Alma Mater Studiorum · University of Bologna

School of Science
Master degree in Physics

Development of qualification procedures for DRM2 acquisition boards of the ALICE-TOF detector

Supervisor:
Prof. Pietro Antonioli

Co-supervisor:
Dr. Davide Falchieri

Presented by:
Marco Giacalone

Session II
Academic Year 2017/2018

To my family

Abstract

Il lavoro di questa tesi è inserito nel contesto del programma di upgrade previsto per l'esperimento ALICE durante lo spegnimento della macchina acceleratrice nel biennio 2019-2020 (Long Shutdown 2).
A partire dal 2021 è prevista in ALICE la registrazione di dati a un rate di interazione maggiore rispetto al passato sia in collisioni pp (fino a 200 kHz) che in eventi Pb-Pb (fino a 50 kHz). Oltre al rinnovo di alcuni detector (tracciatore al silicio e TPC), andranno potenziati gli attuali sistemi di readout per permettere un readout continuo senza preselezione (trigger) di eventi.
Nello specifico l'attività svolta per questa tesi è legata al collaudo e allo sviluppo dei nuovi Data Readout Module (DRM2) che andranno a sostituire i precedenti componenti nel rivelatore a tempo di volo (TOF) dell'esperimento.
Per monitorare le funzionalità della scheda è stata sviluppata una GUI (Graphical user interface) che permette la lettura e scrittura di tutti i registri interni della scheda e anche la programmazione del principale ASIC in uso da essa (il chip GBTx che implementa un ricevitore/trasmettitore a 4.8 Gbit/s). Tale procedura è particolarmente importante in quanto permette al GBTx di programmarsi all'accensione della scheda nella configurazione richiesta.
Poiché la scheda sarà esposta in ambiente radiativo moderatamente ostile (TID = 0.13 krad in 10 anni), sono stati effettuati dei test presso il Centro di Prototerapia di Trento con un fascio di protoni di 100 MeV di energia ad alta intensità su alcuni componenti chiave (FPGA Microsemi Igloo2 e transceiver ottici della AVAGO). Vengono discussi i risultati in termini di resistenza alla dose totale assorbita, di sezione d'urto per Single Event Upset (SEU) e Latchup (SEL).
Al fine di sviluppare un sistema di test-bench compatto della scheda è stata infine sviluppata un'applicazione per consentire il collegamento via LAN attraverso protocollo UDP per monitorare i dati ricevuti attraverso il link GBTx dalla DRM2 con una scheda di sviluppo della Xilinx.

Abstract

The work done with this thesis is linked to the upgrade of the ALICE experiment that will be performed during the shutdown of the LHC in 2019-2020 (Long Shutdown 2).
From 2021 it is foreseen in ALICE the data acquisition with an interaction rate up to 200 kHz for pp collisions and to 50 kHz for Pb-Pb ones. The readout systems will be upgraded, as well as some detectors (like the silicon tracker and the TPC), in order to allow a continuous readout without triggering the events.
The development and the tests of the new Data Readout Module (DRM2), that will replace the older board in the TOF detector of the experiment, are the main topics of this master thesis.
A GUI (Graphical user interface) was developed to better monitor all the functions and read/edit all the board registers. Moreover the software allows one to automatically setup the main ASIC used by the board (the GBTx, implementing a 4.8 Gbit/s receiver/transmitter). This procedure is particularly important because allows to automatically program the GBTx at power-on with the required configuration.
Since the DRM2 will be exposed in a moderately hostile radioactive environment (TID = 0.13 krad in 10 years), a series of tests were done at the Proton Therapy Center in Trento with a proton beam energy of 100 MeV with high intensity on some of the key components of the board (FPGA Microsemi Igloo2 and AVAGO optical transceiver). Results of these tests will be discussed in terms of total dose absorption resistance, cross section per Single Event Upset (SEU) and Latchup (SEL).
Finally, in order to develop a compact test-bench of the board, another software was created that made the connection to PC possible via LAN for monitoring the data received over the GBTx link from the DRM2 through the UDP protocol via a Xilinx evaluation board.

Contents

Introduction

The aim of this thesis is to present my work performed on the DRM2 ALICE-TOF board that will be installed during the LHC Long Shutdown 2 (LS2).
Two software were developed in order to monitor, program and acquire data from the DRM2 card. The software suite developed was used to debug the card and it was provided to the industrial manufacturer currently producing and testing the cards.
This thesis also reports the results of radiation tolerance tests done at the Proton Therapy Center in Trento on some components that will be mounted on the DRM2 card.
A general introduction of the physics involved in the experiment (Quark Gluon Plasma and nuclear strong interaction) is offered in the first chapter, leading to a better understanding of the main reasons behind the detector upgrade.
The ALICE experiment and the upgrade of the ALICE-TOF detector are described in detail in chapter two.
The test setup used both for the radiation tolerance tests and for the development of the GUI software (Direct Control manager and UDPConnect) are shown and described in chapter three.
The development of the software is the main topic of chapter four, presenting its characteristics and the reasons behind each feature.
Finally the methodologies used and the obtained results of the radiation tests are discussed in the last chapter of this dissertation.

Chapter 1

Relativistic heavy-ion collisions physics

ALICE (A Large Ion Collider Experiment) is one of the main LHC experiments at CERN (Geneva), and it is devoted to the study of heavy-ion collisions.
This is because the primary aim of the experiment is to study the Quark Gluon Plasma, which is the state of matter where quarks and gluons are unbound and free to move. This state of matter is reached at very high energy densities, condition satisfied with ultrarelativistic heavy nuclei collisions.
In order to talk about QGP, a brief introduction of nuclear strong interaction is needed.

1.1 Quantum Chromodynamics

The Quantum Chromodynamics (QCD) is the field theory of the strong interaction, which in group theory is described by $SU(3)_C$[1], that is the special Unitary group in 3 dimensions.
QCD is a quantum field theory (QFT) describing interaction among quarks and gluons, where QFT is the theoretical framework for constructing quantum mechanical models of subatomic particles in particle physics [1].
The first step that led to the formulation of QCD was the introduction of the colour charge (in 1964 [2]), which was needed in order to remedy a spin-statistical problem in constructing the Δ^{++} wavefunction (a baryon discovered in 1951) [3]. The particle appeared to be a fermion with symmetric flavour and spin metric function

$$\left|\Delta^{++}\right\rangle = |u_\uparrow u_\uparrow u_\uparrow\rangle \tag{1.1}$$

clearly in contrast with its antisymmetric fermion nature [4].
Eventually, the simplest solution to this problem was to suppose that quarks carry a further degree of freedom, which is *colour*, as a new quantum number associated with the group SU(3), on which the QCD is based, so that the wave function of the particle can be made antisymmetric

$$\left|\Delta^{++}\right\rangle = \left|e^{ijk}\, u_{i\uparrow} u_{j\uparrow} u_{k\uparrow}\right\rangle . \tag{1.2}$$

[1] The c stands for colour charge.

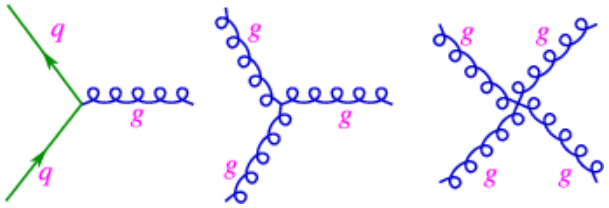

Figure 1.1: Examples of basic QCD Feynman diagrams, where g are gluons and q are quarks.

Quantum Chromodynamics is a non-abelian gauge theory whose Lagrangian density is:

$$\mathcal{L} = \bar{\psi}_q^i (i\gamma^\mu)(D_\mu)_{ij}\psi_q^j - m_q \bar{\psi}_q^i \psi_{qi} - \frac{1}{4} F_{\mu\nu}^a F^{a\mu\nu}, \tag{1.3}$$

where ψ_q^i is a quark field with fundamental colour index i (red, green, blue), $\psi_q = (\psi_{qR}, \psi_{qG}, \psi_{qB})^T$, γ^μ is a Dirac matrix, with μ being a Lorentz vector index, m_q allows for the possibility of non-zero quark masses, $F_{\mu\nu}^a$ is the gluon field strength tensor for a gluon with colour index a (from 1 to 8), and D_μ is the covariant derivative in QCD.

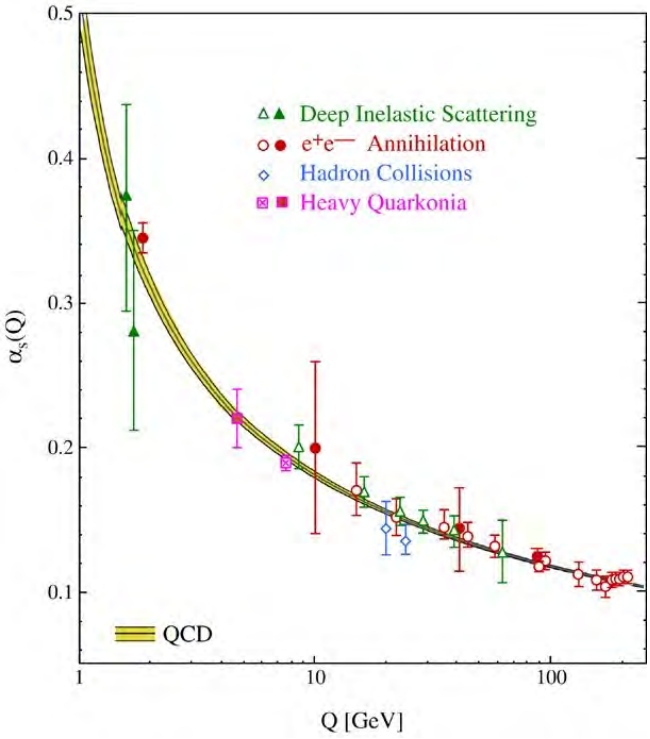

Figure 1.2: Running coupling constant α_s vs the exchanged momentum Q [5].

As for the QED, the interactions between quarks and gluons can be described using Feynman diagrams with the strong coupling constant α_s, which is dependent on the

quadri-momentum transferred (Q^2) at which the interaction takes place and is approximately equal to:

$$\alpha_s(Q^2) = \frac{12\pi}{(22 - 2n_f) \cdot ln(Q^2/\Lambda^2_{QCD})} \tag{1.4}$$

with a first order perturbative QCD calculation (valid at very large energy)[5], where n_f is equal to 6 minus the number of quark flavours and Λ_{QCD} represents an intrinsic energy scale for the strong interaction ($\approx$ 200 MeV).
Self-interaction terms for the gluon, which carries the colour charge, are expected by the theory (as can be seen in Fig. 1.1), making the QCD non-abelian. Furthermore these terms have also a key task on the different screening effect of the charge (Fig. 1.3).
It is common to quote the value of the strong coupling constant at the energy scale of the mass of the Z boson ($\approx$91 GeV), which is $\alpha_s(M_Z) = 0.1177\,^{+0.0034}_{-0.0036}$ (Fig. 1.2) [6].
Many peculiar aspects of the QCD, such as quarks confinement, occur at low energies, similar to Λ_{QCD}, so they can not be treated perturbatively. On the other hand, thanks to the asymptotic freedom (discovered in 1973 by D. Gross, F. Wilczek and D. Politzer[2]), a perturbative approach can be applied at high energy.

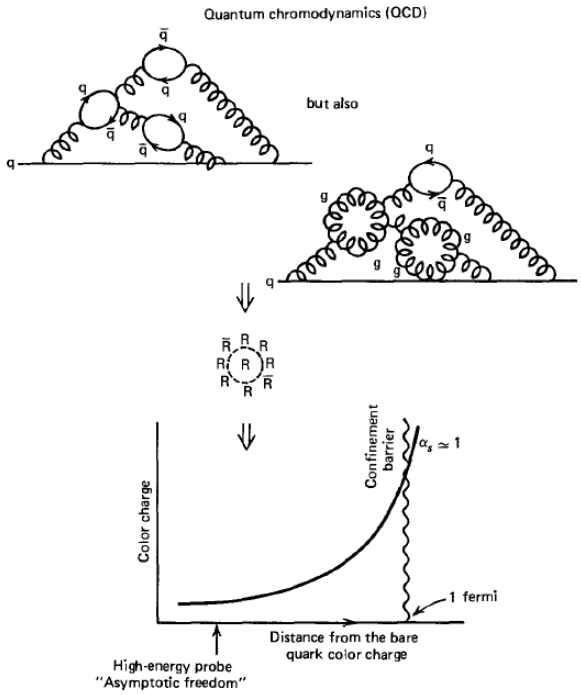

Figure 1.3: Screening of the colour charges in QFT.

In QCD quarks are confined to be bound together forming hadrons. *Colour confinement* means that coloured free particles do not exist in nature as depicted from the fact that no evidence of free quarks at normal conditions has been discovered up to now.

[2]Nobel prize in 2004 [7].

In fact, as can be seen in Fig. 1.3, strong interaction between two quarks rises with the increase of their distance. Moreover, in QCD it looks like a charge is preferably surrounded by other charges with the same colour and the more one approaches the charge the less the charges seem to interact [3].

1.2 Quark Gluon Plasma

At extreme conditions of temperature (175 MeV $\approx 2 \times 10^{12}$ °C) and pressure it is foreseen by theoretical calculations that a new state of matter can be formed: the Quark Gluon Plasma (QGP).
In these conditions quarks and gluons are no more bound to each other in hadrons (radius $\approx$ 1 fm), they are free to move and no more color-neutral [8].
At the boundary between hadronic matter and QGP a phase transition is expected at a critical temperature T_c (Fig. 1.4) which is $\approx$ 170 MeV at near 0 net baryon density, i.e. the density of baryons minus the density of antibaryons (these conditions correspond to the Universe few μs after the Big Bang). When the QGP is formed, quarks and gluons reach a deconfined state.

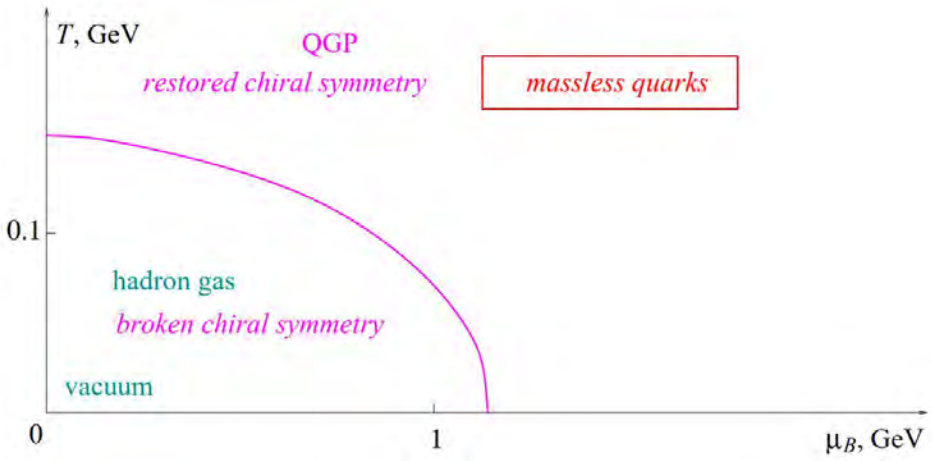

Figure 1.4: Phase Diagram of QCD [9].

The net baryon density in Fig. 1.4 can be derived using the baryochemical potential μ_B, which is the energy (E) a particle needs to increase its quantum baryon number by one:

$$\mu_B = \frac{\partial E}{\partial N_B}, \tag{1.5}$$

where N_B is the number of baryons, but it can be calculated also as the ratio between the baryons and antibaryons abundances. Furthermore, it is shown that an increase of the net baryon density (which is related to an increase of μ_B) yields to a lower value of

T_c for the state transition [10].
Before turning to lattice QCD calculations, the transition between hadronic matter to QGP can be explained using a simple model, called bag model and developed at MIT in the 70's [11].
The simplest form of confined hadronic matter is an ideal gas of massless pions with a pressure of:

$$P_\pi = 3\frac{\pi^2}{90}T^4 \simeq \frac{1}{3}T^4, \tag{1.6}$$

derived from the Stefan-Boltzmann law, where the initial factor 3 is determined by the number of pion charge states. On the other hand, the pressure form for an ideal quark–gluon plasma with two flavours and three colours is

$$P_{QGP} = 37\frac{\pi^2}{90}T^4 - B, \tag{1.7}$$

where 37 is calculated by taking into account also the eight colour degrees of freedom of the gluons and two spin and two particle–antiparticle degrees of freedom of the quarks with a factor 7/8 to obtain the correct statistics. The *bag pressure* B considers the difference between the physical vacuum and the ground state for quarks and gluons in a medium.
Since nature always chooses the lowest state of free energy, which means higher pressure, this implies a phase transition from the pion gas at low T to a QGP at high T, as shown in Fig. 1.5a.

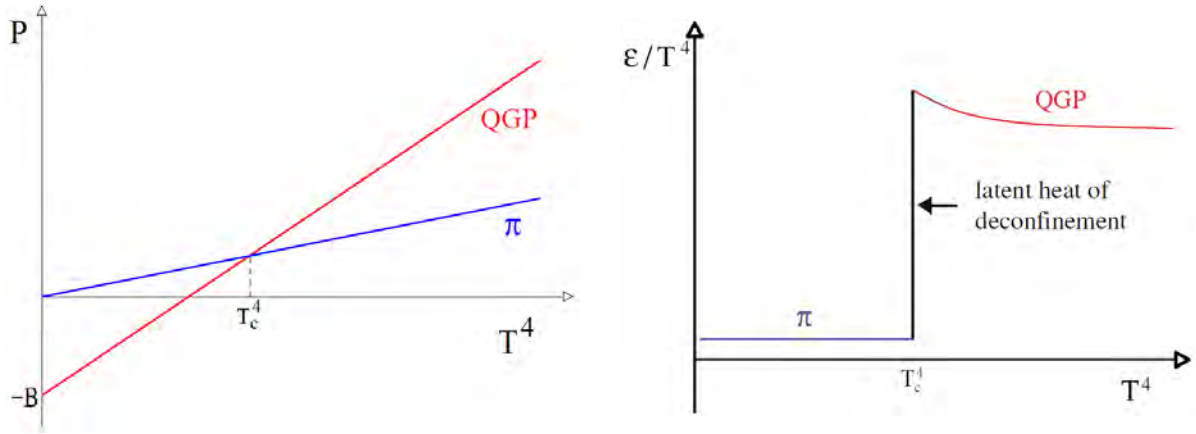

(a) (b)

Figure 1.5: Pressure (a) and energy density (b) of an ideal gas model with two phases, derived from [10].

The critical temperature can be obtained by equalizing P_π and P_{QGP}, that yields to $T^4 = 0.3B$ and therefore, using $B^{0.25} = 200$ MeV, to $T_c = 150$ MeV. Moreover the corresponding energy densities in the model, shown in Fig. 1.5b, become $\varepsilon_\pi \simeq T^4$ and $\varepsilon_{QGP} \simeq 12T^4 + B$, considering that, for an ideal gas of massless constituents, pression

and energy density are connected by the formula $\varepsilon = 3P$ [8]. Thanks to the latent heat of deconfinement, the energy density increases considerably at T_C.
It is possible to show the simple model just analysed derives from strong interaction thermodynamics based on QCD as dynamical input. In order to investigate the phase transition, a perturbative approach can not be used[3], so, as for confinement, QCD lattice calculations [12] are needed and the dependence of the energy density from the temperature can be evaluated numerically by computer simulations.

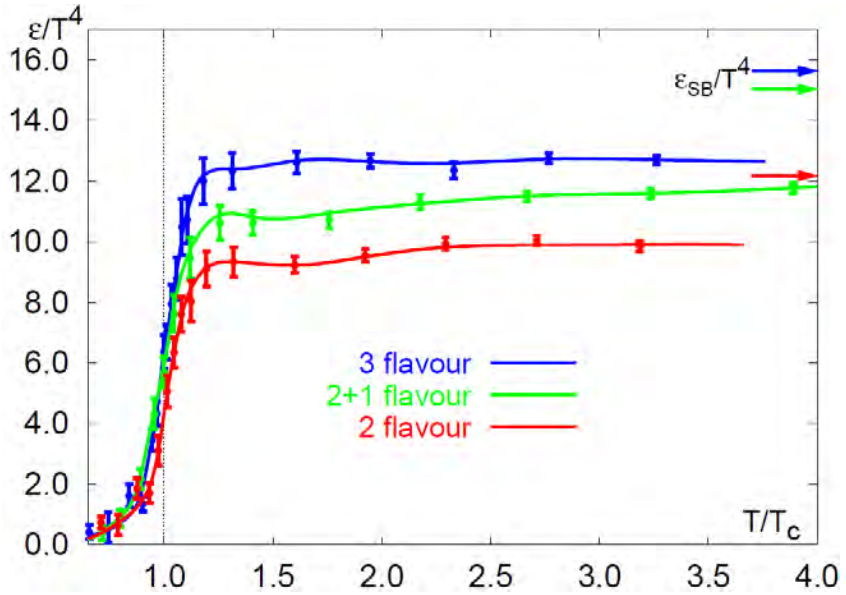

Figure 1.6: Energy density in T^4 units as a function of temperature. The three curves refer to three hypotheses of quark flavours and ε_{SB}/T^4 are the densities obtained using the Stefan-Boltzmann law.

The steep rise of energy density, corresponding to the expected phase transition, is evident in Fig. 1.6, which shows the temperature behaviour of the energy density depending on the quark flavours cases. The increase corresponds to the latent heat of deconfinement and occurs at a T_C of 160-180 MeV, with the energy density at that point equal to $\sim$ 0.5-1.0 GeV/fm^3.
A series of finite-temperature lattice QCD variables, considering firstly the average value of the Polyakov loop [13], i.e. an approximate order parameter for quark deconfinement in a hot gluonic medium, have been studied with a baryon density number close to 0 and it has been discovered that T_L and T_χ, which are the temperature values of deconfinement and of the chiral symmetry breaking respectively (Fig. 1.4), coincides within their errors, so the two phenomenons coincide. Hence the critical temperature for the transition from hadronic matter to QGP is estimated to be $T_C \simeq 175$ MeV.
The first lattice studies made clear the deconfined medium is far from being an ideal

[3]Since, for the study of critical behaviour, long-range correlations and multi-particle interactions are of crucial importance.

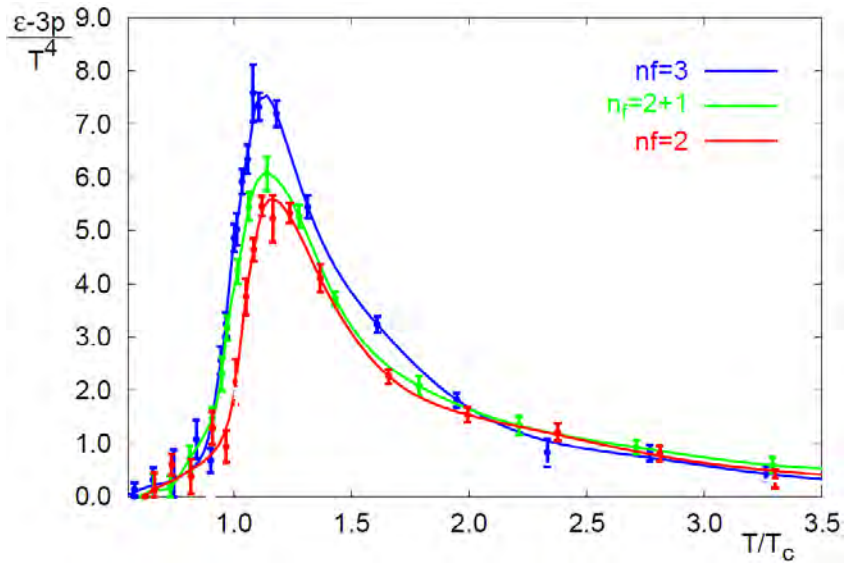

Figure 1.7: Interaction measure in QCD with three hypotheses of quark flavours.

plasma, given that the former is very strongly interacting. This can be seen better from the interaction measure Δ:

$$\Delta = \frac{\varepsilon - 3P}{T^4}, \tag{1.8}$$

which vanishes for non-interacting ideally massless costituents.
The behaviour of the interaction measure, depending on the temperature and the pressure P, is shown in Fig. 1.7, where the peak can be linked to the phase transition seen in energy density shown in Fig. 1.6.

1.3 A selection of experimental observables

Heavy-ion collisions have been studied for more than 20 years now, starting from the first experiments in 1990s with the AGS (Alternating Gradient Synchrotron) at Brookhaven National Laboratories (BNL), which used Au or Pb collisions at a $\sqrt{s_{NN}} = 4.6$ GeV, and with the fixed target experiments at CERN SPS with Lead or Indium at $\sqrt{s_{NN}} = 17.2$ GeV.
Afterwards, this kind of physics has been studied by the Relativistic Heavy-Ion Collider (RHIC) at BNL, which started in year 2000, using p-p, d-Au, Cu-Cu, and Au-Au collisions up to $\sqrt{s_{NN}} = 200$ GeV for four dedicated experiments (PHENIX, STAR, BRAHMS and PHOBOS), and by the Large Hadron Collider (LHC) at CERN, from 2010, where Pb-Pb ions can be accelerated up to $\sqrt{s_{NN}} = 5.5$ TeV, other than p-p, and they are studied mainly by the ALICE, ATLAS and CMS experiments, with the first one specifically dedicated and optimised for lead collisions.
In ultrarelativistic heavy-ion collisions, such as those analysed in LHC, hadronic matter

is heated up to a temperature of at least $2 \cdot 10^{12}$ K[4], creating a *fireball* in which quarks and gluons are melted (QGP). Afterwards the evolution from the hot dense strongly interacting state of matter to hadrons fragments can be studied (Fig. 1.8).
The QGP expands under its own pressure and cools down until it reaches the critical crossing temperature where it hadronizes. The hadron gas keeps expanding for a while until particles do not interact anymore, so the system is *frozen out*.
Basically, the process of *freeze-out* occurs in an expanding system of interacting particles when the mean scattering time (which is inversely proportional to the cross section σ and to the mean velocity of particles) exceeds the mean collision time (inversely proportional to hydrodynamical velocity field) and can be divided in two stages: chemical and kinetic.

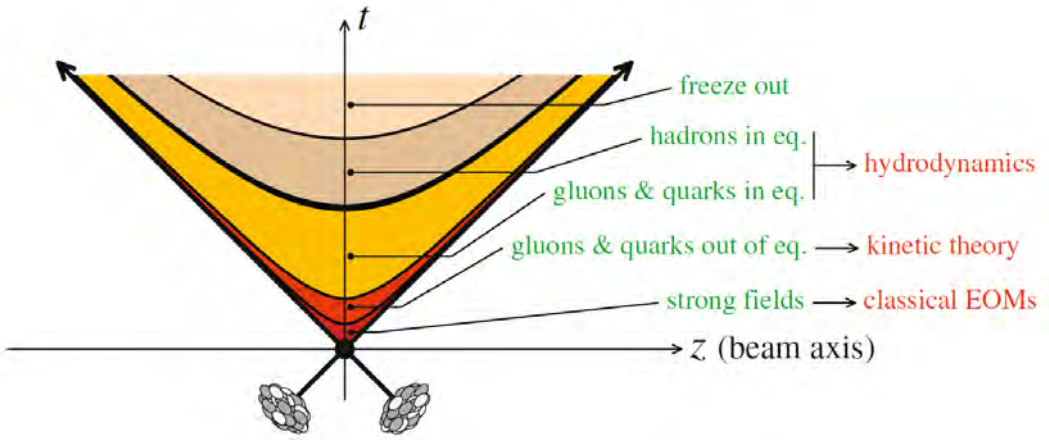

Figure 1.8: Scheme of the various stages of heavy-ion collisions [10].

During the former, which precedes the latter and happens if the inelastic σ outweighs the elastic one, an inverse phase transition takes place (from QGP to hadronic matter) caused by the hadronization of quarks and gluons which will fix particles abundancies and will yield to the final hadronic spectrum. On the other hand, during the latter stage, which happens after the inelastic processes of matter creation stop (elastic cross section prevails), meaning that mutual distances among the new hadrons exceed the typical distance range of the strong interaction ($\sim$ 1 fm), momentum spectra of particles can change due to elastic collisions or resonance decays [14].
Investigating the formation of the QGP is a hard task, given that the lifetime of the deconfinement phase is very short (few fm/c), so several signals leading to understand better the evolution of the collisions are used.
Depending on the moment of the collision phase during which they formed, these signals can be grouped in two categories:

- hard probes: signals produced before the formation of QGP, in the early stages of the collision, due to high momentum parton interaction. They include the study

[4] 1 MeV $\simeq 1.16 \cdot 10^{10}$ K

of heavy quarks, *jet quenching*, direct photons and di-leptons.

- soft probes: signals produced in the later stages of the collision. They carry indirect information about the phase transition and the QGP itself and they can be analysed through spectra studies, strangeness enhancement, correlations in angular distributions and other observables.

In this section several variables are used, hereafter defined: $\sqrt{s_{NN}}$ is the total center-of-mass energy of the colliding particles, p_T is the transverse momentum, equal to $\sqrt{p_x^2 + p_y^2}$, provided that z is the direction of the colliding beams, y is the rapidity, calculated as:

$$y = \frac{1}{2} \ln \left(\frac{E + p_L}{E - p_L} \right) = \tanh^{-1} \left(\frac{p_L}{E} \right),$$

where p_L is the longitudinal momentum and

$$\eta = -\ln \tan \left(\frac{\theta}{2} \right)$$

is the pseudorapidity, the ultra-relativistic approximation of rapidity (more easily experimentally measured), where $E \approx p$ and θ is the angle between the particle momentum and the z axis [15].

1.3.1 Soft probes

Identified particle spectra

One of the characteristics of the expansion of the hadrons emitted after heavy-ion collisions is a strong collective flow, which builds up in the initial partonic phase and through the interaction of hadrons themselves potentially changing the relative abundances.
The collective flow shows that there is a strong correlation between position and momentum variables and, for this reason, it can be studied through the use of some hydrodynamic models, where momentum spectra and motion patterns are calculated using the properties of a fluid, like the viscosity and the equation of state, and the final and initial state boundary conditions, as the freeze-out ones.
The measure of the transverse momentum spectra can offer an insight into the radial flow, which is the component determining the radial expansion of the fireball [16].
Measurements of $\pi/K/p$ spectra at mid-rapidity ($|y|<0.5$) have been performed by the ALICE experiment with Pb-Pb collisions at $\sqrt{s_{NN}} = 2.76$ TeV and results for the most central collisions (0-5%), compared to RHIC ones with Au-Au collisions at $\sqrt{s_{NN}} = 200$ GeV, are shown in Fig. 1.9.
The spectra analysed show a flattening at low p_T for more central collisions, which is coherent with the hypothesis of a strong collective flow.

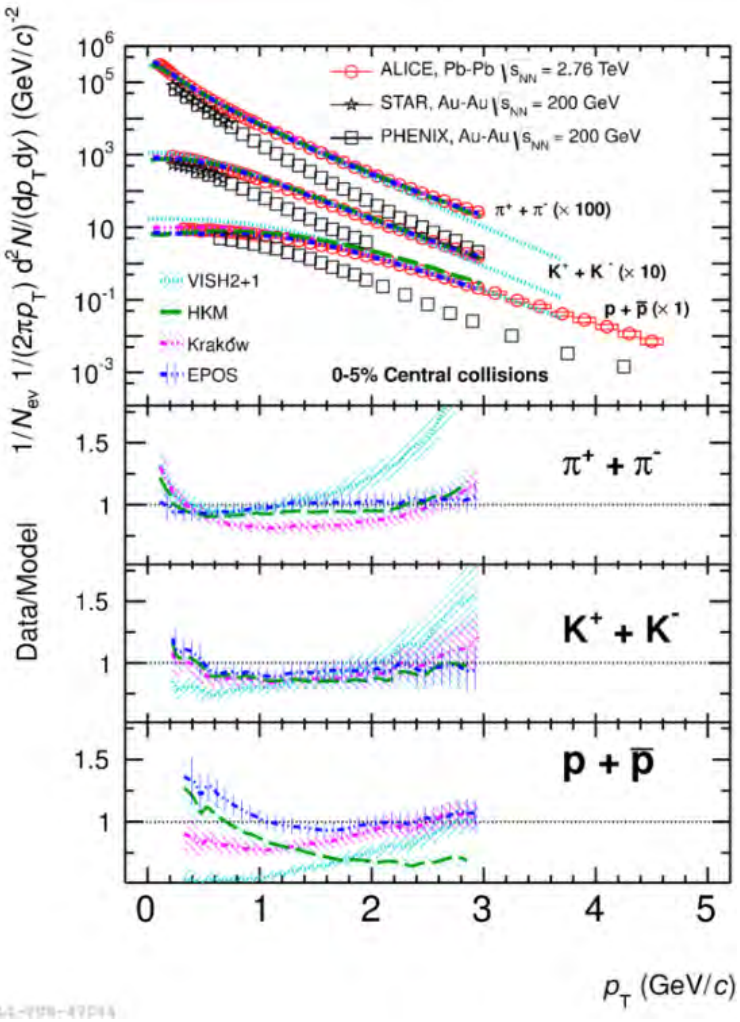

Figure 1.9: p_t spectra of pions, kaons and protons in the centrality range 0-5% measured by ALICE at center-of-mass energy of 2.76 TeV, compared to RHIC results and to hydrodynamical model estimates [16].

Hadron multiplicities

When an energy range opens up for study in heavy-ion collision physics, one of the first measurements performed are those connected with the global characteristics of the event. Among these the charged hadron multiplicities are largely inspected, since they are sensitive to contributions from both hard scatterings ($\propto$ number of collisions) and soft processes ($\propto$ number of participant nucleons N_{part}).
LHC measurements are compared to RHIC results in Fig. 1.10, where charged hadron multiplicity density is analysed as a function of $\sqrt{s_{NN}}$ (Fig. 1.10a) and N_{part} (Fig. 1.10b). The former shows a sharp increase in $\left(\mathrm{d}N_{ch}/\mathrm{d}\eta\right)|_{\eta=0}/\left(\langle N_{part}\rangle/2\right)$ at LHC energies, which is possibly related to the increase of the hard processes contribution, besides in the latter the multiplicity per colliding pair can be seen to have a smooth rise dependant on the

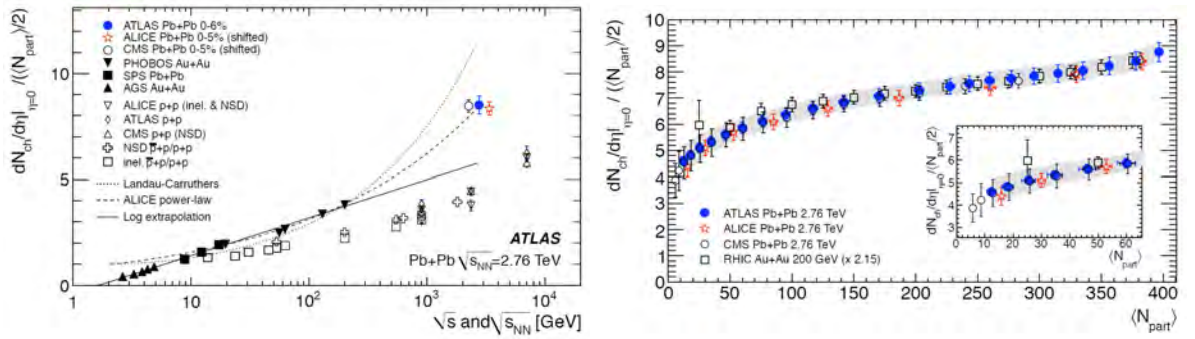

(a) (b)

Figure 1.10: (a) Charged particle multiplicity per participant pair as a function of energy from a variety of measurements in pp, $p\overline{p}$ and central nuclei collisions. The curves show also different expectations for the latter collision case. (b) Charged particle multiplicity per participant pair as a function of N_{part} for centrality intervals of 2% over 0-20% and 5% over 20-80%. The error bars are statistical and systematic uncertainties on $dN_{ch}/d\eta$ combined, while the shaded band represents the total systematic error including also the $\langle N_{part} \rangle$ component [17].

centrality both in RHIC and in LHC experiments.

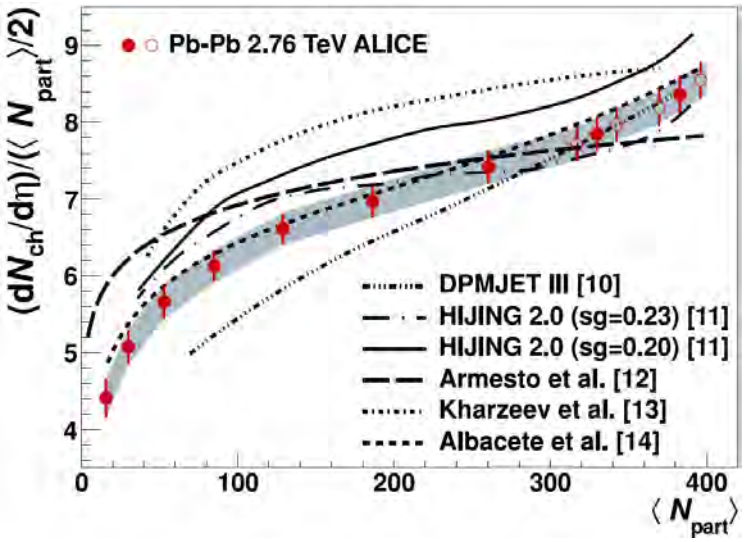

Figure 1.11: Comparison of ALICE 2.76 TeV Pb-Pb data, on $\left(dN_{ch}/d\eta\right)/\left(\langle N_{part} \rangle/2\right)$ as a function of $\langle N_{part} \rangle$, with different models. Statistical errors are negligible, uncorrelated ones are shown via error bars and correlated ones are indicated thanks to the grey band [17].

The obtained data are also coherent to models calculations [17], which were able to

qualitatively predict the multiplicity behaviour[5], as shown in Fig. 1.11.

Strangeness Enhancement

The measurement of strange and multi-strange particle production in relativistic heavy-ion collisions is a unique tool to investigate the property of the QGP, given that there is no strangeness content in the primary colliding nuclei.
This is one of the soft probes analysed and it was one of the earliest proposed signatures of the formation of a deconfined QGP [18].
In heavy-ion central collisions during the final stage of the phase transition strange quarks are expected to be produced more abundantly as a consequence of the restoration of chiral symmetry and is interpreted as the result of the energy loss suffered by partons while crossing the *fireball*.
The effect was observed in Pb-Pb collisions firstly at the NA57 experiment at 158 GeV/c compared to p-Be collisions [19] and was later confirmed by STAR at RHIC and by ALICE in central 2.76 TeV collisions compared to pp interactions [20].

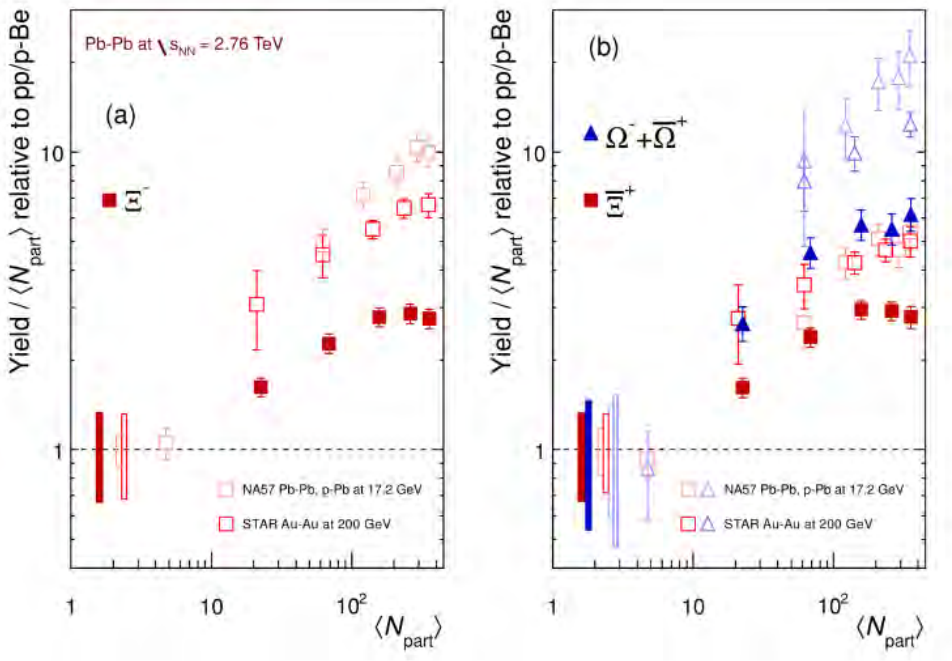

Figure 1.12: Strange enhancement at mid-rapidity ($|y| < 0.5$) as a function of the mean number of participants N_{part} measured by ALICE and compared to RHIC and SPS data. The particles shown have a strangeness of ± 2 for Ξ baryons and of ± 3 for Ω ones [20].

[5]The models were either based on a combination of perturbative QCD processes and soft interactions or saturation ones.

1.3.2 Hard probes

R_{AA} spectra

Particle production in heavy-ion collisions is often characterised by the nuclear modification factor R_{AA} defined as the ratio of the yield in p-A or A-A collisions to the pp yield scaled by the number of binary collisions:

$$R_{AA} = \left(\frac{\partial^2 N_{AA}}{\partial y \partial p_T}\right) \cdot \left(\langle N_{coll}\rangle \frac{\partial^2 N_{pp}}{\partial y \partial p_T}\right)^{-1},$$

where N_{AA} is the particle yield and N_{coll} is the number of collisions in a given centrality class, often computed from the Glauber model [17].

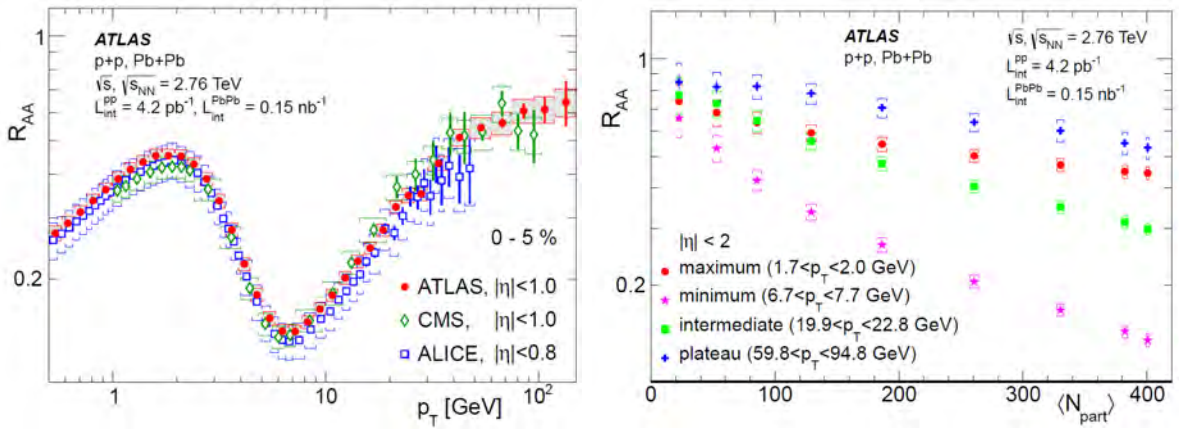

(a) (b)

Figure 1.13: R_{AA} vs (a) p_T and vs (b) the number of participants measured by ATLAS and compared to CMS and ALICE data [21].

LHC measurements have observed the produced particle suppression at large momentum, through the analysis of the nuclear modification factor, and the disappearance of back-to-back correlations, as already found by RHIC, which are consistent with the dense partonic nature hypotheses of the produced medium in nuclei collisions.
Results of the nuclear modification factor for ATLAS, CMS and ALICE are shown and compared in Fig. 1.13: they are in very good agreement for similar centralities and rapidity values [17].
Results are also compared to several models, which consider the charged observed particles as generated by the hadronisation of the medium excited by parton energy loss, and they are shown in Fig. 1.14.

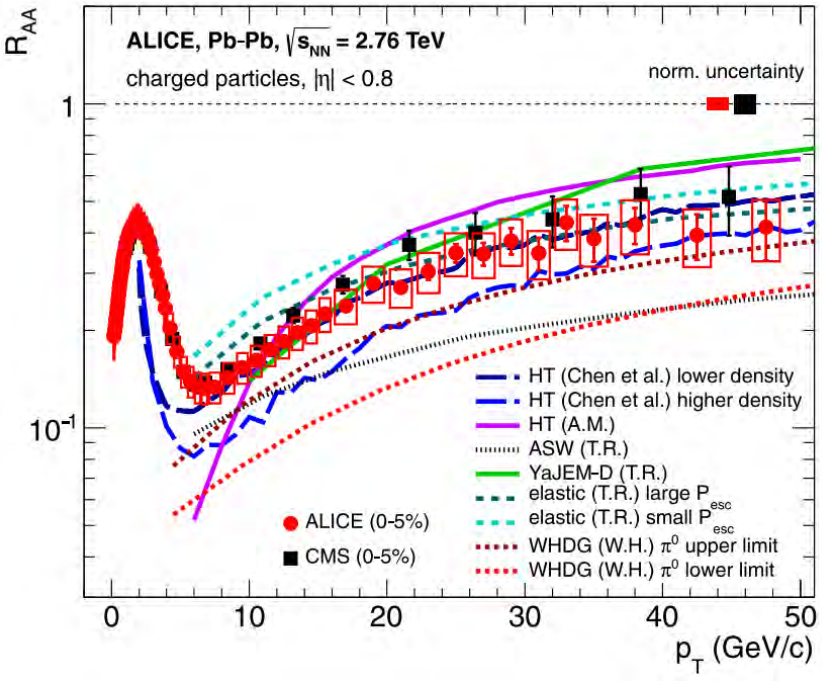

Figure 1.14: Nuclear modification factor as a function of transverse momentum for the ALICE experiment, compared to different models and CMS data [22].

Quarkonia production

The formation of QGP should prevent the binding of $c\bar{c}$ and $b\bar{b}$ (quarkonia), mostly due to colour screening in the deconfined stage, yielding to the suppression of J/ψ (charmonium) and Υ (bottomonium) states. Indeed the suppression of quarkonium production with respect to pp collisions is one of the most distinctive signature of the quark-gluon plasma formation [23].
Another phenomenon that may contribute to the suppression without the need of the QGP formation is the dissociation in cold nuclear matter [24]. These effects (nuclear shadowing, gluon saturation, energy loss and nuclear absorption) are largely unknown at the LHC energy and can be quantified thanks to p-Pb collisions measurements [25].
However other theoretical considerations anticipated that charmonium enhancement at the LHC is also an option, since a large number of $c\bar{c}$ pairs can be formed by quark recombination (given the relatively high abundances of c quark in the formed QGP), so J/ψ production is definitely a more complex mechanism.
Large data samples provided by the LHC of Pb-Pb collisions at $\sqrt{s_{NN}} = 2.76$ TeV (2010-2011), p-Pb collisions at $\sqrt{s_{NN}} = 5.02$ TeV (2013) and at $\sqrt{s_{NN}} = 8.16$ TeV (2017) [26] allowed the study of the production of various quarkonium states and the J/ψ, above all, was studied differentially in p_T and y.
An example of charm suppression is shown in Fig. 1.15, where inclusive J/ψ R_{AA} measured by ALICE at midrapidity is compared to PHENIX data. The suppression

observed in the former is clearly smaller for low p_T than the latter, which is coherent with the presence of a significant regeneration of J/ψ.

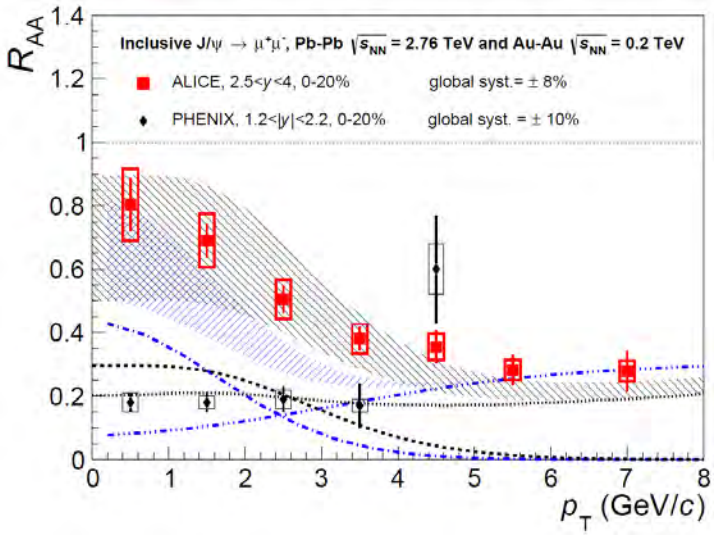

Figure 1.15: Inclusive J/ψ R_{AA} as a function of the transverse momentum measured in Pb-Pb collisions at $\sqrt{s_{NN}} = 2.76$ TeV by ALICE and in Au-Au collisions at $\sqrt{s_{NN}} = 0.2$ TeV by PHENIX. Measurements are also compared to theoretical models [17].

Jet Quenching

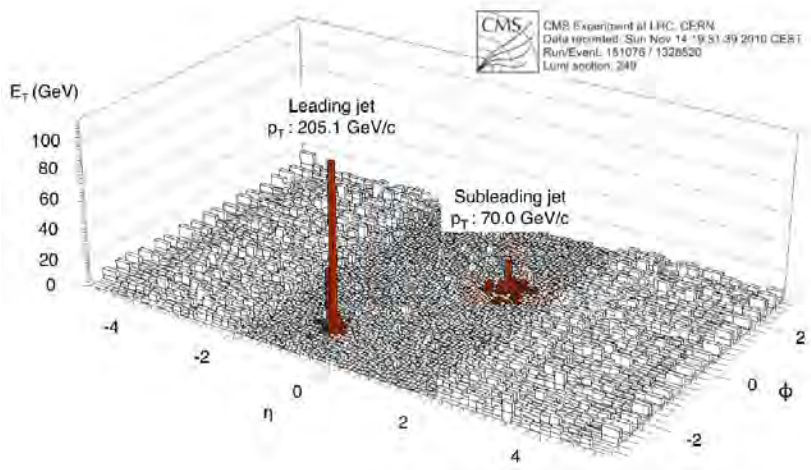

Figure 1.16: Example of an unbalanced dijet in a PbPb collision event at $\sqrt{s_{NN}} = 2.76$ TeV. Data are shown through the summed transverse energy in the electromagnetic and hadron calorimeters of CMS as a function of the pseudorapidity η and of the azimuthal angle ϕ, with the identified jets highlighted in red and labeled with the corrected jet transverse momentum.

Another important hard probe worth of studying is *jet quenching*, which is the energy reduction of jets (a spray of collimated elementary particles created by the collisions of high energy particles) due to their interaction with the QGP, mainly through *gluon-strahlung*.
This results in the decrease of the number of particles produced with high p_T [27].
Experimentally this can be analised through dijets (Fig. 1.16), which are a pair of jets produced back-to-back: it is clear that the one produced near the fireball surface has a yield greater than the one moving through the plasma, because of the energy loss of the latter in the medium before leaving it, so this phenomenon can provide useful information on the QGP itself.

Heavy Flavours

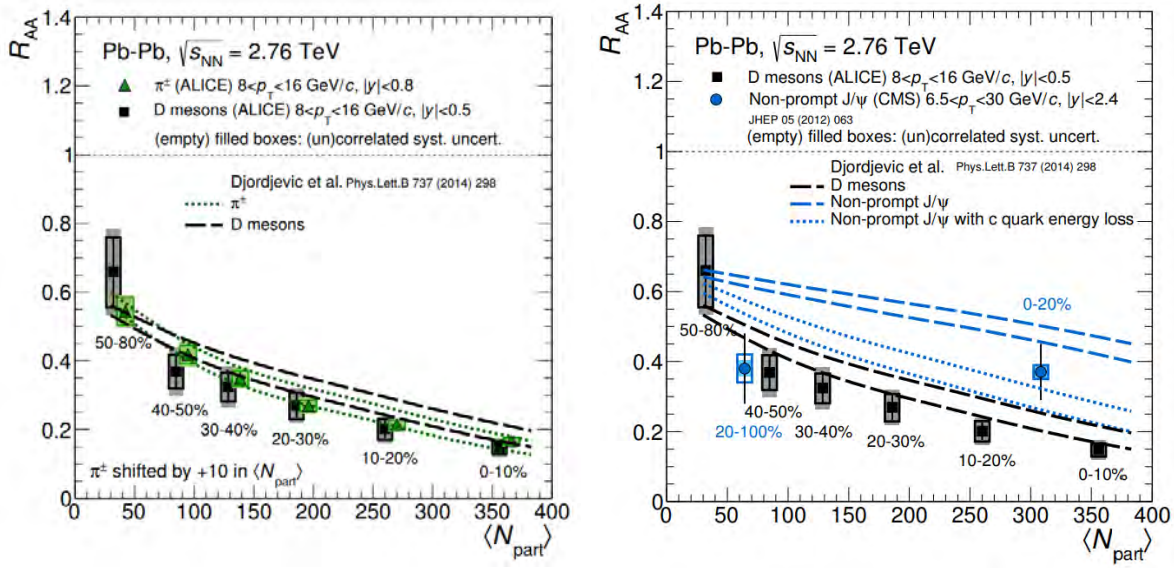

(a) (b)

Figure 1.17: Nuclear modification factor of D meson compared to the R_{AA} of (a) pions and (b) non-prompt J/ψ. In the former measurements are both performed in ALICE at $\sqrt{s_{NN}} = 2.76$ TeV, whereas in the latter the non-prompt J/ψ results derive from CMS measurements [28].

The study of heavy quarks is really important while studying the quark gluon plasma since, due to their masses being larger then the temperature of the system, they cannot be created or destroyed in the medium, but they are rather produced by hard scattering during early stages of high energy heavy-ion collisions and probing the medium during all its evolution depicted in Fig. 1.8. For instance, their study can give an overview on the degree of thermalization of the medium and on its transport coefficient, given that heavy quarks can lose energy and participate in the collective motion of the created

system.
The energy loss of heavy quarks was studied firstly thanks to direct measurements of D meson hadronic decay by STAR and PHENIX experiment at RHIC, which is also able to separate contributions of charm and bottom quarks in the lepton decay channel.
Moreover, at the LHC the measurements of heavy flavours have been extended towards higher transverse momentum values, and provide now detailed information on various charmed mesons and on beauty production via detection of J/ψ from the B decay or hadronic ones for non-prompt decays of J/ψ, i.e. J/ψ deriving from b decays.
Nuclear modification factor for D mesons is analysed in Fig. 1.17 comparing the results of both the ALICE experiment and CMS. D meson production is largely suppressed for central collisions at 0-10% centrality in lead-lead collisions, which agrees with the corresponding results for charged pions (Fig. 1.17a). On the other hand Fig. 1.17b shows that beauty quarks are less suppressed than charm ones, consistently with expectations that predict a mass dependence on the energy loss of the parton due to gluonstrahlung.

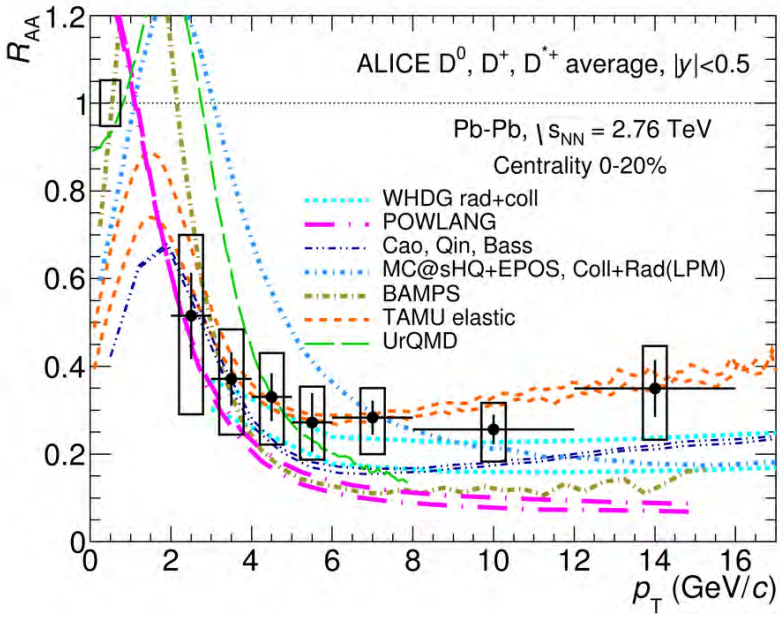

Figure 1.18: Average nuclear modification factor of D meson as a fucntion of p_T measured by ALICE with Pb-Pb collisions at $\sqrt{s_{NN}}$ with a centrality range of 0-20% [29].

More information can be found in Fig. 1.18 where the R_{AA} results for the D meson are compared to various theoretical models [17]. The strong suppression is still visible, but it decreases for smaller transverse momentum values.

Chapter 2

The ALICE detector and its upgrade programme

ALICE is one of the main experiments of the LHC, designed and optimized to detect particles produced in heavy-ion collisions.
The collisions create a multitude of particles that are detected using a variety of different detectors.
The upgrade programme of the experiment will acquire 10 nb^{-1} of integrated luminosity with Pb-Pb collisions, which is 100 times more than the samples acquired both with RUN1 and RUN2, from 2009 to 2018 of LHC beam usage. This is possible thanks to some upgrades on the detector itself including the update of the readout and acquisition system of the time-of-flight detector, which will be described later [30].

2.1 ALICE detectors

As already mentioned the main task of ALICE is to study the QGP. It is a general purpose experiment, designed to cope with the higher multiplicity of produced particles in Pb-Pb collisions compared to p-p collisions [31] and whose detectors measure and identify hadrons at mid-rapidity, which means $|\eta| \lesssim 0.9$.
ALICE is 26 m long, 16 m high and 16 m wide, with a mass of approximately 10^4 tons. It consists of a central barrel part which analyses hadrons, electrons and photons, enclosed in a solenoid magnet (reused from the L3 experiment at LEP) providing a magnetic field of 0.5 T, and of a forward muon spectrometer, which includes a dipole magnet that provides a 0.67 T field. The central part covers polar angles from 45° to 135° and, from inside out, it contains as shown in Fig. 2.2: an Inner Tracking System (ITS) that allows precise tracking and vertex determination; a large cylindrical Time Projection Chamber (TPC), responsible for the global tracking and particle identification through the measurement of the specific energy loss in gas; a Transition Radiation Detector (TRD) and a Time-of-Flight (TOF) system, which identify respectively electrons and charged hadrons; a Ring Imaging Cherenkov detector (the High Momentum Particle

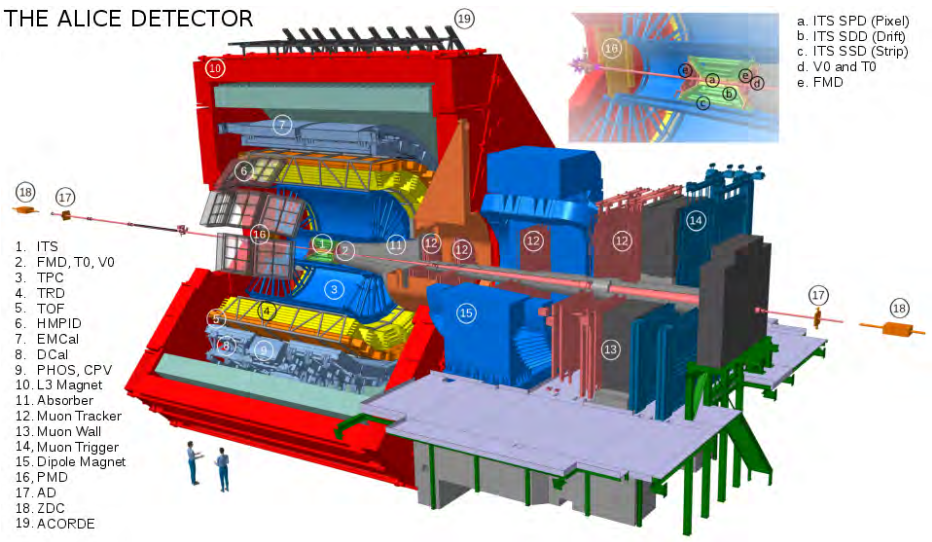

Figure 2.1: The ALICE experiment with an overview of its detectors.

Identification, HMPID); and two electromagnetic calorimeters (PHOS and EMCal). All the detectors mentioned have a full cover of the azimuthal angle, except HMPID and the two calorimeters.

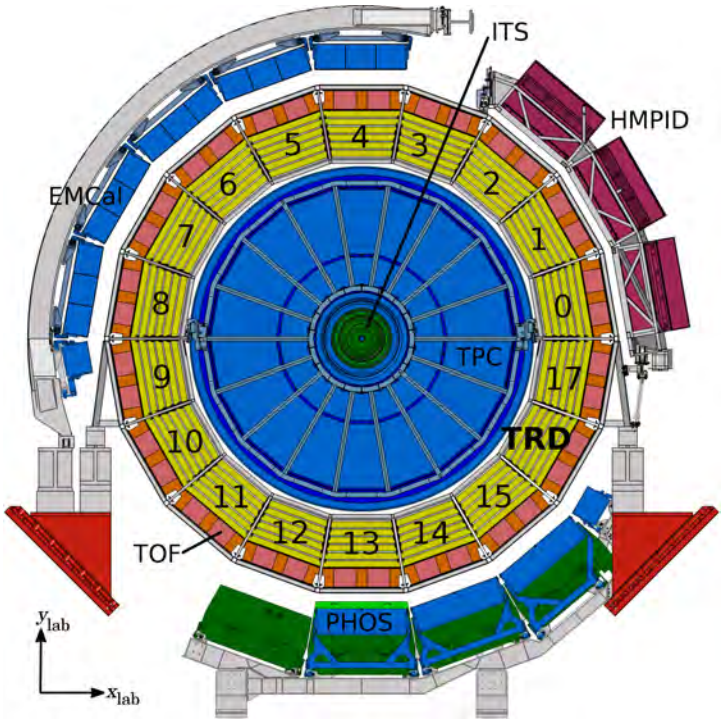

Figure 2.2: Schematic transverse view of the ALICE central barrel detectors as of the start of LHC RUN2 (2015) [32].

Furthermore several smaller detectors (ZDC, PMD, FMD, T0, V0) used for global event characterization and triggering are arranged at small angles near the beam pipe. Finally, on top of the L3 magnet an array of scintillators (ACORDE) provides cosmic rays trigger for calibration, alignment purpose and for cosmic ray physics.

2.1.1 The Inner Tracking System

Being the closest tracking detector to the LHC beam pipe in ALICE, the main task of the ITS is the tracking of the primary vertex of the collision with a resolution better than $100\mu m$. Moreover the detector reconstructs the secondary vertices from the decays of hyperons and heavy flavour hadrons. It is used for the tracking and the identification of particles with a momentum lower than 200 MeV/c, to improve the momentum and angle resolution for particles reconstructed by the TPC and also for the reconstruction of particles traversing dead regions of the TPC itself.

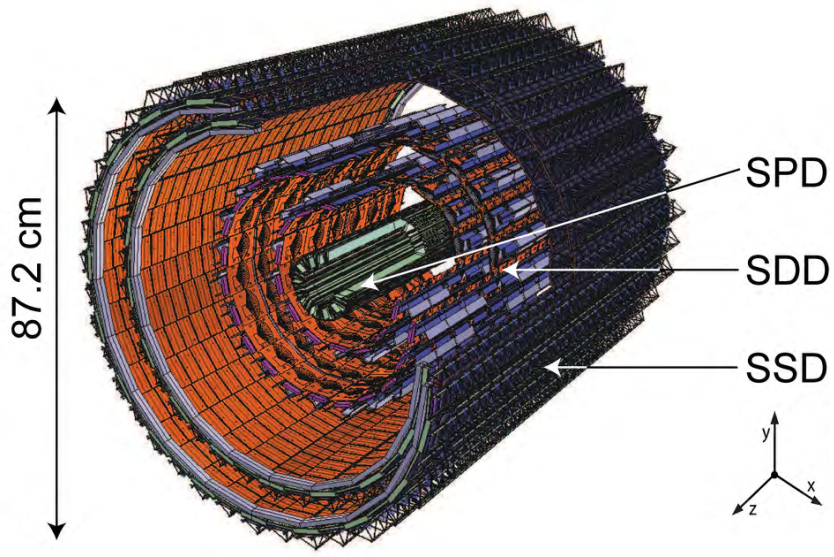

Figure 2.3: Schematic view of ALICE 6 layers Inner Tracking System [33].

The ITS surrounds the beam pipe, which is a 800 μm-thick beryllium cylinder of 6 cm outer diameter, coaxial with the ITS detector layers. It consists of six cylindrical layers of silicon detectors (Fig. 2.3), located at radii between 4 and 43 cm and designed taking into account the high multiplicity environment for central Pb-Pb collisions, that (from innermost to outermost) are: 2 layers of Silicon Pixel Detector (SPD), 2 of Silicon Drift Detector (SDD) and 2 of Silicon Strip Detector (SSD).
The SPD is based on hybrid silicon pixels (sensor ladder) of reverse-biased silicon detector diodes bump-bonded to readout chips. The basic detector module is the half-stave, which consists of two ladders, one Multi-Chip Module (MCM) and one high density aluminium/polyimide multi-layer interconnect. In total the 60 staves of the SPD include

240 ladders with 1200 chips forming a total of $9.8 \cdot 10^6$ readout channels.
The SPD is also used for the trigger system, especially for the selection of minimum bias events.
The SDD is based on modules whose sensitive area are split into two drift regions. Each module consists of one silicon drift detector and two front-end hybrids and is mounted on a linear structure called ladder. The inner layer of SDD is composed by 14 ladders with 6 modules each and the outer has 22 ladders containing 8 modules each.
The SSD is crucial for the matching of tracks from the TPC to the ITS and they also provide specific energy loss information (dE/dx) information to assist particle identification for low momentum particles.
They are made by detection modules composed by one double-sided strip detector connected to two hybrids that host the front-end electronics. Each sensor has 768 strips on each side.
The modules are arranged on 72 ladders, which carry a total of 1698 modules [31].
An example of the ITS PID performance is shown in Fig. 2.4.

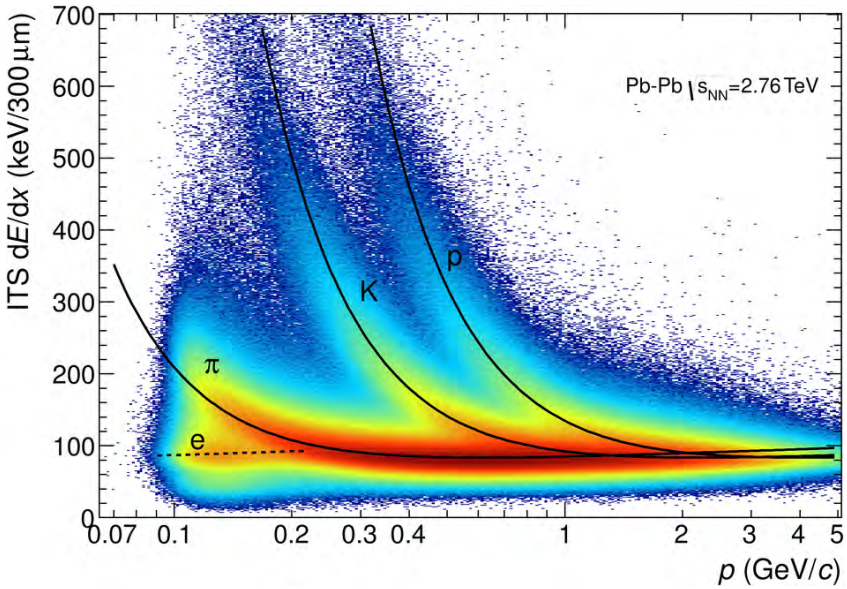

Figure 2.4: Energy loss distribution as a function of the particle momentum, both measured by the ITS alone in Pb-Pb collisions at 2.76 TeV. The black lines are a parametrization of the detector response based on the Bethe-Bloch formula [34].

2.1.2 The Time Projection Chamber

The TPC, a cylindrical detector with an inner radius of ≈85 cm, an outer one of ≈250 cm and an overall length along the beam direction of 5 m (Fig. 2.5), is the main tracking detector of the central barrel, covering the mid-rapidity range ($\eta \lesssim 0.9$ with full radial track length, matching with ITS, TRD and TOF), and providing excellent tracking performance, in spite of the high multiplicity environment.

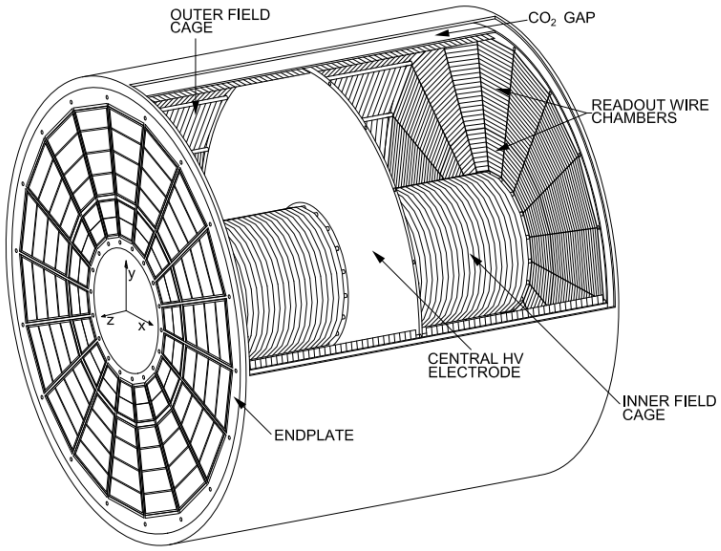

Figure 2.5: 3D view of the TPC field cage, where the high voltage electrode is located at the center of the drift volume [35].

The TPC volume is filled with 90 m^3 of $Ne/CO_2/N_2$ (90/10/5) in which the primary electrons are transported over a distance of up to 2.5 m with a drift velocity of 2.7 cm/s on either side of the central electrode to the end plates, where multi-wire proportional chambers with cathode pad readout are located and arranged into 18 trapezoidal sectors at each end plate. The volume is split in half by a central cathodic plane separating it in two drift regions.

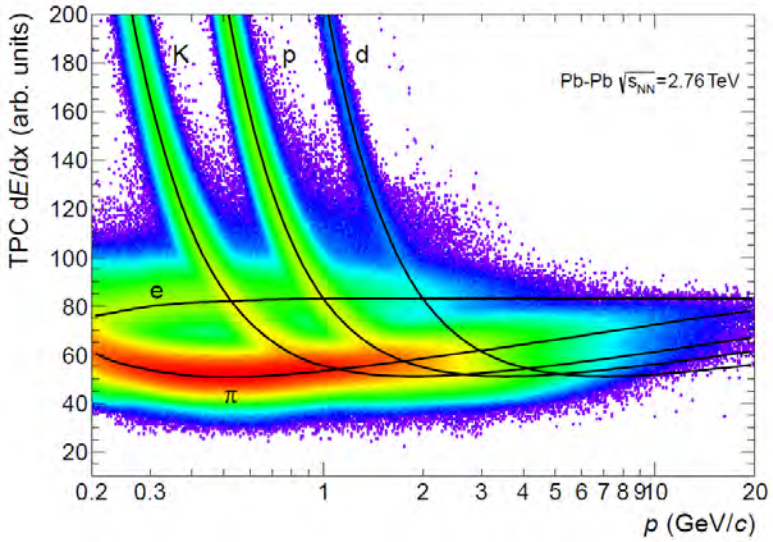

Figure 2.6: Specific energy loss in the TPC as a function of the particle momentum in Pb-Pb collisions at 2.76 TeV. The black lines are the parametrizations of the expected mean energy loss [34].

Given the electron drift velocity and the drift space just mentioned, there is a maximum drift time of $\sim 90\,\mu s$ which currently sets a limit on the event rate sustainability. The detector covers a wide range of transverse momenta p_T from 100 MeV to 100 GeV with good momentum resolution and efficiency (~ 90 %) [31].
The charge collected in the TPC readout pads is used to measure the particle energy loss, that combined with the momentum measurement, acquired thanks to the particle deflection in the magnetic field, allows one to separate charged particles species in the low momentum region, as shown in Fig. 2.6.

2.1.3 The Transition Radiation Detector

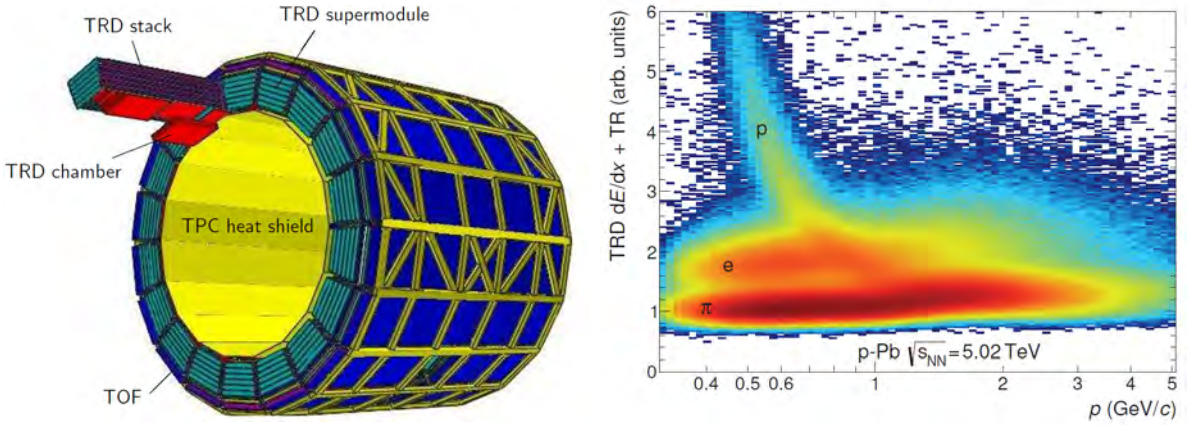

(a) (b)

Figure 2.7: (a) Schematic view of the TRD layout in the ALICE space frame. On the outside the TRD is surrounded by the TOF system (dark blue), while on the inside it surrounds the heat shield (yellow) towards the TPC [31]. (b) Sum of TRD signal, obtained with ionization energy loss and transition radiation, vs momentum of protons from Λ decays, charged pions from K^0_S decays and electrons from γ conversions in p-Pb collisions at 5.02 TeV [34].

The main purpose of the TRD is to provide electron identification in the central barrel for transverse momentum >1 GeV/c, below which the electrons can be identified using the energy loss measurement in the TPC.
A transition radiation (in the keV range) is emitted when a relativistic charged particle crosses the interface of two media with different dielectric constant [36]. Electrons with momentum above the threshold ($\gamma \approx 1000$) radiate differently with respect to pions, so the TRD can extend the capabilities of rejection of the TPC up to very high momenta. The TRD, depicted in Fig. 2.7a, consists of 540 readout detector modules arranged into 18 supermodules, each containing 30 modules. Each detector element consists of a 48 mm thick radiator, a drift section of 30 mm thickness and a multi-wire proportional chamber with pad readout and is filled with a mixture of Xe-CO_2 (85:15).

The longitudinal active length of the detector is 7 m, while the overall length is 7.8 m, with a total mass of 1650 kg.
In conjuction with the data of both TPC and ITS, the TRD provides the necessary electron identification capability. An example of its PID performance is shown in Fig. 2.7b.
Moreover the TRD is used to derive a fast trigger for charged particles of high momentum (it is a part of the Level 1 trigger), to select high momenta electrons coming from heavy flavour decays [31].

2.1.4 The Time Of Flight

This detector is dedicated to the identification of charged particles in the intermediate momentum range, below $\sim$ 2.5 GeV/c for pions and kaons, up to 4 GeV/c for protons and with a separation of π/K and K/p better than 3σ. This is achieved thanks to a overall detector time resolution of around 80 ps [37].

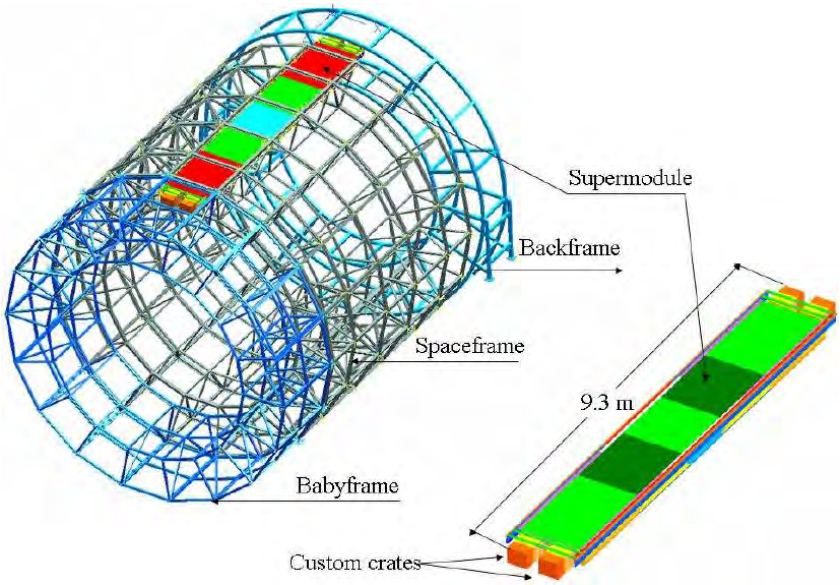

Figure 2.8: Schematic drawing of the TOF detector spaceframe highlighting one of the detector supermodule [31].

The TOF system is a large double-stack Multi-gap Resistive Plate chamber (MRPC) array and has a modular structure with 18 sectors in the azimuthal angle, each one having 5 modules along the beam direction (Fig. 2.8). The design of the detector has been studied to cope with a very high charged-particles density and with ≈150000 independent readout channels.
The whole device is contained in a cylindrical shell with an internal radius of 3.7 m and an external one of 3.99 m. Its thickness corresponds to 30% of a radiation length.
The MRPC strip is 122 cm long and 13 cm wide with an active area of 120×7.4 cm^2

subdivided into two rows of 48 pads each of 3.5×2.5 cm^2. Every module consists of a group of MRPC strips (15 in the central one and 19 in the others) closed inside a gas-tight box, whose gas is a mixture of freon, isobutan and sulfur hexafluoride (90:5:5). The MRPC is basically a stack of resistive plate chambers with high voltage applied to the external surfaces. The fundamental physical process of this kind of detectors is particle ionization, in which a charged particle during its movement ionizes the gas, thus producing an ion-electron pair. The high and uniform electric field over the full sensitive gaseous volume generates a gas avalanche producing the observed signals on the pick-up electrodes segmented into pads and located in PCBs (see Fig. 2.9).

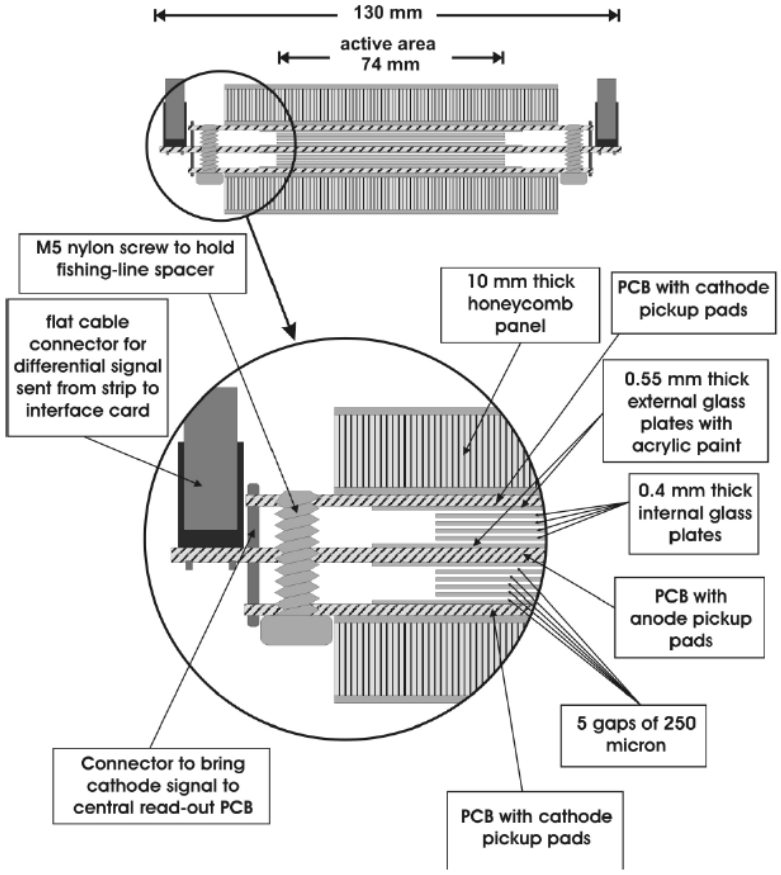

Figure 2.9: Schematic transversal section of a double-stack MRPC [31].

Moreover, two honeycomb panels are attached to the two most external PCBs in order to make the system more rigid.
Figure 2.10 shows the TOF performance expressed as β vs the particle momentum (Fig. 2.10a) and an example of the combined PID capabilities for pions with TOF and TPC (Fig. 2.10b).

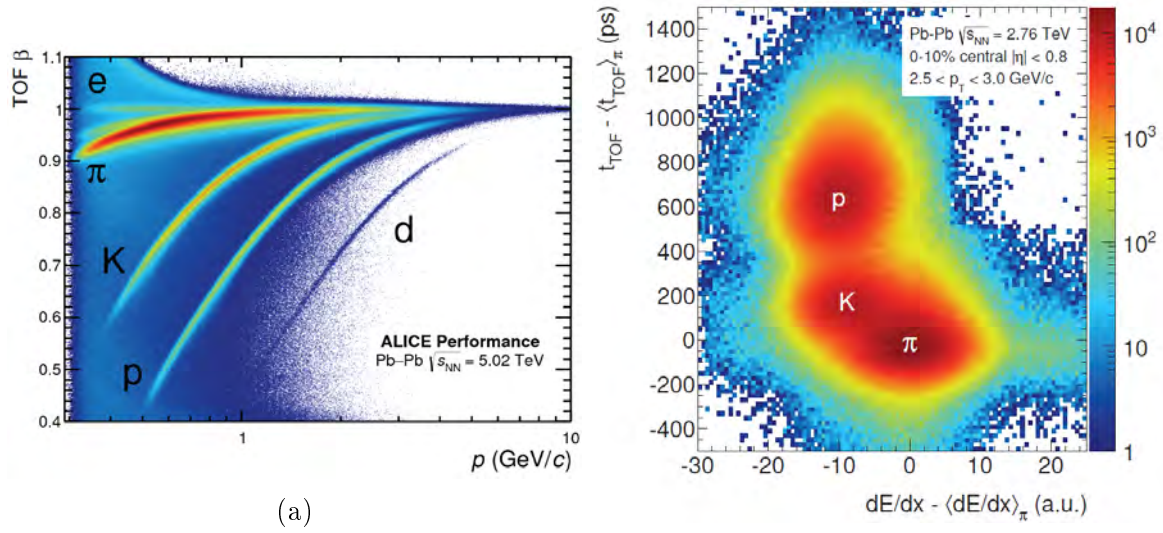

(a) (b)

Figure 2.10: (a) Distribution of β as a function of the particle momentum for Pb-Pb collisions at 5.02 TeV [38]. (b) Combined pion identification in Pb-Pb collisions at 2.76 TeV with the time of flight from the TOF system and with the specific energy loss from the TPC [34].

2.2 The ALICE upgrade programme

The ALICE experiment has a rich detector upgrade programme scheduled during the Long Shutdown 2 (2019-2020)[1], in order to achieve continuous readout and to accumulate an integrated luminosity of 10 nb^{-1} on Pb-Pb collisions between 2021-2029, which is 100 times more than the samples obtained both with RUN1 and RUN2 combined [30].
The measurements with lead ions will be complemented by precision measurements of p-p and p-Pb collisions to have reference data at the equivalent Pb energy. It is estimated that 6 pb^{-1} of integrated luminosity are needed to obtain a significance comparable with the Pb-Pb data. This means a p-p data taking with an event readout of 200 kHz.
The main upgrades that will make this increase possible are:

- the upgrade of the readout system of the TPC, which will replace the MWPC readout with a GEM system (Gas Electron Multiplier) [39].
- a new silicon tracker (ITS) completely made of pixels with a higher spatial resolution on secondary vertexes [40];
- upgrade of the Online Systems, which include High-Level Trigger (HLT), data acquisition (DAQ) and trigger system to cope with higher rates;

[1] After which the LHC will progressively increase its instantaneous luminosity with Pb beams from 10^{27} cm^{-2}s^{-1} to 6 times this value, eventually reaching an interaction rate of 50 kHz.

- the upgrades of the readout systems of various detectors, including TOF (see Sec. 2.2.3) [41];
- the upgrade of the offline data processing software to cope with the reconstruction and analysis of a larger number of events [42].

The ALICE upgrade will improve the general performances of the detector, except for the PID capabilities that will remain the same.

2.2.1 Physics motivation

The main physics topics that the experiment wants to explore, as addressed by the proposed upgrade programme, require the analysis of heavy flavour hadrons, quarkonia and low-mass dileptons which are characterized by rare signals, so large statistics is needed. These signals are also difficult to trigger so the idea of the upgrade is to obtain all the events (continuous readout) and to identify only afterwards (offline via software) the interesting ones.

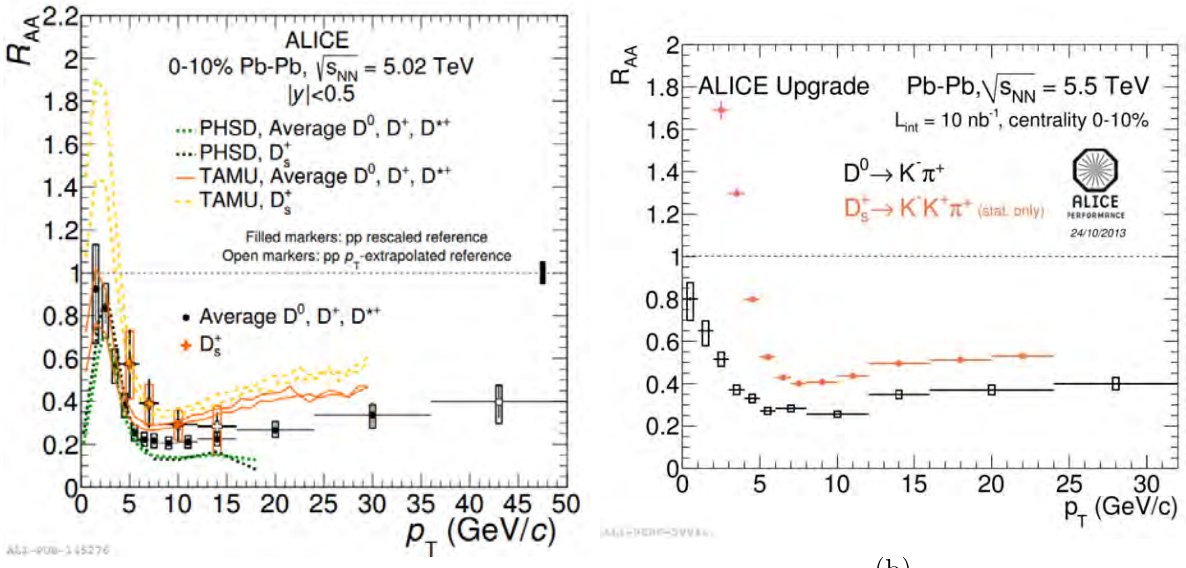

(a) (b)

Figure 2.11: (a) Average nuclear modification factor of D^0, D^+ and D^{*+} and R_{AA} of D_s^+ as a function of transverse momentum for 0-10% central Pb-Pb collisions at $\sqrt{s_{NN}} = 5.02$ TeV from data analysis in ALICE compared with the PHSD and TAMU model calculations. (b) ALICE upgrade R_{AA} of D^0, D^+, D^{*+} and D_s^+ vs p_T at 0-10% centrality range and at $\sqrt{s_{NN}} = 5.5$ TeV obtained using a Monte Carlo simulation [43].

Heavy flavours have a special role in heavy-ion physics because they provide a tagged probe enabling a unique access to their interactions in the QGP, thus allowing us to gain insights into the properties of the medium.

The open questions concerning their interactions are: the thermalization and hadronization of heavy quarks in the medium, studied through the baryon-to-meson ratio for charm and beauty (respectively Λ_c/D and Λ_b/B), and the energy loss of heavy quarks in the QGP and its mass dependence, which can be addressed by measuring the nuclear modification factors of the transverse momentum distribution of D and B mesons in a wide momentum range [30].
For instance in Fig. 2.11 the nuclear modification factor is shown and obtained both with measurements using the current setup (Fig. 2.11a) and with Monte Carlo simulations (Fig. 2.11b) using the upgraded experiment. The latter shows R_{AA} uncertainties significantly lower than the former.

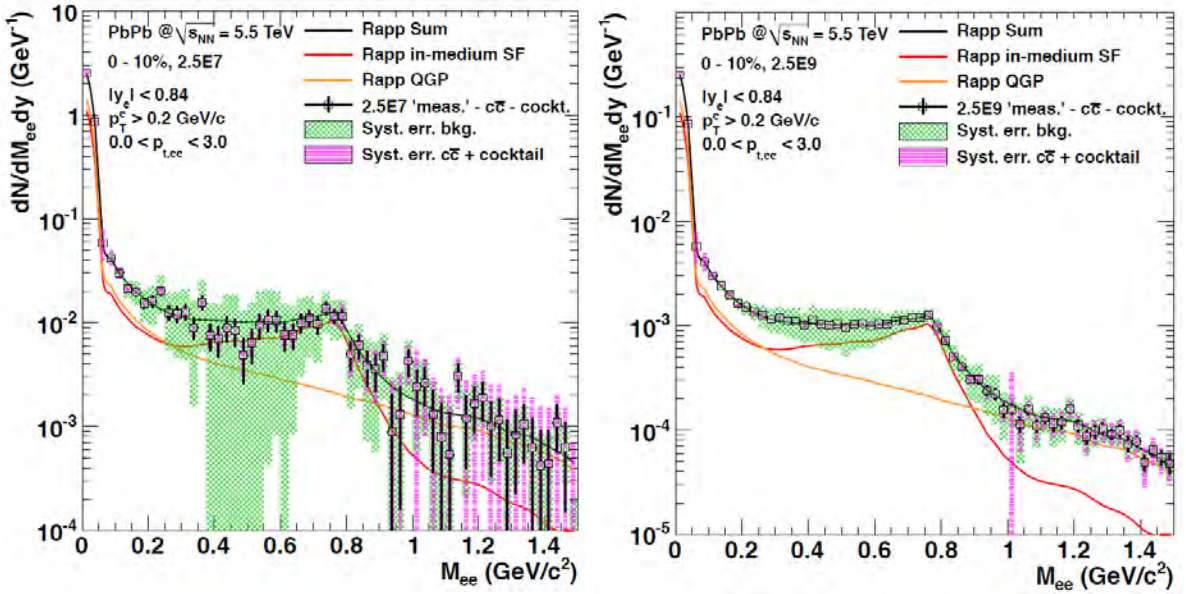

(a) (b)

Figure 2.12: Monte Carlo simulations showing the excess di-electrons invariant mass M_{ee} spectrum for Pb-Pb collisions at 0-10% centrality at $\sqrt{s_{NN}} = 5.5$ TeV with (a) $2.5 \cdot 10^7$ events analysed by the current ITS detector and (b) $2.5 \cdot 10^9$ events analysed by the new ITS detector [30]. The green bands are the systematic uncertainties from the combinatorial background subtraction whereas the magenta ones show systematic errors related to the subtraction of the cocktail and charm contribution.

The expected improvements are: the reduction of the charm identification uncertainties, a better separation between charm and beauty flavours, a complete reconstruction of B decays and precision measurements of heavy baryons.
As already mentioned in Sec. 1.3.2, quarkonia, among the various probes of deconfinement, play a distinctive role. Charmonium was the first hadron for which a clear mechanism of suppression was proposed in the quark gluon plasma.
Unfortunately the mechanisms of the generation of the J/Ψ, for instance, are not that simple so precision data are needed to extract information on the QGP properties and

on the amount of $c\bar{c}$ produced via regeneration.
The upgrades of the ITS and the TPC will also enable a high statistics measurement of low mass dileptons at mid-rapidity in Pb-Pb collisions, which will benefit from the low material budget and the enhanced low-p_T tracking capabilities of the new ITS, that will allow to further suppress combinatorial backgrounds (as clearly displayed in Fig. 2.12 thanks to di-electrons spectra simulated via Monte Carlo) from photon conversions and π^0 Dalitz decays ($e^+e^-\gamma$).
The analysis of low-mass dilepton production provides information about properties, such as the relevant degrees of freedom and the hadronic excitation spectrum in medium, and the space-time evolution of the hot and dense QCD matter.

2.2.2 The TPC upgrade

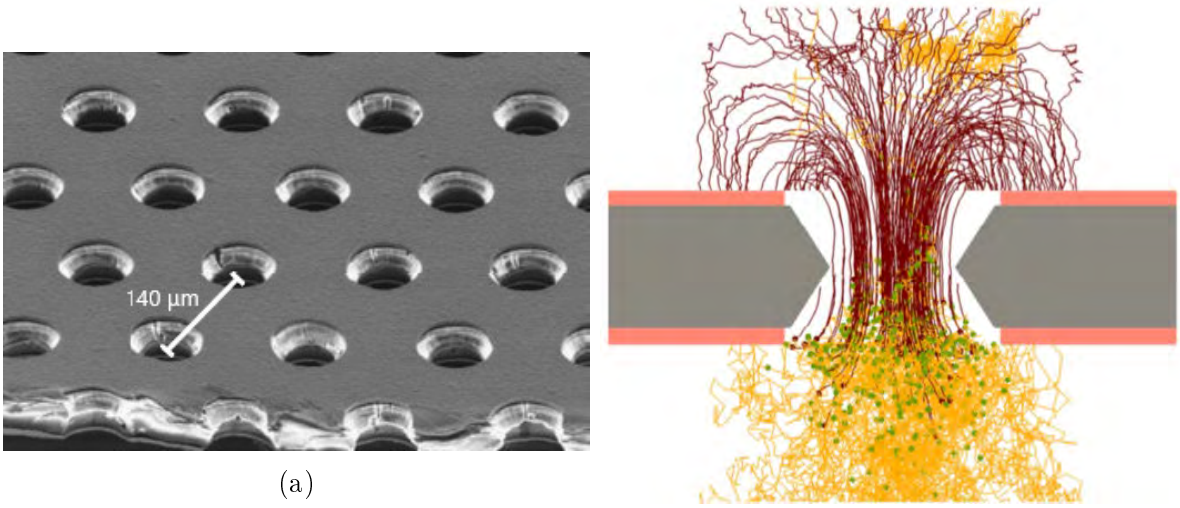

(a) (b)

Figure 2.13: (a) Electron microscope picture of a typical 50 μm thick GEM electrode with holes diameter of 70 μm, derived from [44]. (b) Illustration of a GEM simulation by the ALICE experiment where red and yellow lines correspond respectively to positive ions and electrons paths and the green dots show the position of ionization events [45].

A single GEM electrode (Fig. 2.13a) is a thin polymer foil metal-coated on both sides and pierced with a high density of holes [44]. This simple element, inserted between a drift and a charge collection electrode and with the applications of proper potentials, develops a series of field lines near the holes and a high field inside them, causing the electrons that drift inside the holes to achieve enough energy to ionize the gas molecules that fills the detector. The electrons obtained in the created avalanche drift to the collection electrode or they are transferred to another multiplying layer.
This way, as can be seen in Fig. 2.13b, slow positive ions are basically trapped and the negative signal on the anode is obtained only thanks to electrons collection.

In order to reduce the ion backflow[2] the readout system of the TPC will be based on four GEM stacked elements (Fig. 2.14), allowing the detector a continuous readout at a 50 kHz rate of lead-lead collisions, compared to the current MWPC limit of 3 kHz.

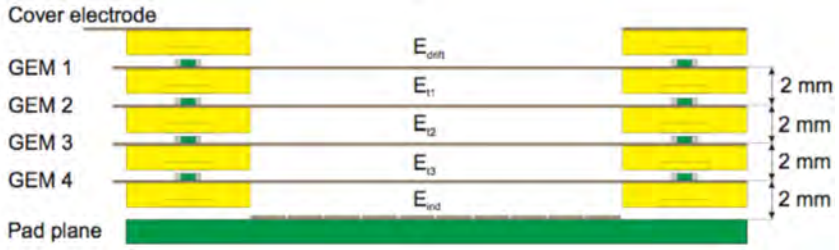

Figure 2.14: Schematic view of a 4-GEM stack [39].

2.2.3 TOF Readout Upgrade

Each of the 18 sectors of the TOF detector is read out by four VME crates, each containing 9 or 10 TDC (Time-to-Digital Converter) Readout Module (TRM) boards and one Data Readout Module (DRM) collecting their data.

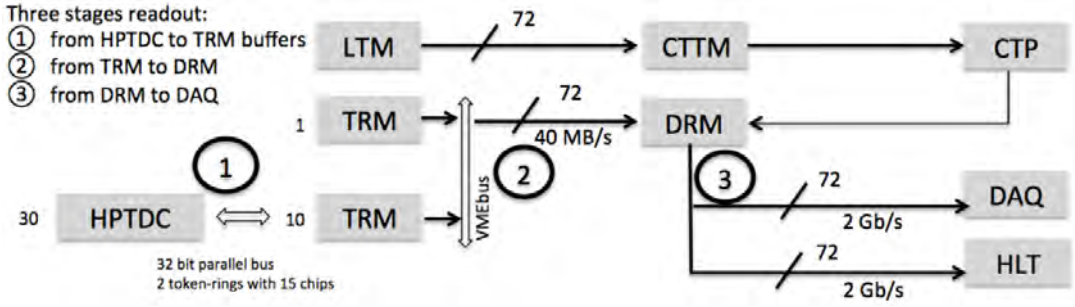

Figure 2.15: Current readout scheme of the TOF system [31, p. 92].

The readout procedure is divided in three phases which are shown in Fig. 2.15 and includes: the HPTDC (High Performance TDC) readout, which is the transfer of data from the chips internal buffers to TRM memories, the VME readout, where data is transferred from the TRM cards to the DRM via VME bus, and the DAQ readout, where DRM sends data to the DAQ via the DDL (Detector Data Links) link.
The LTM (Local Trigger Module) is an interface layer between the front-end electronics and the CTTM (Cosmic and Topology Trigger Module), which is the TOF central trigger board.
In order to cope with the increase of interaction rate a new board was designed, named DRM2, that features a faster link towards the DAQ system via the new GBTx ASIC [46] that manages to increase the data bandwidth up to 4.8 GB/s.

[2]It is the ratio of positive ions reaching the drift electrode to the electron charge detected in the anode.

The new board will replace the old DRM1 and also the CPDM (Clock and Pulser Distribution Module), that was used previously for the clock distribution, and will also feature the modern Flash based FPGA IGLOO2, replacing the older ProASIC3 and Cyclone V mounted on the DRM1.
Moreover the VME64 readout (40 MB/s) will be upgraded to VME64 2eSST protocol yielding to a data throughput of 160 MB/s (Fig. 2.16).
The new DRM2 card will be discussed in greater detail in the next chapter.

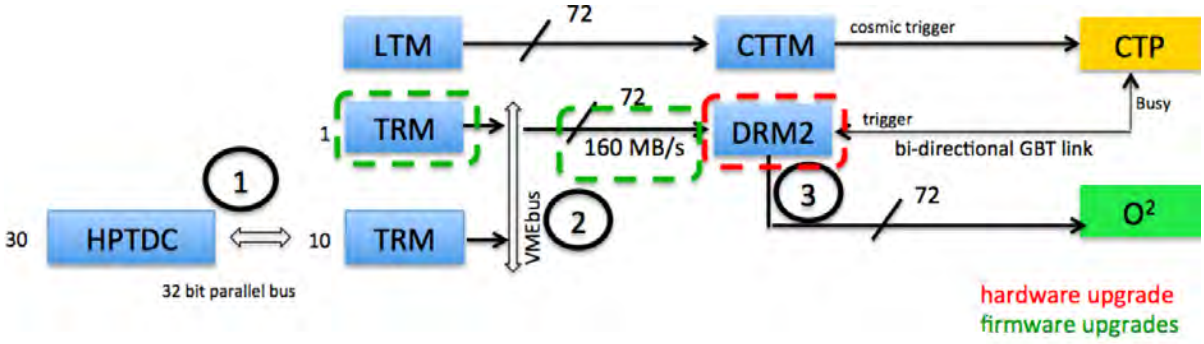

Figure 2.16: New readout scheme of the TOF system with upgraded elements highlighted [41].

The TOF detector, as for TPC, will also be operated in continuous readout mode. To achieve this the internal buffering capabilities of HPTDC will be fully used, a matching window of 30 μs will be employed and a trigger at fixed frequency of 33 kHz will be distributed.
In this way all hits will be readout. Events reconstruction, based on the Bunch ID and relative timing of the hits with respect to the trigger, will be made as part of the online processing. The feasibility of this readout scheme was discussed in [47].

Chapter 3

DRM2 board and test setup

The purpose of the test setup is to check and qualify the DRM2 board as delivered by the manufacturer. The main functionalities, including full data taking via GBTx link are tested as well as Slow Control accesses via CONET2 link.
In order to make this task simpler a test bench setup was prepared and will be described in this chapter.
This same setup was used both for the radiation tolerance test and for the acquisition one combined with the GUI software described in Ch. 4. In order to read a single DRM2 and several TRMs and to make the setup compact, inexpensive and portable we employed for our test a Xilinx KC705 evaluation board, without the complications of another PCI board (see sec. 3.2).

Figure 3.1: Front view of a custom running ALICE-TOF VME crate mounting in order from top to bottom: a DRM2, a LTM and 7 TRM boards.

The final setup that will be mounted at CERN includes 72 (4 per supermodule) custom water-cooled VME crates (Fig. 3.1) mounting a DRM2 board and up to 10 TRMs each.
Data are sent to a PCIe card, called CRU (Common Readout Unit) which is used by all ALICE detectors. For the TOF case, the CRU is equipped with 18 links. A Linux server hosts up to two CRUs, therefore the TOF detector is readout in total by two servers (called FLP, First Level Processors) having each two CRUs.
Moreover 18 servers mounting a PCI A3818 board, implementing 4 optical links, will allow monitoring and configuring of all the DRM2 and TRM boards via the CONET2 link[1].
For the Slow Control links this infrastructure is already in place with the current DRM1 card.

3.1 VME backplane

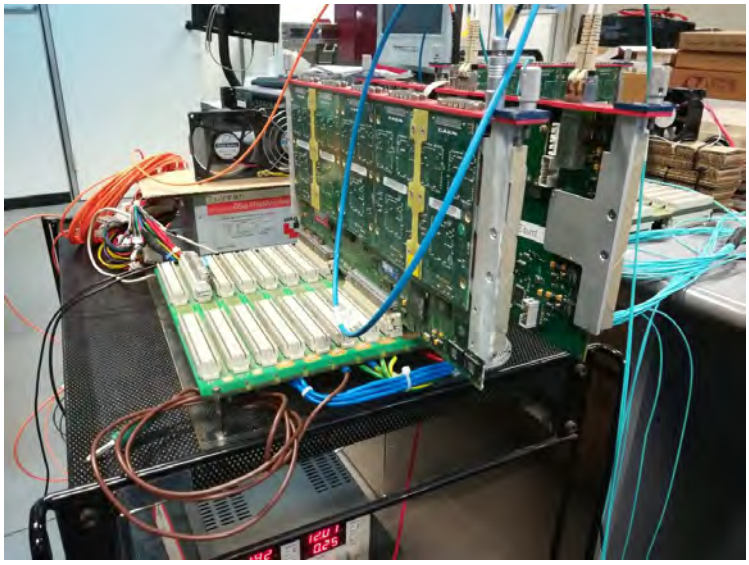

Figure 3.2: Picture of the test setup with a DRM2 board mounted on its first slot and a TRM on its fifth.

For the sake of simplicity, during the functioning test only the DRM2 board was connected, given that we needed to study specifically its characteristics, while the TRM boards were connected only aftwerdards while studying the data acquisition.
The DRM2 board was connected always to the first slot of the VME backplane acting as a VME master. The ALICE TOF makes extensive use of the user data pins available on

[1]the CONET2 link is a proprietary optical link data transmission protocol developed by CAEN and normally used to provide connection from a PCI card housed in a PC to an external card (a VME adapter or a standalone card as a digitizer). The DRM2 uses the CONET2 as a Slow Control link.

VME backplane on connector P2 (rows A and C) following the scheme detailed in Fig. 3.3.

A-row	From.. to..	PIN#	C-row	From.. to..
BUNCH_RESET	DRM -> all	1	N_BUNCH_RESET	DRM -> all
EVENT_RESET	DRM -> all	2	N_EVENT_RESET	DRM -> all
L1a	DRM -> all	3	N_L1a	DRM -> all
L1r	DRM -> all	4	N_L1r	DRM -> all
L0	DRM -> all	5	N_L0	DRM -> all
L2a	DRM -> all	6	N_L2a	DRM -> all
L2r	DRM -> all	7	N_L2r	DRM -> all
SPD	DRM -> all	8	N_SPD	DRM -> all
Not Used		9	Not Used	
/BUSY (WIRE-OR)	all -> DRM	10	/DRDY SLOT 2 (LTM)	LTM -> DRM
/DRDY SLOT 3	TRM3[1]->DRM	11	/DRDY SLOT 4	TRM4->DRM
/DRDY SLOT 5	TRM5->DRM	12	/DRDY SLOT 5	TRM6->DRM
/DRDY SLOT 7	TRM7->DRM	13	/DRDY SLOT 8	TRM8->DRM
/DRDY SLOT 9	TRM9->DRM	14	/DRDY SLOT 10	TRM10->DRM
/DRDY SLOT 11	TRM11->DRM	15	/DRDY SLOT 12	TRM12->DRM
PROG	DRM -> all	16	SYNC PULSE 0	DRM->LTM/CPDM
SYNC PULSE 1	DRM->LTM/CPDM	17	SYNC PULSE 2	DRM->LTM/CPDM
FORCE CLK INT	DRM->CPDM	18	LHC CLK STATUS	CPDM->DRM
SPSE0	DRM -> all	19	SPSEI	all -> DRM
PULSE TOGGLE	DRM->LTM	20	LTM LOCAL TRG	LTM -> DRM
/ON 1	LV_ctrl->DRM	21	/ON 2	LV_ctrl->LTM
/ON 3	LV_ctrl->TRM3[1]	22	/ON 4	LV_ctrl->TRM4
/ON 5	LV_ctrl->TRM5	23	/ON 6	LV_ctrl->TRM6
/ON 7	LV_ctrl->TRM7	24	/ON 8	LV_ctrl->TRM8
/ON 9	LV_ctrl->TRM9	25	/ON 10	LV_ctrl->TRM10
/ON 11	LV_ctrl->TRM11	26	/ON 12	LV_ctrl->TRM12
/FAULT 1	DRM->LV_ctrl	27	/FAULT 2	LTM ->LV_ctrl[2]
/FAULT 3	TRM3[1]->LV_ctrl[2]	28	/FAULT 4	TRM4->LV_ctrl[2]
/FAULT 5	TRM5->LV_ctrl[2]	29	/FAULT 6	TRM6->LV_ctrl[2]
/FAULT 7	TRM7->LV_ctrl[2]	30	/FAULT 8	TRM8->LV_ctrl[2]
/FAULT 9	TRM9->LV_ctrl[2]	31	/FAULT 10	TRM10->LV_ctrl[2]
/FAULT 11	TRM11->LV_ctrl[2]	32	/FAULT 12	TRM12->LV_ctrl[2]

Figure 3.3: Scheme of connector P2 data pins usage.

These pins include signals for synchronization (event reset, bunch reset), triggers (L0, L1a/r, L2a/r), readout (data ready asserted by each VME slave module), status (fail) read by the DRM2 or by the power system in the custom VME crate.

Figure 3.4: Power supply used for the VME backplane.

In the test setup, the slots can be used to test TRM cards, but the last one that was connected to a termination circuit (since some of the signals, like bunch and event reset,

are PECL differential and need to be appropriately terminated at the end of the VME bus and others need pull-up or pull-down resistors).
A simple 520 W computer power supply (Fig. 3.4), adapted for the task, was used to power up the entire VME backplane, hence giving power to the boards connected to it. The TRM and DRM2 boards have respectively a power consumption of 10 A and 3 A at 3.3 V, conditions satisfied by the power supply which is able to deliver 32 A at 3.3 V. The 5 V output is also used to power some components installed on the VME backplane.

3.1.1 TRM

The TDC Readout Module VME board has the task to perform the time digitisation in the TOF detector [48]. It hosts 30 High Performance TDC (HPTDC) ASIC, which were developed by CERN/EP Microelectronic group for LHC applications and were designed to be capable of handling high instantaneous rates, multi-hit and multi-event conditions [49].

Figure 3.5: Three-quarter view of TRM board.

The ASIC returns relative time measurement of each hit at external trigger arrival. If used in its Very High Resolution Mode, as for the TOF, the ASIC integrates 8 channel per chip, compared to the 32 in the lower resolution mode, and the board allows to achieve a time resolution of 20 ps applying Integral Non-Linearity correction, as demonstrated by bench and beam tests [48].
The HPTDC are organized in the card in two separate 32-bit parallel chains and an FPGA acts as readout controller and implements also the VME interface.
Two fans, powered by an external general purpose power supply, were used to cool down the TRM for our tests, while a water cooling system is used in the ALICE-TOF crate.

3.1.2 DRM2

The Data Readout Module 2 (DRM2) is the new version of the readout board of the ALICE-TOF detector and it is able to read the data coming from the TRM boards via VME bus.

The card hosts a Microsemi Flash-based Igloo2 FPGA that provides the main programmable logic, via VHDL code.
As already mentioned, the GBTx ASIC [46] and VTRx radiation hard optical transceiver (developed by CERN) are used for the faster link towards the DAQ system reaching a bandwidth of 4.8 Gb/s. This same link is used also for receiving triggers and a low-jitter clock, which is distributed to the front-end electronics and whose quality is very important for the TOF detector[2] since it is used for high resolution timing measurements on the HPTDC chips of the TRM [51].

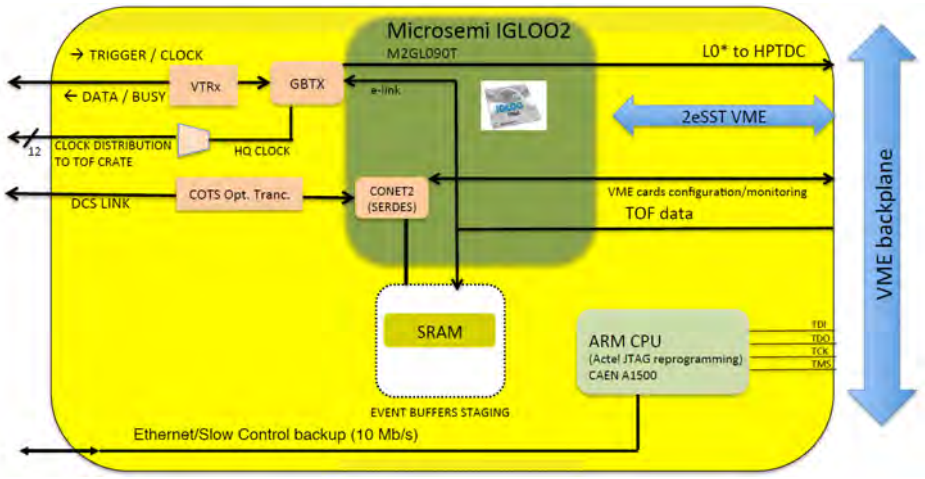

Figure 3.6: Schematic drawing of a DRM2 board design.

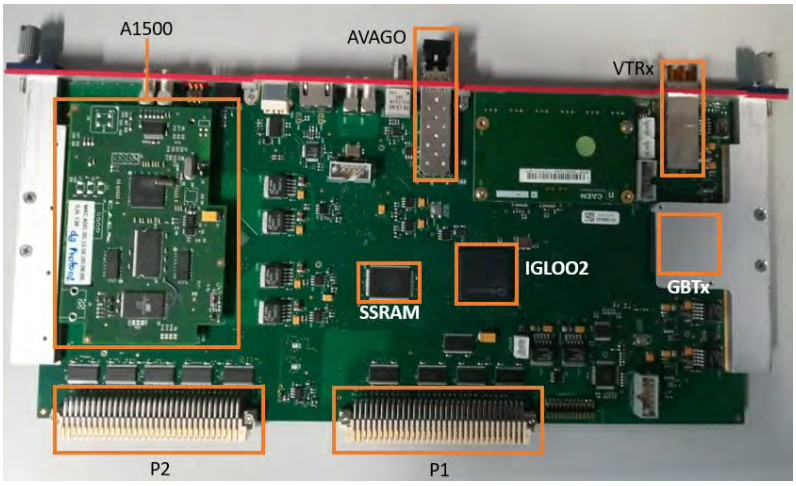

Figure 3.7: Front view of a DRM2 board mounted on the VME with main components highlighted.

[2]A series of measurements on the clock received from the ALICE DAQ card CRU [50] have demonstrated the compatibility of the TOF requirements by determining that the RMS clock jitter is as low as O(10) ps.

A 1Mb×36 SSRAM module is connected to the IGLOO2 and it is used to buffer words from the TRMs followed by the event header.
The GBTx link has a data bandwidth towards the CRU of 400 MB/s and the same bandwidth viceversa for receiving triggers and their information (80 bits per each 40 MHz clock cycle).
The data flow inside the DRM2 can be summarised through these steps (Fig. 3.8):

1. the GBTx link receives a trigger and sends it to the TRM via the VME backplane on the custom bus defined in the P2 connectors;

2. the board reads the data of each TRM and stores them on the SSRAM of the device;

3. the event is read out from the SSRAM and sent to the CRU through GBTx link.

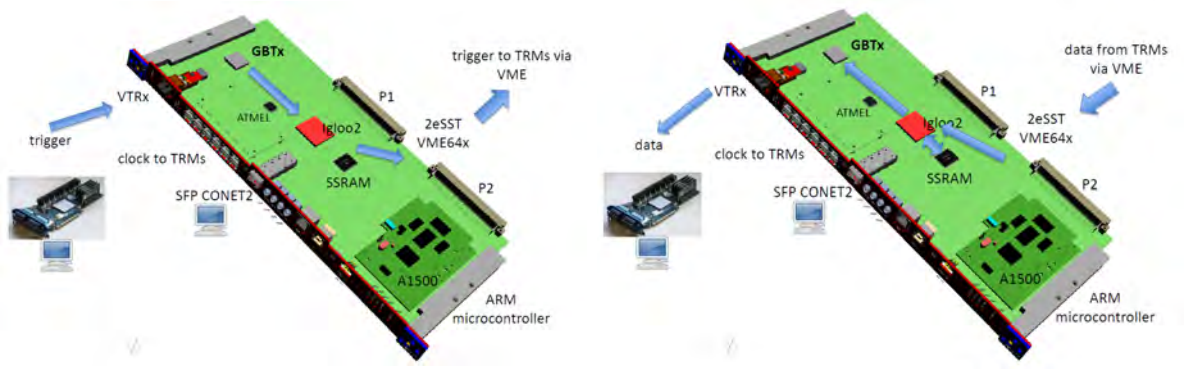

(a) (b)

Figure 3.8: Trigger (a) and Data (b) flows inside a DRM2 board [52].

The implementation of the 2eSST VME64x protocol allows the DRM2 to readout the data from the VME slaves (the TRMs in this case) as 64 bit words on both rising and falling edges of the Data Acknowledge signal (DTACK) leading to a 160 MB/s peak VME data throughput.
The board maintains also two slow control links, installed previously on the DRM1 board [51]: a 1.28 Gb/s serial link (CONET2), used to configure the TRM boards and registers monitoring, and an Atmel ARM processor running Linux on a commercial mezzanine named A1500 by CAEN, used for re-programming remotely the IGLOO2 FPGA and TRM FPGAs via JTAG through an Ethernet link. The CONET2 link is implemented on the IGLOO2 internal high speed SERDES, as opposed to the DRM1 which had a dedicated SERDES chip; it adopts a commercial AVAGO optical transceiver mounted on the board and it is implemented on the receiving Linux server through a 4-link A3818 CAEN PCIe CONET2 controller board.

3.1.3 GBTx

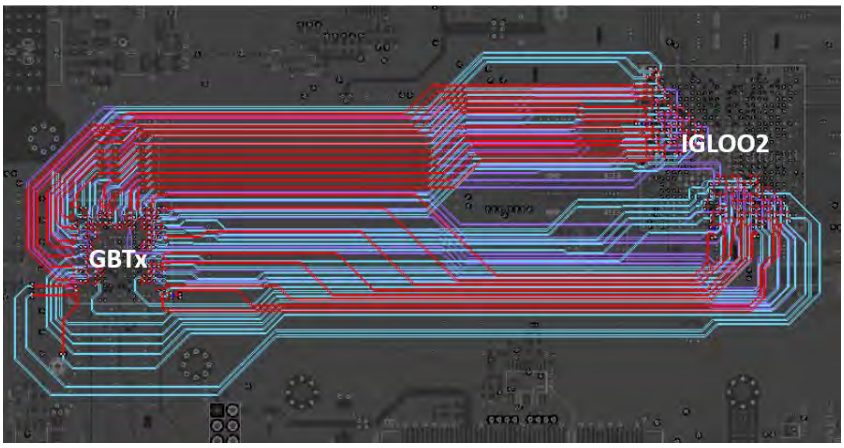

Figure 3.9: Direct data connection between GBTx and IGLOO2 [52].

The GBTx is a radiation tolerant chip implementing multipurpose high speed bidirectional optical links for high energy physics experiments [53].
The chip provides three logical paths for Timing and Trigger Control (TTC), Data Acquisition (DAQ) and Slow Control (SC) information, that are merged on a single optical link allowing a bidirectional link to be used for all these functions.
The GBTx chip is connected directly to the IGLOO2 FPGA on the DRM2 board, without any polarization resistors in both directions (Fig. 3.9).
A 120-bit frame of data is transmitted by the GBTx during a single bunch crossing interval, thus every 25 ns, resulting in a bandwidth of 4.8 Gb/s. The frame is characterised by:

- 4 bits for the header;
- 32 bits for Forward Error Correction (FEC);
- 4 bits for SC information;
- 80 payload bits used for data transmission.

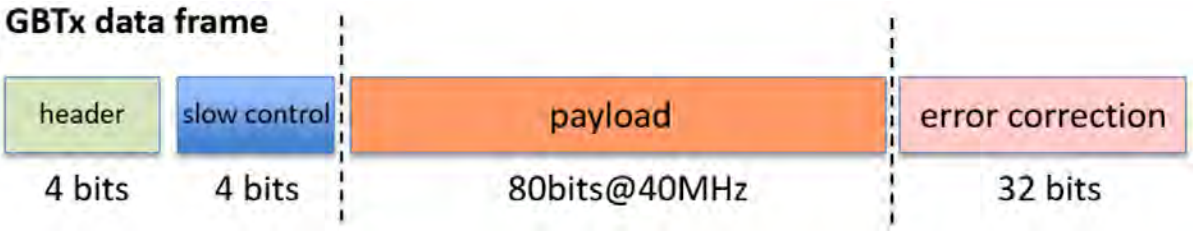

Figure 3.10: GBTx data frame structure [52].

The payload section is not pre-assigned and can be used for DAQ, TTC or Control purposes (Fig. 3.10) [53].

3.2 DAQ and Clock

In order to test the DAQ functionalities of the board and to send it the clock signal we used two COTS boards:

1. Xilinx KC705 rev 1.2 evaluation board featuring a Kintex-7 FPGA, that was used to implement the connection between the DRM2 board and the Linux server;

2. Si5341 Clock Generator Development Kit rev 2.1 by Silicon Labs, which provides a high quality 120 MHz clock needed by the KC705 card to implement a FPGA counterpart of the GBTX link.

Actually the setup included also an additional VME crate (Fig. 3.12) with some TTC boards, in particular they are a LTU (Local Trigger Unit) and a TTCex (Timing, Trigger and Control Encoder/Transmitter) board, acting as an electric/optical converter, that could be used to provide 40 MHz LHC clock to the DRM2 in our setup.
In the final setup the KC705 will not be employed, the 72 DRM2 boards, as already mentioned, will be connected directly to the CRU PCIe boards and the GBTx clock will be obtained from the LHC clock itself.

Figure 3.11: KC705 and Si5341 used for the tests and mounted on a aluminium base specially designed to host them.

Figure 3.12: Additional VME crate that provided LHC clock to the DRM2.

3.2.1 Si5341

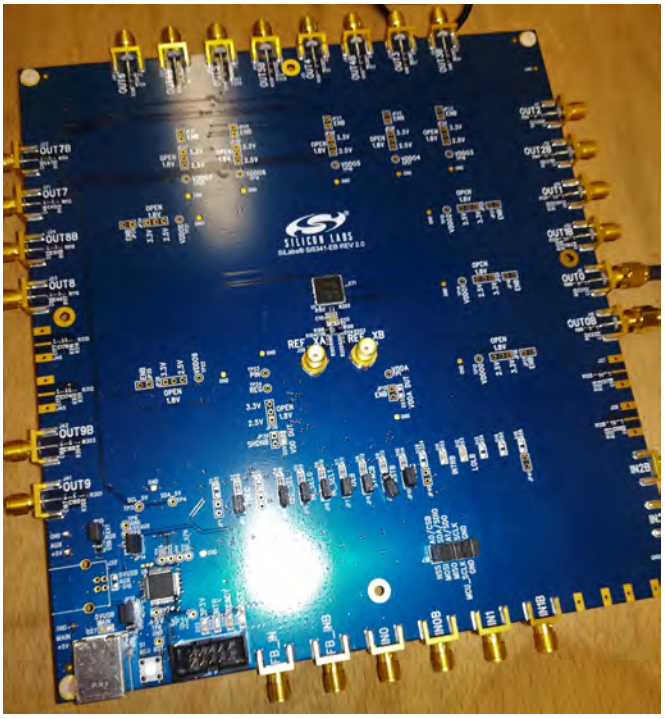

Figure 3.13: Si5341 Clock generator evaluation board.

The Silicon Labs Clock Generator Development Kit was programmed with a firmware made for this purpose using the commercial software ClockBuilder Pro for Windows OS. The board is designed to generate any-frequency clock with ultra low jitter [54].
For our setup only the output OUT0 and OUT0B were used and the device was also programmed in the end using its nonvolatile memory (NVM), via serial interface, so to have a 120 MHz frequency configuration at power-on without the need to use a Windows machine.

3.2.2 KC705

The Xilinx evaluation board has been used to implement the GBTx-FPGA core link and the communication via Ethernet link through UDP protocol between the Linux server and the DRM2 board (Fig. 3.14).
For this purpose a custom firmware was developed using the commercial software Vivado Design Suite and VHDL language.
This software runs on Windows OS, so, when we had a functioning firmware, the board was programmed using its nonvolatile flash memory (it contains two 128 MB flash memory modules that can be used both for configuration and data storage).

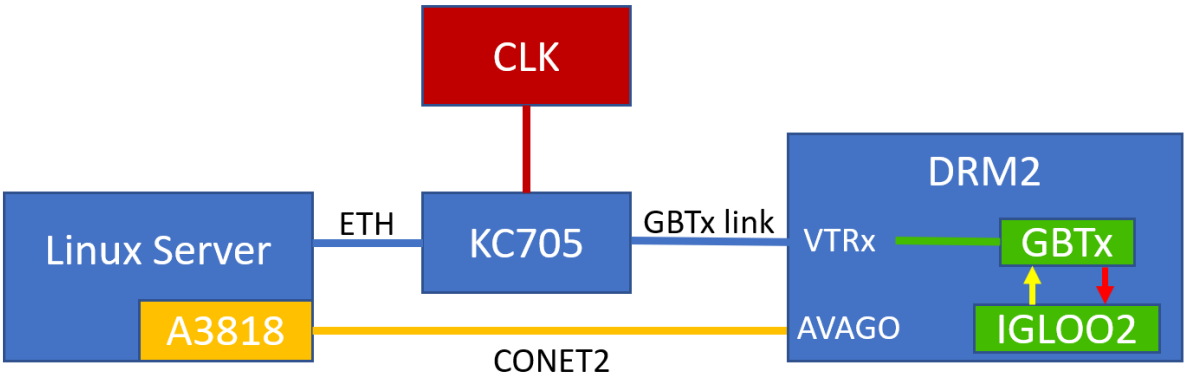

Figure 3.14: Schematic logic view of the test setup.

The KC705 is connected to the Si5341 via two coaxial SMA cables to the two SMA Clock Input [55].
The connection to the DRM2 is through GBTx link, the board is programmed through Vivado via mini USB cable and UDP data are read via LAN on the Linux server.
The board can be reset remotely or through two hardware buttons (one reloads the firmware from the volatile memory, the other reloads the configuration file from the flash memory).

Figure 3.15: Xilinx KC705 evaluation board.

Chapter 4

Monitoring and DAQ software

The development of a software framework to handle the test and programming of DRM2 components has been one of the central tasks of my work.
The programs developed will be used by operators at the manufacturer or at CERN to validate the cards. They are not particular experts of the GBTx programming, therefore I developed an interface to overcome this problem.
The setup needed also to be *compact*, so I developed it just using one operating system (Linux), given this is the one used by TOF for the CONET2 interface.
For my thesis project I studied the software that were partially developed to complete these tasks and made my own using Python language. Before them a Labview software was used to monitor registers and burn the DRM2 eFUSE and a GUI application, created through the Windows Forms Application method in Visual Studio using C#, was used to get data via UDP protocol from the DRM2.
I used a Scientific Linux CERN 6 distribution and a 2.6.6 version of Python.
There are a series of reasons why the language chosen for these application is Python:

- high compatibility with the C language: an important part of the code connected to the basic read and write of the registers was already written in C and linked to C libraries that could be loaded inside the Python software thanks to one of the library of the language, called *ctypes*;

- handles very well GUI development: the language contains a huge number of GUI frameworks and the chosen one, *Tkinter* which is bundled with a normal installation of Python, is efficient, light and really easy to use;

- platform independent: for the most part of the tests the Linux server was used to run the GUI applications, but some initial ones were also made using a Windows notebook and little to no efforts were required to run the software also on the latter[1].

[1]The Tkinter package required just a three-line function at the end of the application to make it run properly on Windows.

The GUI work successfully thanks to a series of software layers implementations which are shown in Fig. 4.1. For the UDP part, the Python code uses an interface for UDP packet management available in Python libraries, that in turn accesses the related network layer of the Linux kernel managing the networking. For the access via CONET2 the custom code is concentrated in two dynamic libraries, written in C, to access GBTx and other general registers of the DRM2 via access over CONET2 link. For this purpose the library provided by the manufacturer of the A3818 card is called CAENVME that in turn interfaces with the A3818 driver loaded in the Linux kernel.

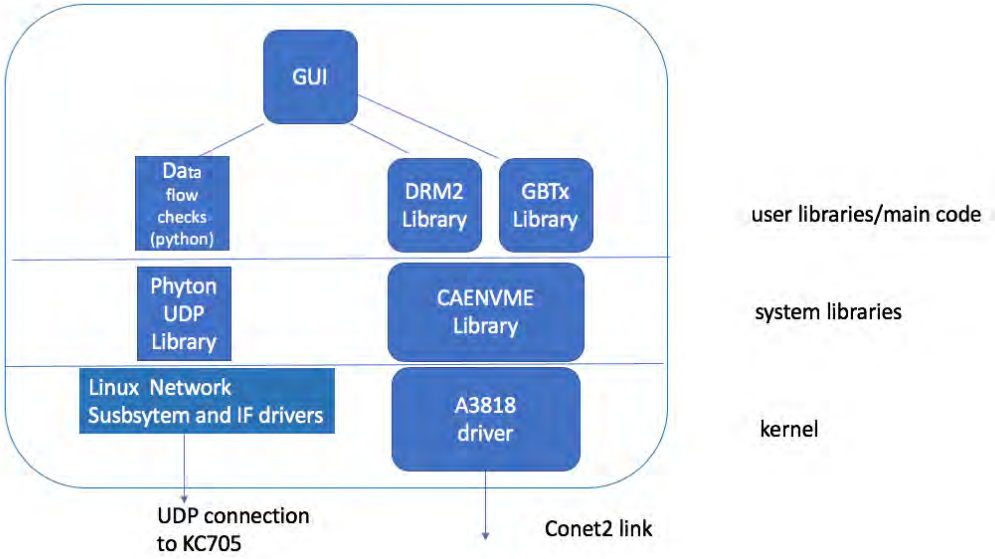

Figure 4.1: Software layers of the two developed GUI.

The Direct Control Manager needs the physical connection of the A3818 CONET2 link to retrieve the registers data, while the UDPConnet needs the KC705 board connected via GBTx link to the DRM2 and via LAN to the Linux server (Fig. 4.2) and it uses also the CONET2 link to configure the TRM boards.
Several tests were performed on these software both in Bologna and at CAEN (Viareggio), proving their stability and efficiency. In particular in Bologna we tested the monitoring capabilities of the DRM2 which logged temperature and voltage values for a whole day without crashing, checking repeatedly whether the information obtained were the same as the one obtained with previous functioning terminal applications; we tested the UDPConnect data acquisition and data writing capabilities using various configurations and for different time intervals (up to a 24 hours test); we checked if the pulses sent by the eFUSE (see sec. 4.2) programmer had the correct width and frequency thanks to an oscilloscope and, at last, we successfully programmed some DRM2 boards eFUSE both in Bologna and at CAEN.

Figure 4.2: Schematic view of the physical connections needed to make the GUI software on the server work. A single or multiple TRMs can be connected via VME to the DRM2.

4.1 Tkinter

Before talking about the developed software, a brief introduction to the built-in graphical user interface (GUI) package for all standard Python distributions is mandatory.
Tkinter is the standard Python interface to Tk. This is the GUI toolkit for Tcl/Tk [56], which is the combination of the high-level, general-purpose and interpreted programming language Tcl (Tool Command Language) with the Tk extension. The former is a very simple but powerful language commonly used for scripted applications and GUIs, while the latter is an open-source, cross platform widget toolkit containing a library of GUI widgets needed to develop desktop applications, such as buttons, labels, etc.
Tkinter is implemented as the Python module *Tkinter.py*, which is just a wrapper[2] around a C-extension using Tcl/Tk libraries [57].
Among the Python GUI frameworks, Tkinter is an easy one to code fast complex and powerful interfaces using few lines and commands. The choice of creating graphical applications, instead of simple console scripts, was made to ensure the user-friendliness of the procedures.

4.2 Monitoring and Programming: Direct Control Manager

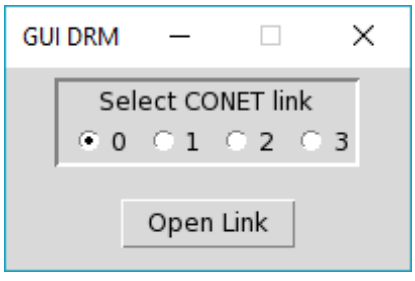

Figure 4.3: Start window and CONET2 link selection of the DRM.

[2] *Wrapping* is one of the procedures that permits Python to execute C/C++ code.

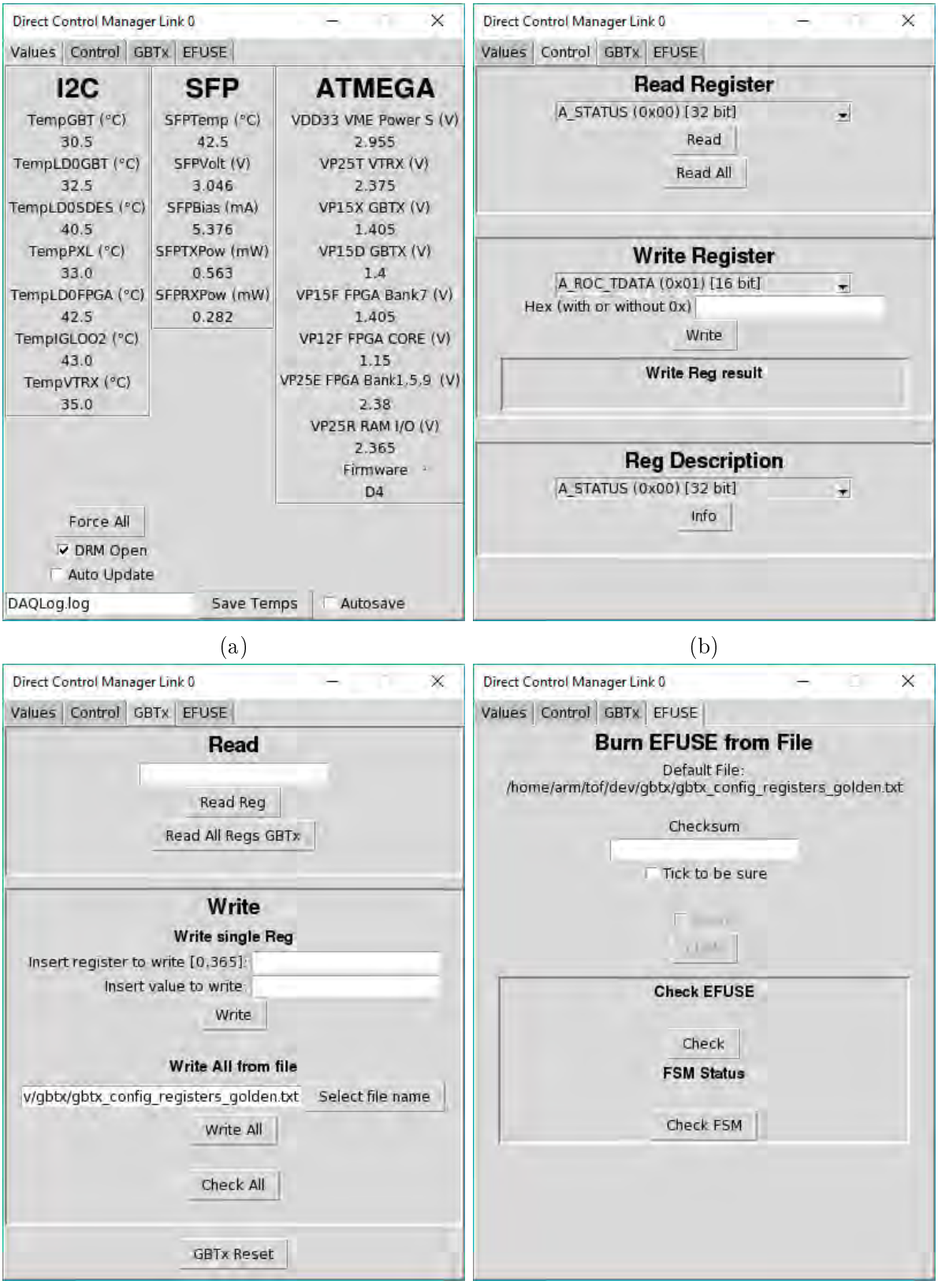

Figure 4.4: Control Manager tabs allowing the user to: (a) monitor the main temperatures, voltages and currents of the board; (b) read/write IGLOO2 registers; (c) read/write GBTx registers; (d) program eFUSE.

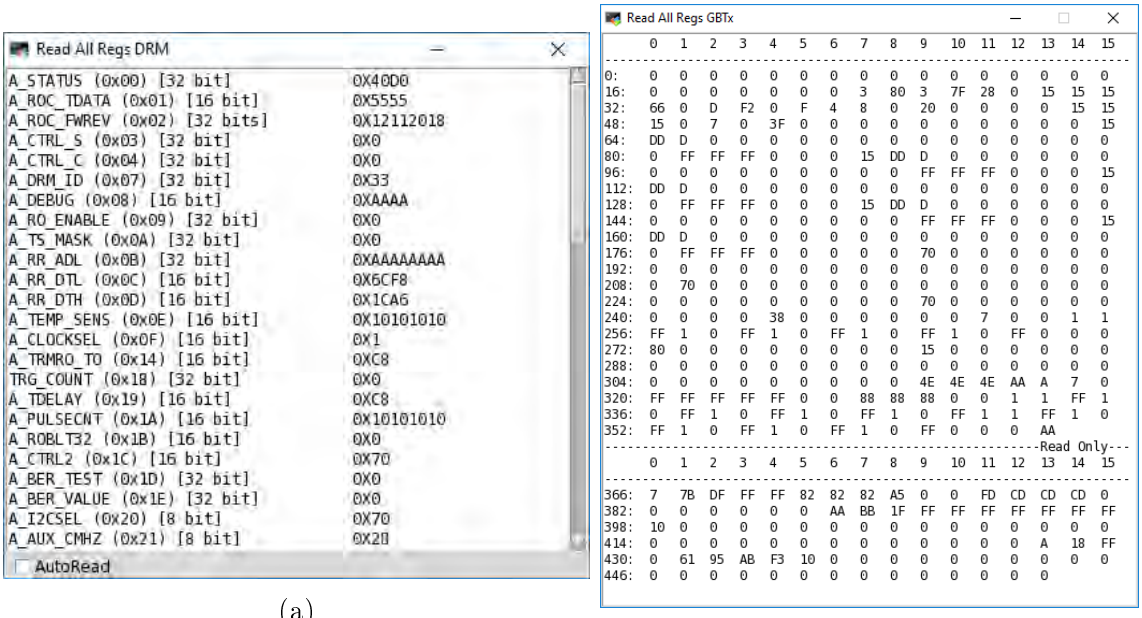

(a) (b)

Figure 4.5: Windows opened from commands in the Control Manager that allows reading all registers of (a) IGLOO2 and (b) GBTx.

The first developed software was the Direct Control Manager that basically allows the user to check, write and read every single register on the DRM2 board.
In order to make it work the CONET2 link of the A3818 server card must be connected to the DRM2 AVAGO and the link on the starting window of the program must be selected and opened through the dedicated button (Fig. 4.3).

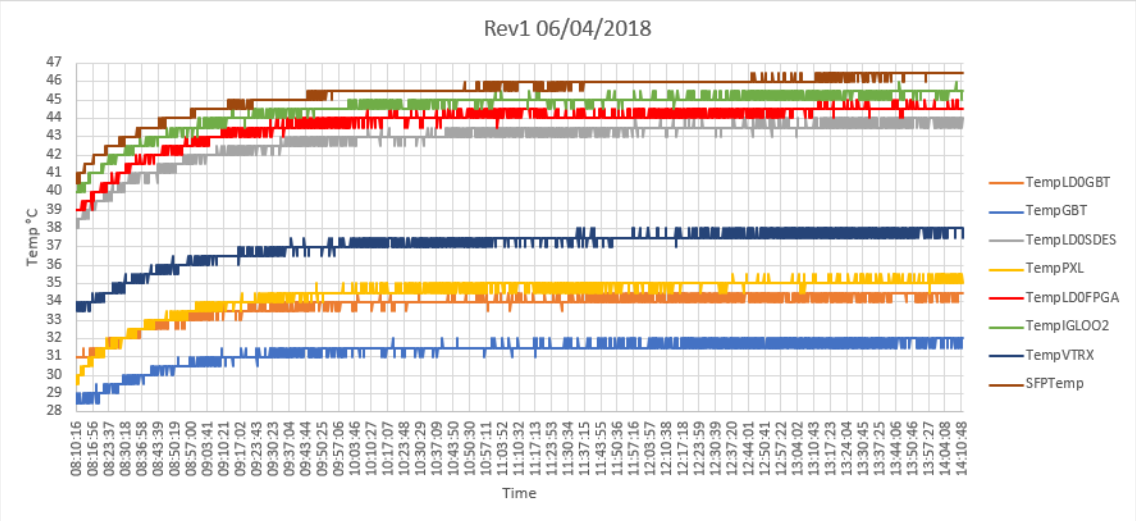

Figure 4.6: Temperatures Log analysis of a full crate containing a DRM2 rev1 on a 6 hour running test.

This procedure includes a series of functions called from the C dynamic libraries, layered on top of the CAENVME library (access via CONET2).
Opening the link will cause a Top Level window to pop up (Fig. 4.4a), whose title contains the number of the opened link. From here on, the application was developed using different tabs that perform different tasks (Fig. 4.4).
The first tab lets the user to check several important monitoring values including temperatures, voltages and current values of the DRM2 board, like the average temperature of the IGLOO2 and of the CONET2 optical transceiver, which are obtained via I^2C serial protocol thanks to two different sensors which are the AD7416AR3 (made by Analog Devices) for the former and an internal SFP one for the latter. All these values can be stored in a log file, providing data for further analysis, as done for the analysis shown in Fig. 4.6 where a full water-cooled crate with a DRM2 and 9 TRMs was tested while acquiring data for 6 hours.
The second tab allows one to read/write the DRM2 IGLOO2 registers and returns also information about them through the last specific module visible in Fig. 4.4b.
The third tab reads/writes every GBTx registers either individually or together and allows programming the GBTx via file. A defined button lets also the user to quickly force reset the GBTx in case of error.
All GBTx and IGLOO2 registers can be read simultaneously by pressing specific buttons in their dedicated tabs, showing new windows like those in Fig. 4.5.
The last tab is dedicated to the burning of the eFUSE that can store the GBTx configuration file in order to program it at power-on without the need of external configuration loading.

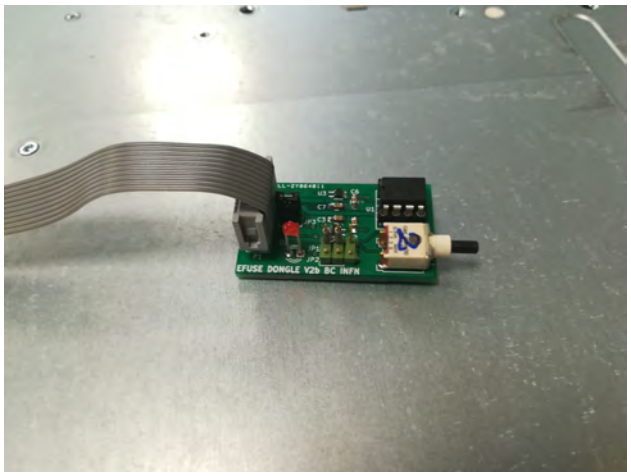

Figure 4.7: eFUSE Dongle.

4.2.1 eFUSE Programming

The DRM eFUSE are an array of fuses organized in bytes. Each one of them can be programmed to contain a default value of the GBTx registers that will be loaded at

power-on or reboot.
Given that eFUSE can be programmed just once, a rigid protocol (Fig. 4.8) must be followed in order to do so and several security options are implemented to avoid user errors: firstly a dongle (Fig. 4.7) has been developed and must be connected in order to receive the 3.3 V voltage needed to burn them, otherwise, even though the user reaches the end of the software procedures, the operation will fail; then the GBTx must be programmed temporarily using the form in the third tab (Fig. 4.4c) from which a checksum is obtained if the registers on the file correspond exactly to the one just written inside the GBTx; finally writing the checksum value inside the last tab specific entry allows the software to program the eFUSE after checking if the selected file is the one used in the previous step.

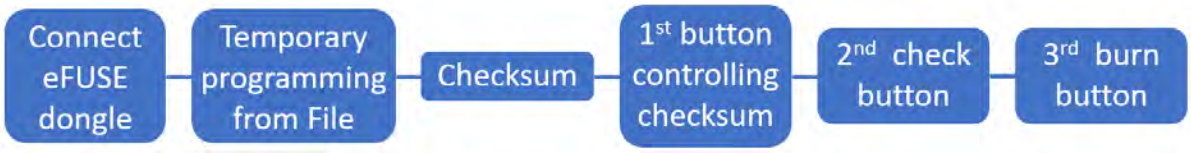

Figure 4.8: Security protocol for the eFUSE burning.

Once the dongle is connected (Fig. 4.9) and the last button of the protocol is pressed, the IGLOO2 register EFUSECTRL (address 0x48) is used to control the programming process thanks to the IGLOO2 signals EFUSEENAB (which enables the 3.3 V sent to the EFUSEPOWER pin of the GBTx) and EFUSESYNC (which gives the pulse whose rising edge will be used by the dongle to generate the programming pulse), following this list of operations, as programmed in the software:

1. a 'v' is written inside EFUSECTRL, so the EFUSEENAB signal switches to '1' enabling the 3.3 V on EFUSEPOWER;

2. the address of the register to be programmed is written on GBTx registers 238 and 239 (the address is a 9 bits word, so the LSBs are written on the former and the MSB[3] on the latter);

3. the register value is written on the GBTx register 240;

4. the programming is activated by writing a 'p' on EFUSECTRL, hence the EFUSESYNC activates making the EFUSE DONGLE generate a 200 μs pulse on its rising edge, sent to the EFUSEPROGRAMPULSE input of the GBTx;

5. EFUSESYNC resets automatically and EFUSECTRL shows again the 'v' value;

6. the procedure is repeated from step 2 to 5 from register 0 to 365 and the programming process ends writing a 0x07 on register 366 of the GBTx;

7. a 'd' is written inside EFUSECTRL to disable the programming voltage.

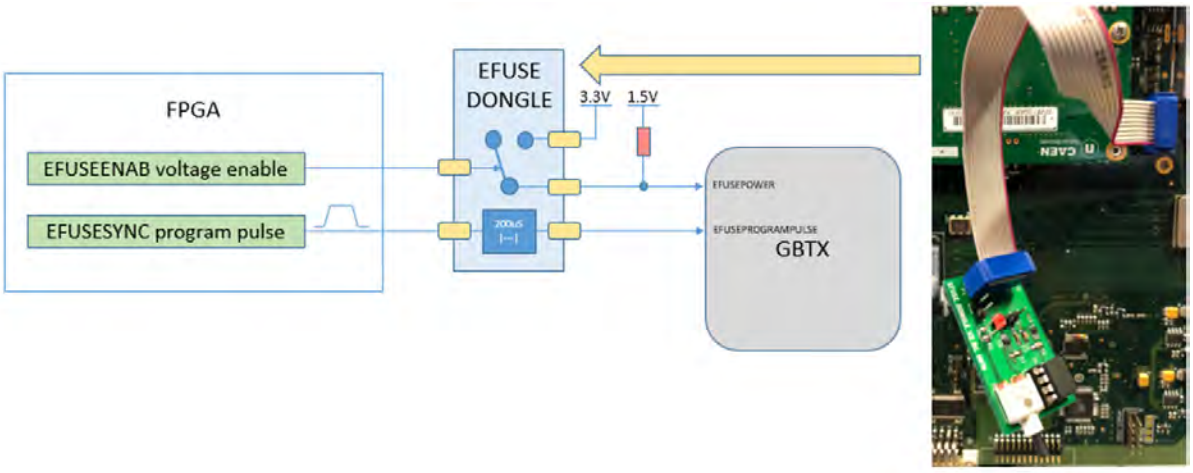

Figure 4.9: Schematic drawing of the eFUSE programming components involved.

The procedure ends with an automatic GBTx reset, after which the configuration data inside the programmed eFUSE will be loaded, and a text label[4] in the last tab, shown when the specific 'Check' button is pressed, will assure if the device has been permanently programmed or not, by reading the value of register 366 (Fig. 4.4d).

4.3 Data Acquisition: UDPConnect

The second application developed is the one related to the acquisition of DRM2 data, obtained from the TRM boards, via UDP protocol.
User Datagram Protocol (UDP) is a simple internet protocol that allows computer applications to send messages (in datagram units which are structured in header at the beginning of the message and payload afterwards) among communicating devices [58].
UDP provides error detection and checksums for data integrity, but its functions do not include error correction, duplicates elimination or flow control. The protocol was chosen for the application because it lets the user to have a great deal of control over how packets are sent and processed, despite having no handshaking[5] dialogues, making the delivery of the data unreliable if no protections are implemented by the user.
The UDP communication required the joined work on the Python software and on the VHDL firmware of the KC705, which was developed intentionally for this purpose.
The KC705 is connected to the DRM2 board via GBTx link and via LAN to the Linux server. Data are transferred from the TRM to the DRM2 via VME bus, from the DRM2 to the KC705 via optical link and finally to the server via LAN (1 Gb/s $\approx$ 110 MB/s), as in Fig. 4.2.

[3]Least and Most significant bits.
[4]'BURNT' if permanently programmed and 'CLEAN' otherwise.
[5]It is an automated process of negotiation between two communicating participants establishing rules for communication between them.

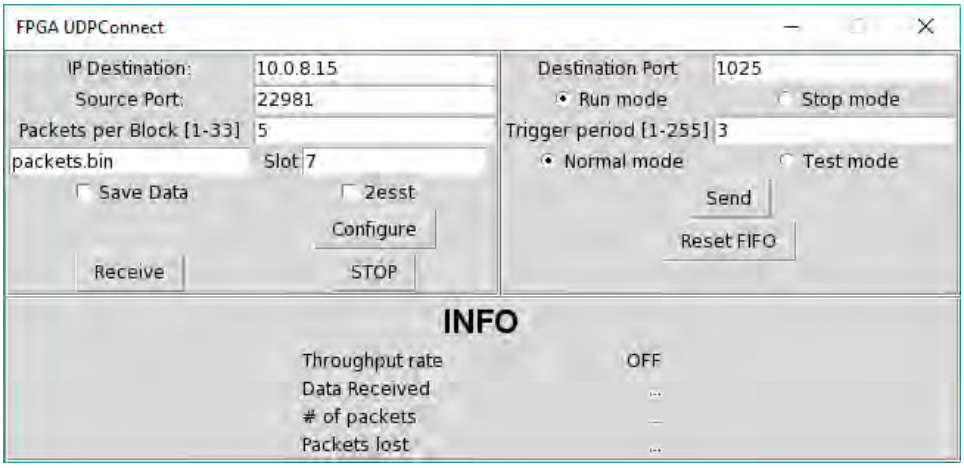

Figure 4.10: Root window of the UDPConnect software.

The application opens the two UDP sockets (one to receive data and the other to send them) by including the IP of the KC705 board and the source/destination port, which are defined also into the board firmware. In order to have communication, the MAC address of the network interface of the server must be also included into the firmware itself.

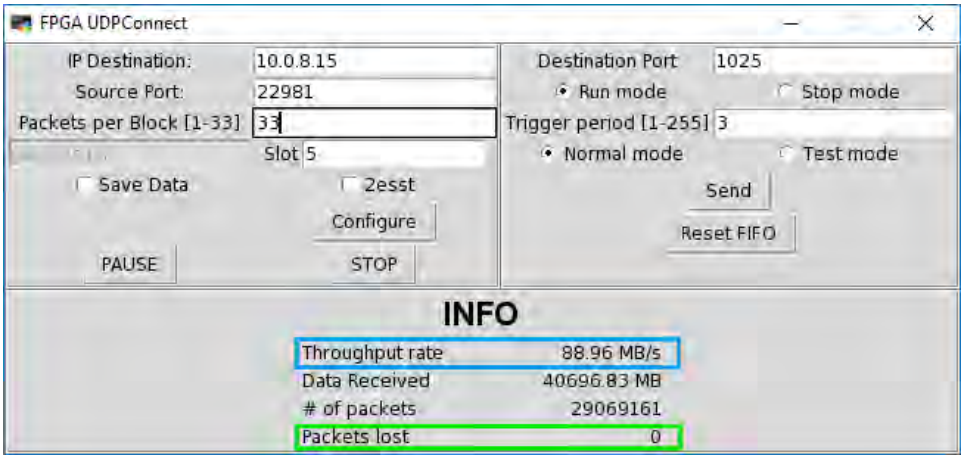

Figure 4.11: Running test mode on UDPConnect, with throughput rate (cyan) and number of packets lost (green) highlighted.

The application allows the user to use a test mode, where several counters are sent continuously to the KC705, in order to analyse the maximum throughput rate and to check if the connection is set properly between the board and the server. The first version of the software, which basically obtained data without any kind of online analysis or lost packets control, returned a throughput rate on test mode of ≈ 105 MB/s, while the current upgraded one showed a rate of ≈ 90 MB/s (Fig. 4.11), which is ≈ 20 MB/s less than the LAN capabilities. This decrease is essentially due to the checks and controls

implemented in the new application.
TRM boards data are instead collected using the Normal Mode of the software, that lets one to set on which slots are connected the boards (providing that the first one is occupied by the DRM2) and to configure them for data acquisition through the specific button (for our tests we made them simulate a series of realistic hits).
A button that allows resetting the KC705 state machine and its FIFO is also implemented in the software.
The UDPConnect lets the user decide also the trigger rate and data are sent by the evaluation board in blocks containing a custom number (from 1 to 33)[6] of packets, defined by the dedicated entry in the application, each of 1400 bytes.
The trigger rate is calculated from the trigger period the user sets in the GUI (1-255). This number is considered as the MSBs of a 16 bit number containing FF as LSBs, meaning that if we choose 255 (0xFF) there will be a trigger after 65536 (0xFFFF +1) 25 ns clock cycles, meaning a trigger rate of ≈610 Hz (minimum settable value). The maximum obtainable rate is ≈78 kHz, with a trigger period of 0x1FF.

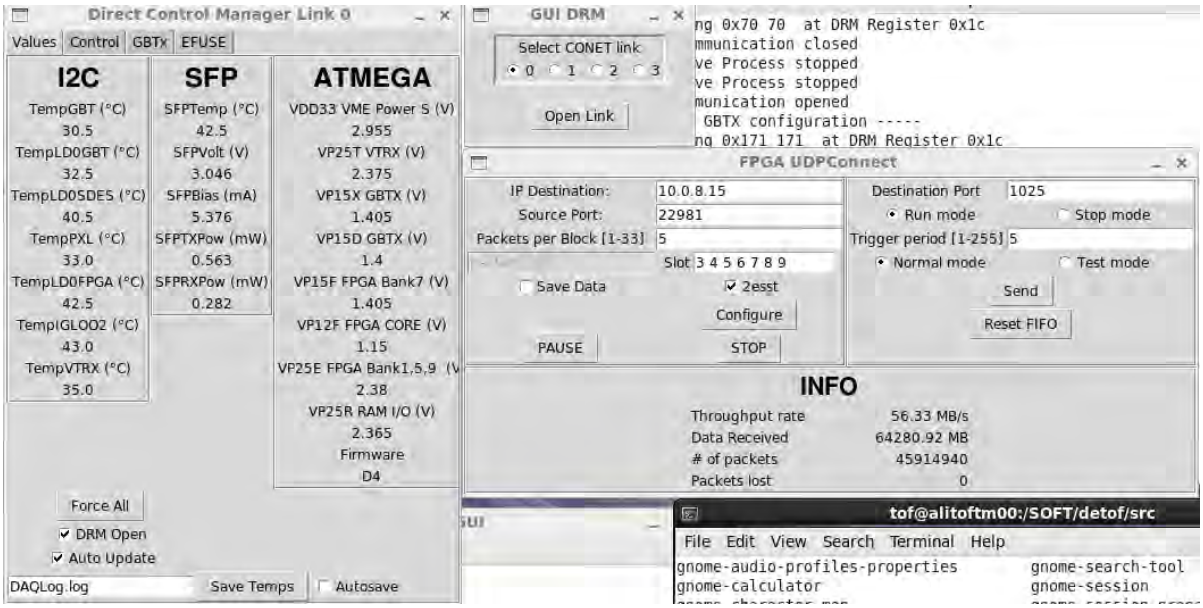

Figure 4.12: View of the GUI suite while used to monitor DRM2 and to acquire data from 7 TRMs.

So a single event is split up in multiple blocks and packets, whose data frame includes a small header containing information on the blocks and packets received.
Through these last values I implemented a kind of *handshaking* protocol between the KC705 and the DRM2 allowing the latter to send data only if the former acknowledges to have received the previous packet of the block. If this does not happen, the information about the packets lost per block are written on a lost-packet file that will be

[6] After this value we started to lose packets, while up to this number we tested the acquisition of ≈ 100 GB without data loss.

generated by default at the beginning of the receiving operation, and the acquisition will continue automatically only after this process, showing the loss of packets also on the specific label in Fig. 4.11.
Obtained UDP data can be saved for further analysis through the tick of a CheckBox on a custom named file. Moreover the VME64 2esst protocol can also be enabled via a dedicated CheckBox.
Ultimate tests with the software proved no data loss during the acquisition from one or more TRM boards and the saved data, analysed thanks to other custom C software (described in detail in sec. 4.3.1), were received correctly by the server with no errors.
These tests were also performed while monitoring the DRM2 via Direct Control Manager (Fig. 4.12).

4.3.1 *depack* and *rdchck*

In order to test the integrity of the obtained UDP data from the DRM2 two C software were used.
The first one is *depack* whose task is to reconstruct the events from the file obtained through UDPConnect. The program reads the file, finds the events and encodes them using the same data format that would be used by the CRU board, hence with 8192 kB packets (Fig. 4.13a).
Its primary function is to rebuild whole events, that can be distributed across multiple UDP packets with 1400 bytes length.
Then *rdchck* reads these data and applies a collection of check controls on the data integrity, showing in the end the number of events found, if there are writing errors compared to the default CRU data format (that for example implements 0xEEEEEEEE for all non-written data) and calculates the Cyclic Redundancy Check (CRC) for the events comparing them to the one calculated by the DRM2. The latter, above all, is really important because it allows checking whether data obtained from the board were not corrupted during data transmission. (Fig. 4.13b).
The applications checks also if the bunch ID sent from the CRU or from KC705 when the event was triggered is the same as the one written by the DRM2 and by TRMs.
It is compatible with 10 TRM boards and shows if there are errors on the words number, global header or trailer of the events.
These last two programs were widely used for data checking and to test the goodness of the ones we obtained through my software. They are currently implemented as terminal program, but in the future they could be fully integrated into the GUI suite I developed.

```
------ Encoded so far: 913000 events (96 words pending stored, 4 words expected)
------ READ SO FAR 365171861 BYTES (260837 blocks) [1400 bytes]: Bl # 43473 Pck. 4
------ Encoded so far: 923000 events (68 words pending stored, 28 words expected)
------ READ SO FAR 366361861 BYTES (261687 blocks) [1400 bytes]: Bl # 43615 Pck. 2
------ Encoded so far: 926000 events (4 words pending stored, 0 words expected)
------ READ SO FAR 367952261 BYTES (262823 blocks) [1400 bytes]: Bl # 43804 Pck. 4
------ Encoded so far: 930000 events (80 words pending stored, 20 words expected)
------ READ SO FAR 368349861 BYTES (263107 blocks) [1400 bytes]: Bl # 43852 Pck. 0
------ Encoded so far: 931000 events (72 words pending stored, 28 words expected)
------ READ SO FAR 369152061 BYTES (263680 blocks) [1400 bytes]: Bl # 43947 Pck. 3
------ Encoded so far: 933000 events (92 words pending stored, 8 words expected)
------ READ SO FAR 369552461 BYTES (263966 blocks) [1400 bytes]: Bl # 43995 Pck. 1
------ Encoded so far: 934000 events (32 words pending stored, 68 words expected)
------ READ SO FAR 369951461 BYTES (264251 blocks) [1400 bytes]: Bl # 44042 Pck. 4
------ Encoded so far: 935000 events (72 words pending stored, 28 words expected)
------ READ SO FAR 370752261 BYTES (264823 blocks) [1400 bytes]: Bl # 44138 Pck. 0
------ Encoded so far: 937000 events (88 words pending stored, 12 words expected)
------ READ SO FAR 372738861 BYTES (266242 blocks) [1400 bytes]: Bl # 44374 Pck. 3
------ Encoded so far: 942000 events (96 words pending stored, 4 words expected)
------ READ SO FAR 373135061 BYTES (266525 blocks) [1400 bytes]: Bl # 44421 Pck. 4
------ Encoded so far: 943000 events (4 words pending stored, 0 words expected)
```

(a)

```
-------------------------------------------------------------------------------------------------
ALICE-TOF data scan:    262144 events read (-2147483616 bytes)
Padding pattern err:    262144
DRM CRC event errors:   000000
CRU-DRM BC misalign.:   000000
-------------------------------------------------------------------------------------------------
TRM Data Scan             03     04     05     06     07     08     09     10     11     12
-------------------------------------------------------------------------------------------------
Events Ok               000000 000000 131072 000000 000000 000000 000000 000000 131072 000000
Word Count errors       000000 000000 000000 000000 000000 000000 000000 000000 000000 000000
Missing global header   000000 000000 000000 000000 000000 000000 000000 000000 000000 000000
Missing chain A header  000000 000000 000000 000000 000000 000000 000000 000000 000000 000000
Missing chain A trailer 000000 000000 000000 000000 000000 000000 000000 000000 000000 000000
Missing chain B header  000000 000000 000000 000000 000000 000000 000000 000000 000000 000000
Missing chain B trailer 000000 000000 000000 000000 000000 000000 000000 000000 000000 000000
Missing global trailer  000000 000000 000000 000000 000000 000000 000000 000000 000000 000000

Bunch Cnt misalignments 000000 000000 262144 000000 000000 000000 000000 000000 262144 000000
Event Cnt misalignments 000000 000000 000000 000000 000000 000000 000000 000000 131040 000000
CRC errors              000000 000000 000000 000000 000000 000000 000000 000000 000000 000000

IntraTRM event misal.   000000
IntraTRM BCID misal.    000000
-------------------------------------------------------------------------------------------------
```

(b)

Figure 4.13: (a) Messages of *depack* while encoding the file. (b) Final results of the *rdchck* application.

Chapter 5

Radiation tolerance test

Before the production phase of the boards, an important part of my thesis project was to test two key components of the DRM2: two kinds of AVAGO optical transceivers (AFBR-57R5AEZ and AFBR-57R5APZ) and the IGLOO2 FPGA (M2GL090T-1FGG676I with the latest silicon revision 3) [59].
The radiation levels at large experiments of the LHC can damage the electronics due to Total Ionizing Dose (TID) compromising its correct functioning.
The LHC heavy-ion collisions create, given the distance of 4 m from the interaction point, a moderately hostile environment for the DRM2, with a total dose of 0.13 krads in 10 years and a flux of 0.26 kHz/cm^2 of hadrons with energy above 20 MeV, which can cause single event upsets (SEU) and single event latchup (SEL) [60].
These effects happen when there is a very high energy deposition in a small volume of electronics chips, thus the released charge along the path of the ionizing particle is collected and the resulting transient current can cause, in the former, the bit flip from 0 to 1 or viceversa and, in the latter, the temporary inversion of a pn junction, resulting in the potential loss of vital detector control functions [61].
A localized energy deposition due to ionization depends both on the energy loss $\mathrm{d}E/\mathrm{d}x$ of heavy-ions (contribution $\propto Z^2$ and increasing rapidly with the decreasing energy of the particles) and on nuclear recoils, which rarely exceed 10 MeV and, hence, they have to be produced in the electronics chip to induce a SEU (their range is usually O(10) μm). Simulations, which applied first principles of the nuclear interactions of hadrons in silicon combined with the finding that high-energy hadrons dominate the SEU rate at LHC, demonstrated that a suitable test beam to study the radiation environment at LHC is a 60-200 MeV proton one, given that the SEU cross section is roughly energy-independent above 30 MeV [61].
For the sake of our tests we used the 100 MeV proton beam of the TIFPA facility at Trento Proton Therapy Centre with variable section and current. We irradiated two types of optical transceiver in order to choose which one was the best suited for the task, 4 for each kind and each one with a different dose, and three DRM2 boards mounting each an IGLOO2 FPGA. We analysed the SEU and SEL obtained and tested also if the FPGA were reprogrammable or not after the irradiation, as reported by some other

groups [62, 63].

5.1 Proton beam in Trento

The Trento Proton Therapy Center is one of the three facility in Italy treating tumors through the use of protons and it has been operative, both for patients treatment and research purposes, since mid 2014 [64].

Figure 5.1: Proton therapy delivery system for cancer treatment in Trento facility.

The facility was built by IBA (Ion Beam Applications), which is the world's leading provider of Proton Therapy solutions for the treatment of cancer, and it is now regulated by an agreement between TIFPA (INFN Trento Institute for Fundamentals Physics Applications) and APSS (Azienda Provinciale per i Servizi Sanitari).
It consists in a cyclotron able to produce protons up to 250 MeV, an energy selection system to continuously decrease the beam energy down to 70 MeV and a beam transport line that feeds two treatment rooms (Fig. 5.1) and one experimental area [65], shown in Fig. 5.2, which was completed only in 2016 and it is dedicated to a large spectrum of research activities.
The experimental area hosts a beam line split in two exit lines at 0°, used for biology research, and 30°, used for physics experiments. Through the latter, which is the one we used for our tests (Fig. 5.3), a single pencil beam is available.

5.2 Setup and tests performed

Our tests were performed using as basis the setup described in Ch. 3 (Fig. 5.5). The main differences are:

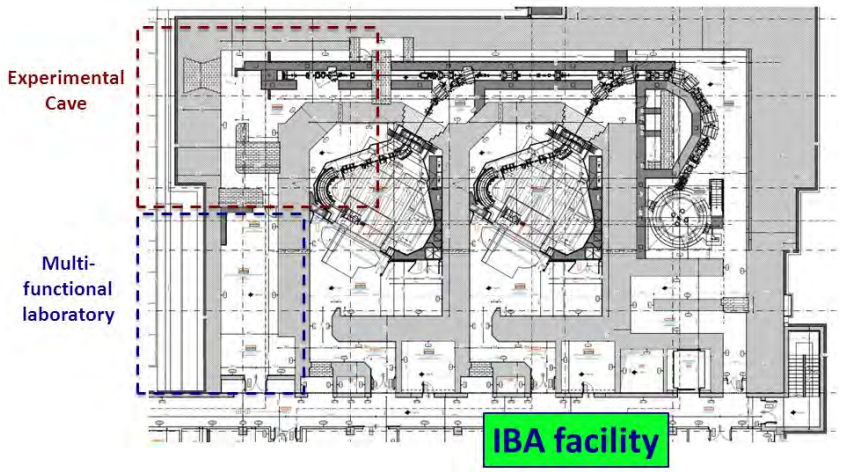

Figure 5.2: Schematic layout of the proton therapy center in Trento with the experimental area highlighted [66].

- the TRM board was not installed on the VME backplane, given that we needed to study only some components of the DRM2 board under radiation;

- a Windows computer was used, besides the Linux server, to monitor important current and voltage values of the DRM2 board and to switch off remotely the power supply (all of them performed thanks to Labview custom software) while the board was being irradiated (Fig. 5.4);

- an Arduino Nano based dongle connected to the DRM2 (Fig. 5.6a) was used to send monitoring voltages data to the PC through USB cable;

- a USB-8451 National Instruments serial I^2C master interface device was connected to retrieve temperatures and currents from the DRM2.

The backplane was positioned on a movable table, allowing us to target the beam to the center of the FPGA and, approximately, to the center of the optical transceiver. This was also possible thanks to a laser system installed in the experimental room and a self-levelling laser (Fig. 5.6b).

Figure 5.3: Picture of the experimental area beam split lines showing on the right the Physics one and on the left the Biology one.

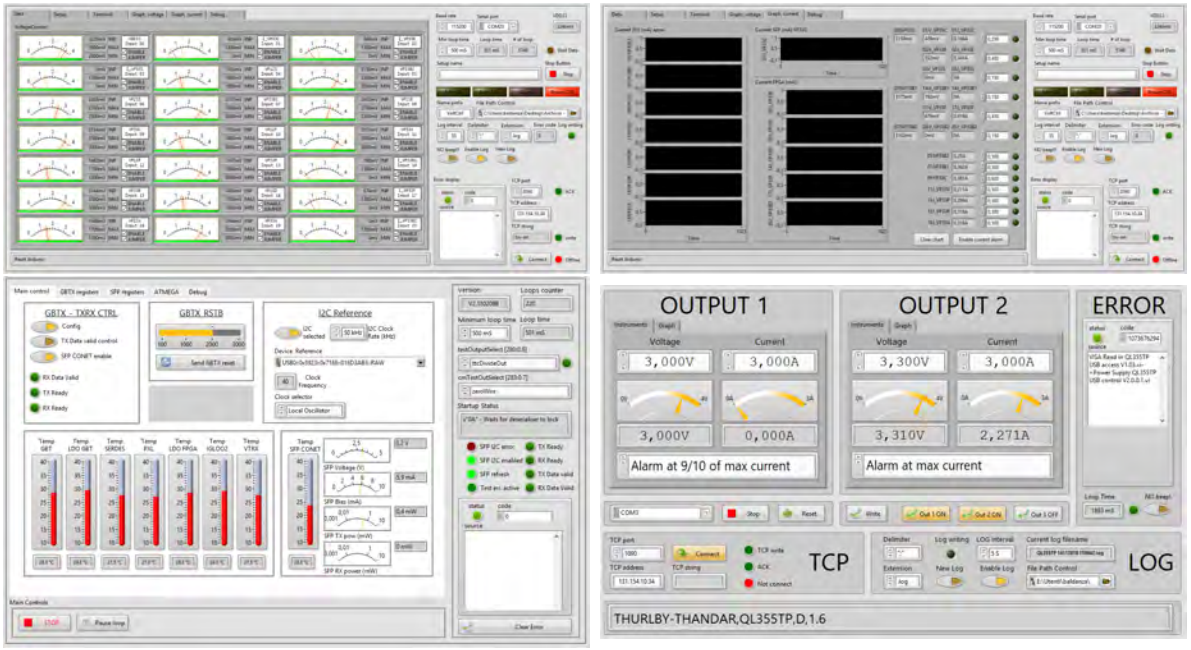

Figure 5.4: Labview software to monitor voltage, current and temperature values and to control and monitor the power supply.

While the beam was On we connected remotely to the Linux server through an SSH protocol connection and to the PC thanks to the commercial software TeamViewer.
In order to analyse the beam characteristics before the irradiation and to check whether or not it satisfied our needs a miniQ-STRIP detector (Fig. 5.7a), provided by the facility,

Figure 5.5: Setup under test.

was used [67]. This is a stack of ionization strip chambers that allows evaluating the beam spot center of gravity and the 2D profile at the isocenter.
Moreover the beam profile was evaluated thanks to Gafchromic films (a kind of radiation sensitive film) by measuring with a ruler the darkened area caused by the proton beam (Fig. 5.7b).

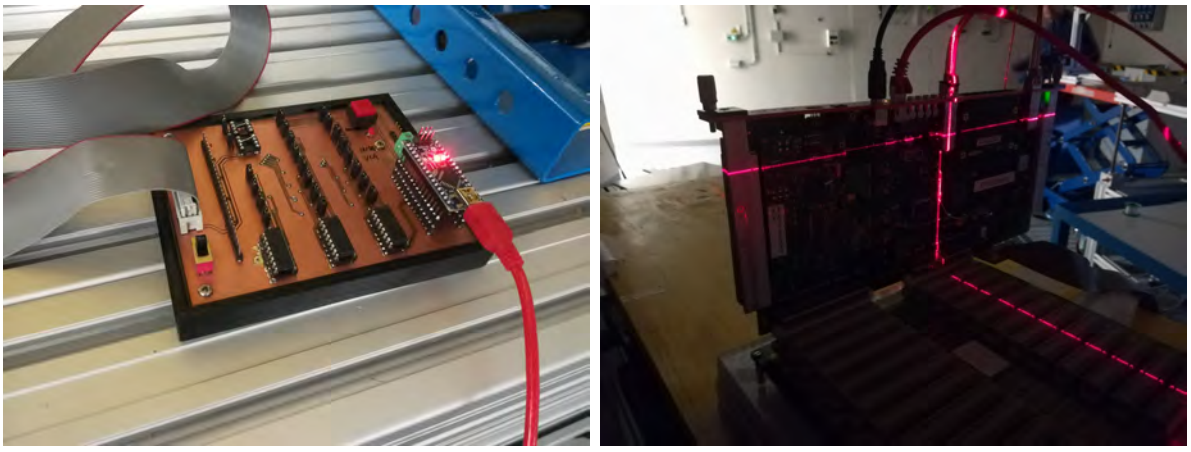

(a) (b)

Figure 5.6: (a) Arduino based dongle sending data to the Windows PC through USB; (b) Laser system used for targeting the beam to the components under test.

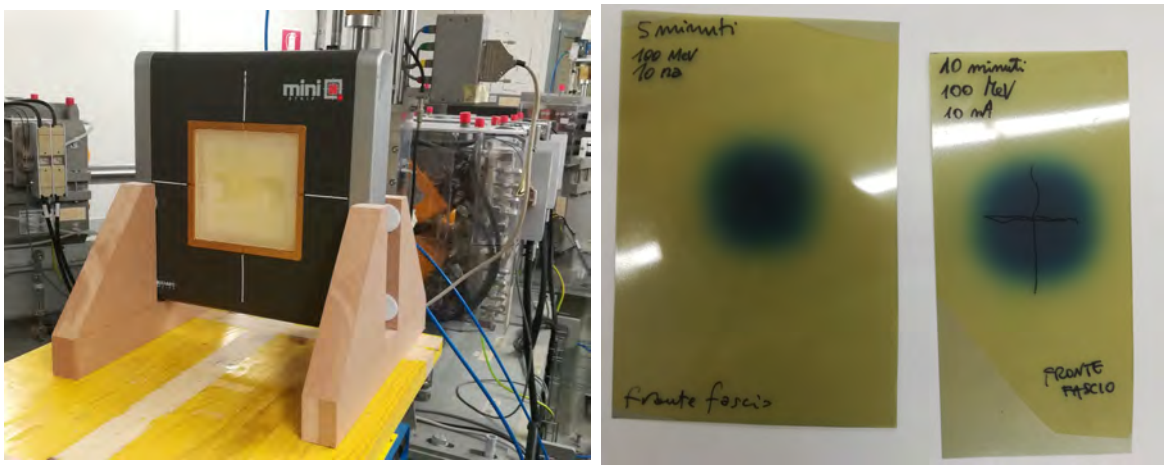

(a) (b)

Figure 5.7: Intruments used to analyse the proton beam: (a) miniQ-STRIP detector and (b) Gafchromic films irradiated by a 100 MeV 1 nA beam for 5 minutes (Left) and 10 minutes (right).

The beam was setup to deliver protons with a kinetic energy of 100 MeV and variable currents, corresponding to different proton fluxes on the device under test (DUT).

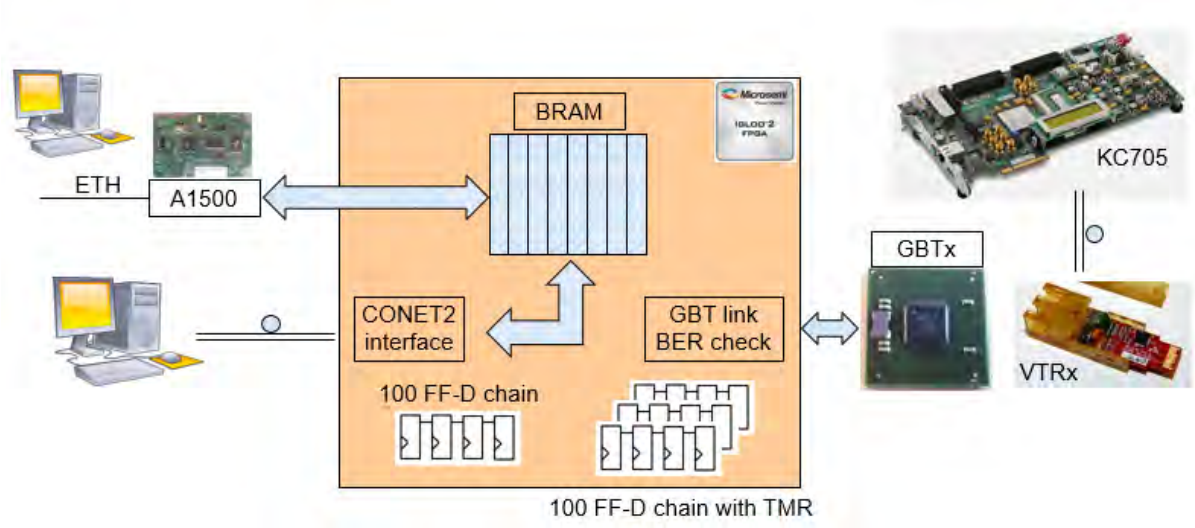

Figure 5.8: IGLOO2 firmware blocks implemented and basic connections to the Linux server for our setup.

For the purpose of our test, the firmware of the IGLOO2, during its irradiation, was edited implementing some special features, shown in Fig. 5.8, such an internal BRAM (64 KWords of 16 bit), which is written with known patterns[1] and then readout via

[1]These were 0xAAAA, 0x5555, 0x0000 and 0xFFFF to cover the situations of alternate bits and all bits set, and to better study if there are correlations or differences between $0 \rightarrow 1$ and $1 \rightarrow 0$ transitions.

CONET2 and A1500 (they use half of the memory each) in order to check upsets on the internal memory, and two D chains of 100 flip-flops running at 40 MHz, one of them with Triple Modular Redundancy implemented (TMR), loaded with a known pattern and analysed to test internal logic upsets. Moreover we analysed also the GBTx link, thanks to the KC705 evaluation board.
So our purpose was to estimate the SEU and SEL rates, to evaluate the reprogramming ability of the board after irradiation and to analyse the stability of the used links. To do so we put the DRM2 board under a state of running data transmission over the GBTx link and analysed the returned values of the BRAM registers and of the pattern inside the flip-flops loop, which are both sensible to SEU. Comparing these with the true values using a Linux software we obtained the bit upsets rate. In the meantime the FPGA transmitted data on the GBTx link and these were tested via KC705 (data sent in a loopback to the FPGA and checked against the expected values).
The SEL were analysed by monitoring current values of the board, given that a latchup implies a higher electric absorption due to a junction becoming conductive, so if some values have a rise we could intervene by powercycle bringing the card back to normal conditions.

5.3 Results

Data transfer from BRAM was implemented both from the CONET2 link and from the PXL data bus (which is the way the ARM processor on the A1500 mezzanine interfaces the FPGA [46]).

```
18/Apr/2018 22:20:17 --I-- beam on
18/Apr/2018 22:20:19 --I-- completed monitoring cycle # 100 [Err Count: BER 0 SREG 0 SREG(TMR) 0 BRAM 1]
18/Apr/2018 22:20:20 --E-- BRAM found 0xFFBF instead of 0xFFFF at address 0x10D0A09A
18/Apr/2018 22:20:23 --I-- completed monitoring cycle # 110 [Err Count: BER 0 SREG 0 SREG(TMR) 0 BRAM 2]
18/Apr/2018 22:20:26 --E-- BRAM found 0xFFFD instead of 0xFFFF at address 0x10D0BC2E
18/Apr/2018 22:20:27 --E-- BRAM found 0x5455 instead of 0x5555 at address 0x10D09BC9
18/Apr/2018 22:20:27 --E-- BRAM found 0xAAAB instead of 0xAAAA at address 0x10D0C658
18/Apr/2018 22:20:28 --I-- completed monitoring cycle # 120 [Err Count: BER 0 SREG 0 SREG(TMR) 0 BRAM 5]
18/Apr/2018 22:20:31 --E-- BRAM found 0x5545 instead of 0x5555 at address 0x10D09255
18/Apr/2018 22:20:32 --I-- completed monitoring cycle # 130 [Err Count: BER 0 SREG 0 SREG(TMR) 0 BRAM 6]
18/Apr/2018 22:20:34 --E-- BRAM found 0xBAAA instead of 0xAAAA at address 0x10D09998
18/Apr/2018 22:20:36 --E-- BRAM found 0xBFFF instead of 0xFFFF at address 0x10D0DCC6
18/Apr/2018 22:20:37 --I-- completed monitoring cycle # 140 [Err Count: BER 0 SREG 0 SREG(TMR) 0 BRAM 8]
```

Figure 5.9: Excerpt from the Log file of the PROTO0 CONET2 RUN1 irradiation.

The data taking took from 16 to 18 April 2018, since we could use the proton beam just for few hours in the evening (due to the patient treatment schedule), allowing the irradiation of 8 AVAGO optical transceivers (4 EZ and 4 PZ), and 3 IGLOO2 FPGA mounted on different DRM2 boards.
The monitoring of internal registers of the SFP[2] via I^2C bus was also performed while irradiating all the components.

[2]Small Form-factor Pluggable refers to the optical transceiver.

The analysis of the obtained data was done offline using a custom made software written in Python, which analysed all the Log files obtained while the beam was ON and the simulation running.
SEUs are indicated for example in the lines of the log extract shown in Fig. 5.9 where single bit upsets were found at different locations, like 0xFFBF instead of 0xFFFF at the address 0x10D0A09A, meaning 1111 (F) changed to 1011 (B), or 0xAAAB instead of 0xAAAA, so 1010 (A) → 1011 (B), at address 0x10D0C658.
Furthermore some counters keep track of all the obtained errors (BER, for GBTx errors, SREG and SREG(TMR), for flip-flops, and BRAM).

5.3.1 AVAGO

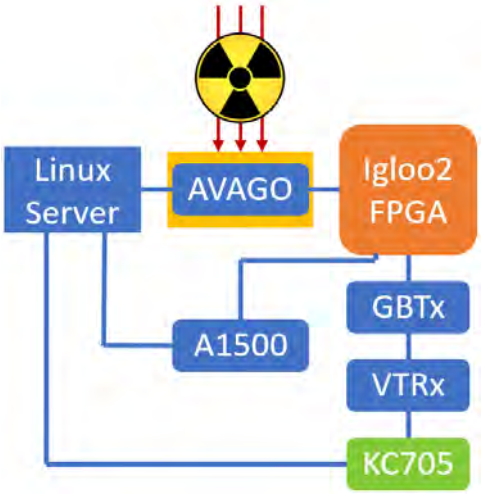

Figure 5.10: Phase 1: AVAGO irradiation.

The optical transceivers were the first components we analysed under radiation.
For all of them the beam was setup with a current of 10 nA and a flux of 1.04×10^8 p/s. Thus, in order to test them with different radiation doses, they were irradiated for different time intervals, shown in Tab. 5.1.
The absorbed dose D was obtained with the formula:

$$D = \frac{\text{Fluence}}{\text{Fluence}_{\text{ref}}} D_{\text{ref}} \tag{5.1}$$

where the fluence is calculated by multiplying the flux with the duration of the irradiation and *ref* means reference values, which for silicon and a 100 MeV proton beam are:

$$\text{Fluence}_{\text{ref}} = 10^{11}\,\text{p} \quad D_{\text{ref}} = 9.40\,\text{krad}. \tag{5.2}$$

The analysis showed no errors for all of the devices except for the EZ4 which returned one error in the BRAM both for CONET2 and PXL (A1500). These were received almost

45 seconds apart: the former returned 0xCACC instead of 0xAAAA at the address 0x10D01FFC, while the latter returned 0xFFFF instead of 0x0 at address 0x10D0EB3B. However they were reported about a minute before the "beam ON" declaration in the logs, so they should be discarded, as they were probably caused by non-reproducible noise conditions during beam setup.

Device (EZ and PZ)	Duration (s)	Dose (krad)
1	300	2.93
2	300	2.93
3	450	4.40
4	600	5.87

Table 5.1: AVAGO EZ and PZ optical transceivers irradiation parameters.

We found no transmission errors and both the AVAGO models tested resulted stable and reliable, showing neither TID damages, nor SEU and SEL. Moreover the monitoring of SFP registers showed no communication errors.
In the end the EZ model was chosen for the TOF detector because it has a better shielding with respect to electromagnetic noise (from datasheet).

5.3.2 FPGA

The FPGAs irradiated were mounted on three different boards: PROTO0, PROTO2 and PROTO3.

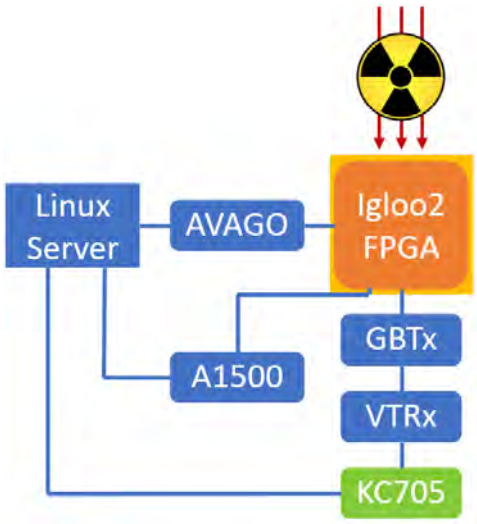

Figure 5.11: Phase 2: FPGA irradiation.

They were tested using different beam currents and for different time intervals so to achieve different absorbed doses for the silicon die of the IGLOO2, which is 1×1 cm^2 inside a 2.5×2.5 cm^2 package.

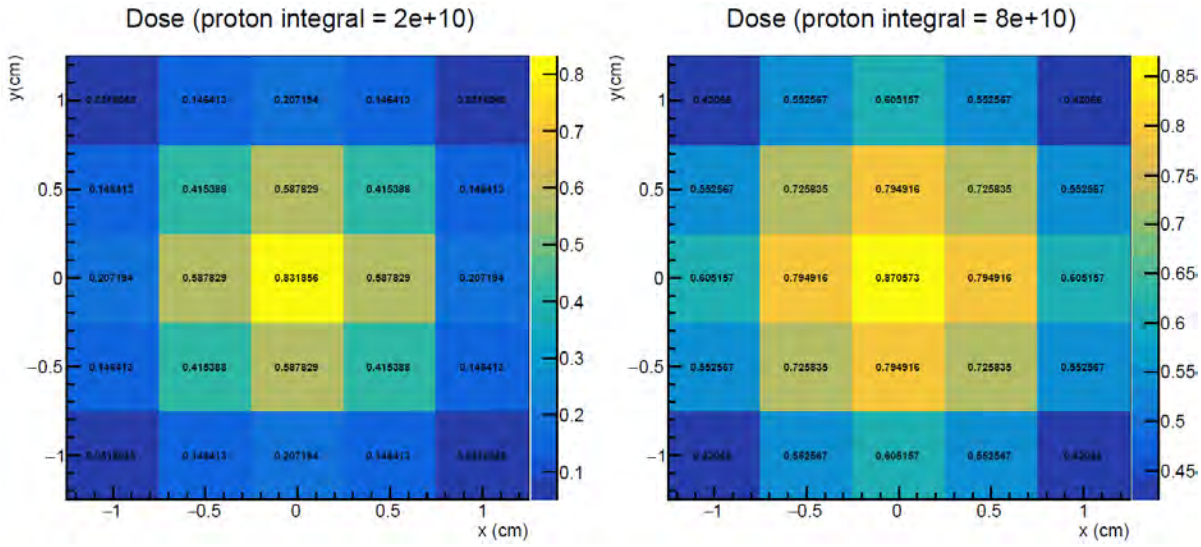

(a)

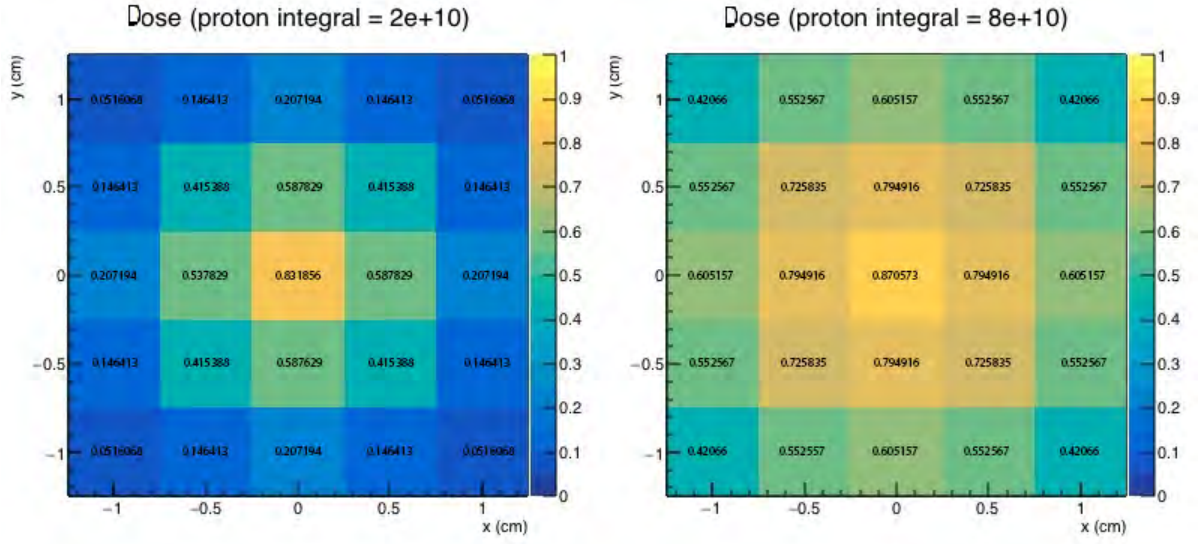

(b)

Figure 5.12: Estimate of the package dose absorptions with two beam integral values and with beam sigmas of (a) 0.58 cm and (b) 1.12 cm.

The dose values shown in the following tables are averaged over the FPGA package, while a more precise study of it was computed and can be seen in Fig. 5.12. Here the beam was described as a bi-dimensional Gaussian with a sigma of 0.58 cm (Fig. 5.12a) and 1.12 cm (Fig. 5.12b), the silicon die was divided in square sections, the number of protons was calculated by integrating the beam, from which the fluence was obtained, and the average dose of each square was calculated through Eq. 5.1 using as reference values those in Eq. 5.2.
For the PROTO0 a beam sigma of 0.58 cm was setup, while for the other two boards we

used a sigma of 1.12 cm, hence giving the silicon die a more uniform dose.
The last rows of the dose tables show the total average dose in bold.
Each error was given by a single bit changing state, i.e. no multiple bits upset was found.
After each RUN we also tested the reprogramming ability of the boards under test.
In the tables shown in the next paragraphs: SFP_{tot} refers to total I^2C errors of the SFP and $0 \rightarrow 1$ and $1 \rightarrow 0$ are all the bit flips from 0 to 1 and viceversa obtained in the BRAM, whose sum is indicated as $BRAM_{tot}$.
Furthermore neither the CONET2 nor the GBTx link went down, we saw just one SEU on flip-flops during RUN1 of PROTO3 board, and no SEL were found during all the irradiation tests, as opposed to the latchup events found during a previous irradiation campaign in 2016, where several other components (like SSRAM, clock and voltage regulators), two different models of Finisar optical transceiver and the IGLOO2 with silicon revision 1 were tested. These events are shown as current rise in Fig. 5.13 after which the board was powercycled to solve them.

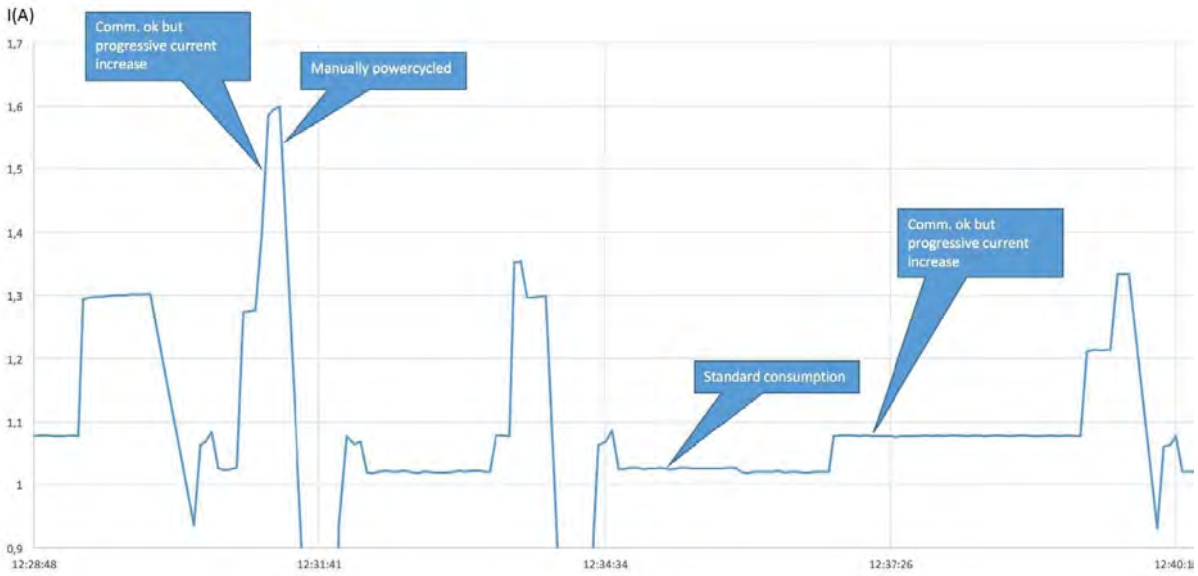

Figure 5.13: Total current absorbed by the tested board as a function vs time during irradiation tests in 2016.

PROTO0

Initially we tried to use a very low intensity flux, given the SEU rate was unknown, but the facility is not able to measure current values smaller than 1 nA. In this situation the intensity is firstly measured with a scintillator system, that provides an intercalibration and a measurement of the obtained flux. This operation was performed by TIFPA personnel.
The SFP error 0xA2 obtained refers to an error on I^2C data (it does not compromise the

connection to the board) and it seems related, therefore, to some upset in the registers controlling the I^2C bus in the FPGA (the SFP was not irradiated).

RUN	**Current (nA)**	**Flux (p/s)**	**Duration (s)**	**Dose (krad)**	**Dose rate (krad/s)**
1	n.a.	2.9e06	1800	0.18	0.10
2	1	8.9e06	450	0.14	0.31
3	1	8.7e06	600	0.18	0.30
4	2	2.2e07	300	0.23	0.77
5	2	2.0e07	720	0.5	0.69
				1.24	

Table 5.2: PROTO0 irradiation parameters.

RUN	**$BRAM_{tot}$**	**SFP_{tot}**	**0→1**	**1→0**
1	10	0	5	5
2	6	0	2	4
3	10	0	4	6
4	6	0	5	1
5	20	0	15	20

Table 5.3: PROTO0 errors monitored via CONET2.

RUN	**$BRAM_{tot}$**	**SFP_{tot}**	**0→1**	**1→0**
1	13	1 (0xA2)	6	7
2	10	0	5	5
3	10	0	7	3
4	9	2 (0xA2)	1	8
5	35	1 (0xA2)	15	20

Table 5.4: PROTO0 errors monitored via PXL.

PROTO3

This board showed no SFP I^2C errors and the connection to it was stable during all the radiation tests.

RUN	**Current (nA)**	**Flux (p/s)**	**Duration (s)**	**Dose (krad)**	**Dose rate (krad/s)**
1	10	9.3e07	461	0.48	1.04
2	10	9.5e07	450	0.48	1.07
3	10	9.5e07	450	0.48	1.07
4	10	9.5e07	450	0.48	1.07
5	10	9.5e07	450	0.48	1.07
				2.54	

Table 5.5: PROTO3 irradiation parameters.

RUN	**$BRAM_{tot}$**	**SFP_{tot}**	**0→1**	**1→0**
1	30	0	14	16
2	27	0	15	12
3	54	0	20	34
4	63	0	32	31
5	59	0	31	28

Table 5.6: PROTO3 errors monitored via CONET2.

RUN	**$BRAM_{tot}$**	**SFP_{tot}**	**0→1**	**1→0**
1	28	0	13	15
2	22	0	5	17
3	60	0	31	29
4	45	0	23	22
5	51	0	24	27

Table 5.7: PROTO3 errors monitored via PXL.

PROTO2

This was the last tested board and we tried to reach a larger total dose. Hence a higher dose rate was also used (given the short remaining beam time allocated to us).
During RUN2 the CONET2 link crashed after 3 minutes of irradiation due to a user error (the program monitoring the CONET2 link was shutdown inadvertently), so 24 seconds of data were lost for the PXL, while the CONET2 remained down. Once the program was restarted the initialization of the BRAM was redone (this is why Tab. 5.10 shows a

sum of two values for this irradiation).
After being irradiated with 3.82 krad, it was not possible to reprogram the board at first, but after ≈ 12 hours we tried again and it reprogrammed successfully.
As reported also by some other groups, it seems a certain annealing time is needed to recover the reprogramming ability, at least for these values of TID (above 10 krad - a value not relevant for TOF - it has been reported that reprogrammability is permanently lost) [62, 63].
For this card we observed I^2C interface errors of the I^2C interface towards the SFP just during RUN1. However this instability was observed before while testing the card in a standard environment and it is likely due to some mounting issues of the card components.
For this reason we preferred not to powercycle the board or just the SFP to re-establish this communication, given that it was more important to monitor the BRAM.

RUN	**Current (nA)**	**Flux (p/s)**	**Duration (s)**	**Dose (krad)**	**Dose rate (krad/s)**
1	20	1.9e08	600	1.27	2.12
2	20	1.9e08	600	1.27	2.12
3	20	1.9e08	600	1.27	2.12
				3.82	

Table 5.8: PROTO2 irradiation parameters.

RUN	**$BRAM_{tot}$**	**SFP_{tot}**	**0→1**	**1→0**
1	146	0	77	69
2	41(crash)	0	17	24
3	156	0	71	85

Table 5.9: PROTO2 errors monitored via CONET2.

RUN	**$BRAM_{tot}$**	**SFP_{tot}**	**0→1**	**1→0**
1	161	>800	70	91
2	76+76=152	0	39+37=76	37+39=76
3	145	0	72	73

Table 5.10: PROTO2 errors monitored via PXL.

5.4 SEU cross-section for BRAM

The cross sections of the BRAM bits were calculated for all the IGLOO2 via Eq.

$$\sigma_{\text{bit}} = \frac{\text{BRAM}_{\text{tot}}}{\text{Nbit}_{\text{tot}} \cdot \text{Fluence}}, \tag{5.3}$$

where Nbit_{tot} is the total number of bits inside the BRAM (64 KWords×16 bits = 1048576 bits) and BRAM_{tot} is the number of total SEU obtained, as in previous tables. Results of these measurements can be seen in Tab. 5.11, where the last row shows the mean obtained value and the errors on them were calculated through:

$$\delta\sigma_{\text{bit}} = \sigma_{\text{bit}} \sqrt{\left(\frac{\delta\text{BRAM}_{\text{tot}}}{\text{BRAM}_{\text{tot}}}\right)^2 + \left(\frac{\delta\text{Fluence}}{\text{Fluence}}\right)^2}, \tag{5.4}$$

where a statistical error equal to the square root of the total SEU number and systematic uncertainty of the 15% for respectively the BRAM_{tot} and Fluence values have been considered.
We did not calculate on purpose the cross section of PROTO2 during RUN2, due to lack of data caused by the user error described earlier.

RUN	**PROTO0**	**PROTO3**	**PROTO2**
1	(1.1±0.3)e-14	(1.1±0.2)e-14	(2.2±0.3)e-14
2	(1.0±0.3)e-14	(9.2±1.9)e-15	n.a.
3	(9.8±2.6)e-15	(2.1±0.4)e-14	(2.1±0.3)e-14
4	(5.8±1.7)e-15	(2.0±0.4)e-14	
5	(9.8±2.0)e-15	(2.1±0.4)e-14	
Mean	**(9.3±2.5)e-15**	**(1.7±0.3)e-14**	**(2.2±0.3)e-14**

Table 5.11: BRAM bit cross sections in $\frac{1}{\text{cm}^2\text{bit}}$ units.

The obtained cross section values, whose average for the three analysed FPGA is $\overline{\sigma}_{\text{bit}} = (1.6 \pm 0.3) \cdot 10^{-14}$ $\text{cm}^{-2}\text{bit}^{-1}$, are compatible to those obtained in previous irradiation measurements by other groups [68].
We saw no significant differences between bits transition from $0 \rightarrow 1$ or viceversa, no multiple upsets were found and no latchup events were observed.
Moreover we did not lose the CONET2 link for all the irradiation tests, hence its implementation seems reliable inside a moderately hostile radiation environment.
However, as discussed before, the beam conditions were different for PROTO0 with respect to PROTO3 and PROTO2 (the two latter measurements are compatible within two sigmas) during whose tests the die surface was irradiated in a more homogenous way. We report therefore as final value the average of just PROTO3 and PROTO2 irradiation as $(2.0 \pm 0.3) \cdot 10^{-14}$ $\text{cm}^{-2}\text{bit}^{-1}$.

Conclusions

In this thesis I presented the software I developed to test the DRM2 board, a new readout card that will be used by the ALICE TOF detector at LHC.
This software was used to configure (including permanent configuration of GBTx chip) and monitor the card as well as to test the full data acquisition chain with a compact set of test boards. This entailed the development of a UDP-based data readout between my software and a commercial card to mimic the full DAQ chain that will be deployed in the experiment.
The radiation tests in Trento allowed us to choose the EZ AVAGO optical transceiver over the PZ, as the one that will be mounted on the 72 commissioned boards. Even though they both behaved correctly under the proton beam, the former was preferred because it has a better shielding with respect to electromagnetic noise.
The tests on the IGLOO2 allowed the verification that the silicon version 3 produced by Microsemi is SEL immune as stated by the manufacturer. We verified the stability of both the logic elements and of our code (in particular the one implementing the CONET2 link) when exposed to radiation and we observed no communication errors.
Moreover the BRAM SEU cross section measured is consistent with values reported by other groups.

Bibliography

[1] M. E. Peskin and D. V. Schroeder, *An Introduction to quantum field theory*. Reading, USA: Addison-Wesley, (1995), ISBN: 9780201503975.

[2] O. W. Greenberg, "Spin and Unitary-Spin Independence in a Paraquark Model of Baryons and Mesons", *Phys. Rev. Lett.*, vol. 13, pp. 598–602, 20 (1964). DOI: 10.1103/PhysRevLett.13.598.

[3] F. Halzen and A. D. Martin, *Quarks and Leptons: An introductory course in modern particle physics*. New York, Usa: Wiley, (1984).

[4] I. Aitchison and A. Hey, *Gauge Theories in Particle Physics: QCD and the Electroweak Theory, 3rd Edition, Vol 2*. Taylor & Francis, (2003), ISBN: 9780750309509.

[5] W. Nazarewicz, *QCD class*, Lesson at Michigan State University, 2015.

[6] T. Klijnsma, S. Bethke, G. Dissertori, *et al.*, "Determination of the strong coupling constant $\alpha_s(m_Z)$ from measurements of the total cross section for top-antitop quark production", *Eur. Phys. J.*, vol. C77: 778, (2017). DOI: 10.1140/epjc/s10052-017-5340-5. arXiv: 1708.07495 [hep-ph].

[7] D. J. Gross and F. Wilczek, "Ultraviolet Behavior of Nonabelian Gauge Theories", *Phys. Rev. Lett.*, vol. 30, pp. 1343–1346, (1973). DOI: 10.1103/PhysRevLett.30.1343.

[8] H. Satz, "The Quark-Gluon Plasma – A Short Introduction", *Nuclear Physics A*, vol. 862-863, (2011), ISSN: 0375-9474. DOI: 10.1016/j.nuclphysa.2011.05.014.

[9] M. A. Stephanov, "QCD phase diagram: An Overview", *PoS*, vol. LAT2006, 024, (2006). DOI: 10.22323/1.032.0024. arXiv: hep-lat/0701002 [hep-lat].

[10] S. Sarkar, H. Satz, and B. Sinha, *The Physics of the Quark-Gluon Plasma: Introductory Lectures*, ser. Lecture Notes in Physics. Springer Berlin Heidelberg, (2009), ISBN: 9783642022852.

[11] A. Chodos, R. L. Jaffe, K. Johnson, *et al.*, "New extended model of hadrons", *Phys. Rev. D*, vol. 9, pp. 3471–3495, 12 Jun. 1974. DOI: 10.1103/PhysRevD.9.3471.

[12] C. Davies, "Lattice QCD: A Guide for people who want results", in *Proceedings, 58th Scottish Universities Summer School in physics, SUSSP58, St. Andrews, UK, August 22-28, 2004*, (2005), pp. 233–272. eprint: hep-lat/0509046.

[13] K. Fukushima and V. Skokov, "Polyakov loop modeling for hot QCD", *Prog. Part. Nucl. Phys.*, vol. 96, pp. 154–199, (2017). arXiv: 1705.00718 [hep-ph].

[14] F. Becattini, "The Quark Gluon Plasma and relativistic heavy ion collisions in the LHC era", *Journal of Physics: Conference Series*, vol. 527, no. 1, (2014).

[15] M. Tanabashi, K. Hagiwara, K. Hikasa, *et al.* Particle Data Group Collaboration, "Review of Particle Physics", *Phys. Rev. D*, vol. 98, 3, 030001 Aug. 2018. DOI: 10.1103/PhysRevD.98.030001.

[16] B. Abelev *et al.* ALICE Collaboration, "Centrality dependence of π, K, p production in Pb-Pb collisions at $\sqrt{s_{NN}}$ = 2.76 TeV", *Phys. Rev.*, vol. C88, p. 044910, (2013). DOI: 10.1103/PhysRevC.88.044910. arXiv: 1303.0737 [hep-ex].

[17] N. Armesto and E. Scomparin, "Heavy-ion collisions at the Large Hadron Collider: a review of the results from Run 1", *Eur. Phys. J. Plus*, vol. 131, no. 3, p. 52, (2016). DOI: 10.1140/epjp/i2016-16052-4. arXiv: 1511.02151 [nucl-ex].

[18] J. Rafelski and B. Müller, "Strangeness production in the quark-gluon plasma", *Phys. Rev. Lett.*, vol. 48, pp. 1066–1069, 16 Apr. 1982. DOI: 10.1103/PhysRevLett.48.1066.

[19] F. Antinori *et al.* NA57 Collaboration, "Enhancement of hyperon production at central rapidity in 158-A-GeV/c Pb-Pb collisions", *J. Phys.*, vol. G32, (2006). DOI: 10.1088/0954-3899/32/4/003. arXiv: nucl-ex/0601021 [nucl-ex].

[20] B. B. Abelev *et al.* ALICE Collaboration, "Multi-strange baryon production at mid-rapidity in Pb-Pb collisions at $\sqrt{s_{NN}}$ = 2.76 TeV", *Phys. Lett.*, vol. B728, (2014). arXiv: 1307.5543 [nucl-ex].

[21] G. Aad *et al.* ATLAS Collaboration, "Measurement of charged-particle spectra in Pb+Pb collisions at $\sqrt{s_{\mathrm{NN}}}$ = 2.76 TeV with the ATLAS detector at the LHC", *JHEP*, vol. 09, 050, (2015). DOI: 10.1007/JHEP09(2015)050. arXiv: 1504.04337 [hep-ex].

[22] B. Abelev *et al.* ALICE Collaboration, "Centrality dependence of charged particle production at large transverse momentum in Pb–Pb collisions at $\sqrt{s_{\mathrm{NN}}}$=2.76 TeV", *Physics Letters B*, vol. 720, no. 1, pp. 52–62, (2013), ISSN: 0370-2693. DOI: https://doi.org/10.1016/j.physletb.2013.01.051.

[23] T. Matsui and H. Satz, "J/ψ Suppression by Quark-Gluon Plasma Formation", *Phys. Lett.*, vol. B178, pp. 416–422, 1986. DOI: 10.1016/0370-2693(86)91404-8.

[24] R. Vogt, "Cold Nuclear Matter Effects on Open and Hidden Heavy Flavor Production at the LHC", in *Proceedings, 7th International Workshop on Charm Physics, CHARM 2015: Detroit, USA, May 18-22*, (2015). arXiv: 1508.01286 [hep-ph].

[25] C. Hadjidakis, "Quarkonium production in ALICE at the LHC", *Nuclear Physics A*, vol. 932, pp. 541–548, (2014). DOI: https://doi.org/10.1016/j.nuclphysa.2014.09.085. arXiv: 1405.1177 [hep-ex].

[26] G. Trombetta for the ALICE Collaboration, "New results on Initial State and Quarkonia with ALICE", in *5th Large Hadron Collider Physics Conference (LHCP 2017) Shanghai, China, May 15-20*, (2017). arXiv: 1709.04363 [nucl-ex].

[27] S. Chatrchyan *et al.* CMS Collaboration, "Observation and studies of jet quenching in PbPb collisions at nucleon-nucleon center-of-mass energy = 2.76 TeV", *Phys. Rev.*, vol. C84, (2011). DOI: 10.1103/PhysRevC.84.024906. arXiv: 1102.1957 [nucl-ex].

[28] J. Adam *et al.*, "Centrality dependence of high-p_T D meson suppression in Pb-Pb collisions at $\sqrt{s_{NN}} = 2.76$ TeV", *Journal of High Energy Physics*, vol. 2015, no. 11, p. 205, Nov. 2015, ISSN: 1029-8479. DOI: 10.1007/JHEP11(2015)205.

[29] B. B. Abelev *et al.* ALICE Collaboration, "Azimuthal anisotropy of D meson production in Pb-Pb collisions at $\sqrt{s_{\mathrm{NN}}} = 2.76$ TeV", *Phys. Rev.*, vol. C90, no. 3, p. 034904, (2014). DOI: 10.1103/PhysRevC.90.034904. arXiv: 1405.2001 [nucl-ex].

[30] B. Abelev *et al.* ALICE Collaboration, "Upgrade of the ALICE Experiment: Letter Of Intent", *J. Phys.*, vol. G41, 087001, (2014). DOI: 10.1088/0954-3899/41/8/087001.

[31] K. Aamodt *et al.* ALICE Collaboration, "The ALICE experiment at the CERN LHC", *Journal of Instrumentation*, vol. 3, no. 08, S08002, (2008).

[32] S. Acharya *et al.* ALICE Collaboration, "The ALICE Transition Radiation Detector: construction, operation, and performance", *Nucl. Instrum. Meth.*, vol. A881, pp. 88–127, (2018). DOI: 10.1016/j.nima.2017.09.028. arXiv: 1709.02743 [physics.ins-det].

[33] K. Aamodt *et al.* ALICE Collaboration, "Alignment of the ALICE Inner Tracking System with cosmic-ray tracks", *JINST*, vol. 5, P03003, (2010). DOI: 10.1088/1748-0221/5/03/P03003. arXiv: 1001.0502 [physics.ins-det].

[34] B. B. Abelev *et al.* ALICE Collaboration, "Performance of the ALICE Experiment at the CERN LHC", *Int. J. Mod. Phys.*, vol. A29, 1430044, (2014). DOI: 10.1142/S0217751X14300440. arXiv: 1402.4476 [nucl-ex].

[35] J. Alme, Y. Andres, H. Appelshäuser, *et al.*, "The ALICE TPC, a large 3-dimensional tracking device with fast readout for ultra-high multiplicity events", *Nuclear Instruments and Methods in Physics Research Section A: Accelerators, Spectrometers, Detectors and Associated Equipment*, vol. 622, no. 1, pp. 316–367, (2010), ISSN: 0168-9002. DOI: https://doi.org/10.1016/j.nima.2010.04.042.

[36] C. Grupen and B. Shwartz, *Particle Detectors*, 2nd ed., ser. Cambridge Monographs on Particle Physics, Nuclear Physics and Cosmology. Cambridge University Press, (2008). DOI: 10.1017/CBO9780511534966.

[37] A. Akindinov *et al.*, "Performance of the ALICE Time-Of-Flight detector at the LHC", *Eur. Phys. J. Plus*, vol. 128, 44, (2013). DOI: 10.1140/epjp/i2013-13044-x.

[38] N. Jacazio for the AchuLICE Collaboration, "PID performance of the ALICE-TOF detector in Run 2", in *6th Large Hadron Collider Physics Conference (LHCP 2018) Bologna, Italy, June 4-9*, 2018. arXiv: 1809.00574 [physics.ins-det].

[39] B. Abelev *et al.* ALICE Collaboration, "Technical design report for the Upgrade of the ALICE Time Projection Chamber", Tech. Rep. CERN-LHCC-2013-020. ALICE-TDR-016, Oct. 2013. [Online]. Available: https://cds.cern.ch/record/1622286.

[40] B. Abelev *et al.* ALICE Collaboration, "Technical Design Report for the Upgrade of the ALICE Inner Tracking System", Tech. Rep. CERN-LHCC-2013-024. ALICE-TDR-017, Nov. 2013. [Online]. Available: https://cds.cern.ch/record/1625842.

[41] P. Antonioli, A. Kluge, and W. Riegler ALICE Collaboration, "Upgrade of the ALICE Readout & Trigger System", Tech. Rep. CERN-LHCC-2013-019. ALICE-TDR-015, Sep. 2013. [Online]. Available: http://cds.cern.ch/record/1603472.

[42] P. Buncic, M. Krzewicki, and P. Vande Vyvre, "Technical Design Report for the Upgrade of the Online-Offline Computing System", Tech. Rep. CERN-LHCC-2015-006. ALICE-TDR-019, Apr. 2015. [Online]. Available: https://cds.cern.ch/record/2011297.

[43] J. Wiechula for the ALICE Collaboration, "The upgrade program of ALICE at the LHC", (2018), LHCP 2018 Presentation. [Online]. Available: https://indico.cern.ch/event/681549/contributions/2944434/attachments/1664823/2668433/180609_LHCP_ALICE_upgrade.pdf.

[44] F. Sauli, "The gas electron multiplier (GEM): Operating principles and applications", *Nuclear Instruments and Methods in Physics Research Section A: Accelerators, Spectrometers, Detectors and Associated Equipment*, vol. 805, pp. 2–24, (2016), ISSN: 0168-9002. DOI: https://doi.org/10.1016/j.nima.2015.07.060.

[45] D. González-Díaz, F. Monrabal, and S. Murphy, "Gaseous and dual-phase time projection chambers for imaging rare processes", *Nuclear Instruments and Methods in Physics Research Section A: Accelerators, Spectrometers, Detectors and Associated Equipment*, vol. 878, pp. 200–255, (2018), ISSN: 0168-9002. DOI: https://doi.org/10.1016/j.nima.2017.09.024.

[46] D. Falchieri, P. Antonioli, C. Baldanza, *et al.*, "Design and Test of a GBTX-Based Board for the Upgrade of the ALICE TOF Readout Electronics", *IEEE Transactions on Nuclear Science*, vol. 64, no. 6, pp. 1357–1362, Jun. 2017, ISSN: 0018-9499. DOI: 10.1109/TNS.2017.2707302.

[47] M. Fanì, "Proposal of a Continuous Read-Out Implementation in the ALICE - TOF Detector", Master Thesis, University of Bologna (2015).

[48] P. Antonioli and S. Meneghini for the ALICE TOF Group, "A 20 ps TDC readout module for the ALICE Time of Flight system: design and test results", (2003). [Online]. Available: https://cds.cern.ch/record/722074.

[49] J. Christiansen, "HPTDC High Performance Time to Digital Converter", CERN, Geneva, Tech. Rep., 2004. [Online]. Available: https://cds.cern.ch/record/1067476.

[50] J. Mitra, S. Khan, S. Mukherjee, *et al.*, "Common Readout Unit (CRU) - A new readout architecture for the ALICE experiment", *Journal of Instrumentation*, vol. 11, no. 03, C03021, (2016).

[51] D. Falchieri for the ALICE Collaboration, "DRM2: the readout board for the ALICE TOF upgrade", *PoS*, (2018), TWEPP-17, 081. 6 p. [Online]. Available: https://cds.cern.ch/record/2312286.

[52] D. Falchieri for the ALICE Collaboration, "DRM2: the readout board for the ALICE TOF upgrade", (2017), TWEPP-17 Presentation. [Online]. Available: https://indico.cern.ch/event/608587/contributions/2614132/attachments/1520714/2376966/twepp2017_falchieri.pdf.

[53] The GBT Project, Edited by P. Moreira, J. Christiansen, K. Wyllie, *GBTX manual, v. 0.16*. [Online]. Available: https://espace.cern.ch/GBT-Project/GBTX/Manuals/gbtxManual.pdf.

[54] Silicon Labs, *Si5341, Si5340 Rev D Family Reference Manual*. [Online]. Available: https://www.silabs.com/documents/public/reference-manuals/Si5341-40-D-RM.pdf.

[55] Xilinx, *KC705 Evaluation Board for the Kintex-7 FPGA User Guide*, v1.8.1, Jul. 2018. [Online]. Available: https://www.xilinx.com/support/documentation/boards_and_kits/kc705/ug810_KC705_Eval_Bd.pdf.

[56] C. Flynt, *Tcl/Tk, Second Edition: A Developer's Guide*, 2nd. San Francisco, CA, USA: Morgan Kaufmann Publishers Inc., (2003), ISBN: 9781558608023.

[57] B. Chaudhary, *Tkinter GUI Application Development Hotshot*. Packt Publishing, (2013), ISBN: 9781849697941.

[58] K. Fall and W. Stevens, *TCP/IP Illustrated, Volume 1: The Protocols*, ser. Addison-Wesley Professional Computing Series. Pearson Education, (2011), ISBN: 9780132808187.

[59] Microsemi, *DS0128 Datasheet: IGLOO2 FPGA and SmartFusion2 SoC FPGA*. [Online]. Available: https://www.mouser.com/ds/2/523/Microsemi_SmartFusion2_and_IGLOO2_Datasheet-908525.pdf.

[60] G. Messenger and M. Ash, *Single Event Phenomena*. Springer US, (1997), ISBN: 9780412097317. DOI: 10.1007/978-1-4615-6043-2.

[61] M. Huhtinen and F. Faccio, "Computational method to estimate Single Event Upset rates in an accelerator environment", *Nuclear Instruments and Methods in Physics Research Section A: Accelerators, Spectrometers, Detectors and Associated Equipment*, vol. 450, no. 1, pp. 155–172, (2000), ISSN: 0168-9002. DOI: https://doi.org/10.1016/S0168-9002(00)00155-8.

[62] J. Ferencei, J. Pospisil, T. Vanat, *et al.*, "IGLOO2 - notes on radiation testing at NPI Rez", Nuclear Physics Institute of the Czech Academy of Science at Rez (Prague). [Online]. Available: https://twiki.cern.ch/twiki/pub/FPGARadTol/InformationOfInterest/IGLOO2_irradiation_at_NPI_Rez.pdf.

[63] J. Mariano, "ngCCM IGLOO2 Mezzanine Irradiation Test at University of Maryland", [Online]. Available: https://twiki.cern.ch/twiki/pub/FPGARadTol/InformationOfInterest/ngCCM_Mezzanine_IrradiationTest_at_UMD_v4.pdf.

[64] Trento Institute for Fundamentals Physics Applications, "Tifpa activity report 2017", Tech. Rep., May 2018.

[65] Trento Institute for Fundamentals Physics Applications, "Tifpa activity report 2015-16", Tech. Rep., Jan. 2017.

[66] F. Tommasino (TIFPA, Trento), "Experimental Cave at Trento CPT: status update", (2016), RDH/IRPT Meeting Presentation. [Online]. Available: https://agenda.infn.it/materialDisplay.py?contribId=25&sessionId=16&materialId=slides&confId=10837.

[67] S. Braccini, R. Cirio, M. Donetti, *et al.*, "Segmented ionization chambers for beam monitoring in hadrontherapy", *Modern Physics Letters A*, vol. 30, no. 17, 1540026, (2015). DOI: 10.1142/S021773231540026X.

[68] Microsemi, *SmartFusion2 and IGLOO2 Neutron Single Event Effects (SEE): TR0020 Test Report*. [Online]. Available: https://www.microsemi.com/document-portal/doc_view/135249-tr0020-smartfusion2-and-igloo2-neutron-single-event-effects-see-test-report.